NASA-CR-194356

A Global Traveling Wave on Venus

Michael D. Smith, Peter J. Gierasch, Paul J. Schinder

The dominant large-scale pattern in the clouds of Venus has been described as a "Y" or "Ψ" and tentatively identified by earlier workers as a Kelvin wave. A detailed calculation of linear wave modes in the Venus atmosphere verifies this identification. Cloud feedback by infrared heating fluctuations is a plausible excitation mechanism. Modulation of the large-scale pattern by the wave is a possible explanation for the Y. Momentum transfer by the wave could contribute to sustaining the general circulation.

The general circulation on Venus is dominated by spin of the atmosphere. The direction of the spin is the same as that of the planet but about 50 times faster at cloud-top level, approximately 70 km above the surface. The atmosphere is composed primarily of CO_2, and the pressures at the surface and at the cloud tops are ~90 bars and 50 mbar, respectively (*1*). The planet rotates with a period of 243 days, and the cloud tops with a period of 4 or 5 days. The detailed rotational structure shows jets at mid-latitudes (*2*) and vertical shear (*3*) that correlates with the vertical temperature gradient, but to a first approximation the rotation increases linearly with height and each shell of atmosphere is in rigid body rotation. This puzzling configuration is not understood, because countergradient momentum fluxes (Reynold's stresses) within the fluid are required to maintain the flow against dissipative processes.

The Venus clouds are featureless in visible light but show contrast in the ultraviolet (Fig. 1). The large-scale pattern has been described as a traveling Ψ or Y (turned sideways). It rotates with a period of 4 or 5 days and is global in scale (*4*), with a strong component at a zonal wave number of unity. The wave sometimes moves more rapidly than the equatorial wind speed and sometimes more slowly, but the speed difference is less than 20%. The true wind speed is indicated by the motion of small-scale blotches and wisps in the clouds (*5*). The visibility of the Y varies, and sometimes, although rarely, it is not apparent at all. Exhaustive analysis of Pioneer Venus orbiter images has revealed that the wave also manifests itself in perturbations of the zonal wind speed, with an amplitude of several meters per second and with a particular phasing relative to the albedo pattern (*6*).

Time-lapse images from the Galileo spacecraft (*7*) reveal that the wind oscillation was particularly strong at the time of the flyby (February 1990), with an amplitude of about 10 m s^{-1} (*8*). Figure 1 displays additional zonal (west-east) velocities that we have measured in order to examine the dependence of the amplitude on latitude. We have found that meridional (south-north) wave velocities are too small (less than 3 m s^{-1}) to extract from the data with present techniques.

Infrared monitoring from Earth at the flyby time revealed that the deep cloud varied spatially in optical thickness by as much as 25%, and that the variation contains a strong component with wave number equal to one (*9*). The velocity of the large-scale cloud disturbance is greater than that of small-opacity patches in the deep cloud, and we suggest that the high velocity is associated with the same global wave that is apparent in the cloud-top ultraviolet markings.

Belton *et al.* (*5*) speculated that the large-scale wave on Venus is analogous to a Kelvin mode, which is an internal gravity wave modified by Coriolis effects. This mode is confined to low latitudes and has zonal velocity perturbations but no meridional velocities. DelGenio and Rossow (*6*) confirmed a velocity field consistent with Kelvin waves in an extensive study of Pioneer Venus images. Covey and Schubert (*10*) calculated the structure of global-scale Kelvin waves on Venus but did not account for the excitation of the wave or the coherence of the Y with time. We report here calculations of the detailed structure of planetary waves on Venus. We find that there is a Kelvin-like mode, although global in scale, whose propagation speed agrees with the observations. Moreover, we find that radiative heating variations, caused by the influence of the wave on the cloud deck, can lead to a feedback that amplifies the wave and that a modulation of the large-scale cloud pattern by the wave can account for the Y feature.

Our mathematical model is similar to that used by Covey and Schubert (*10*). The equations of motion are linearized about a basic state in which the zonal velocity is proportional to the cosine of the latitude at each height; that is, each atmospheric shell

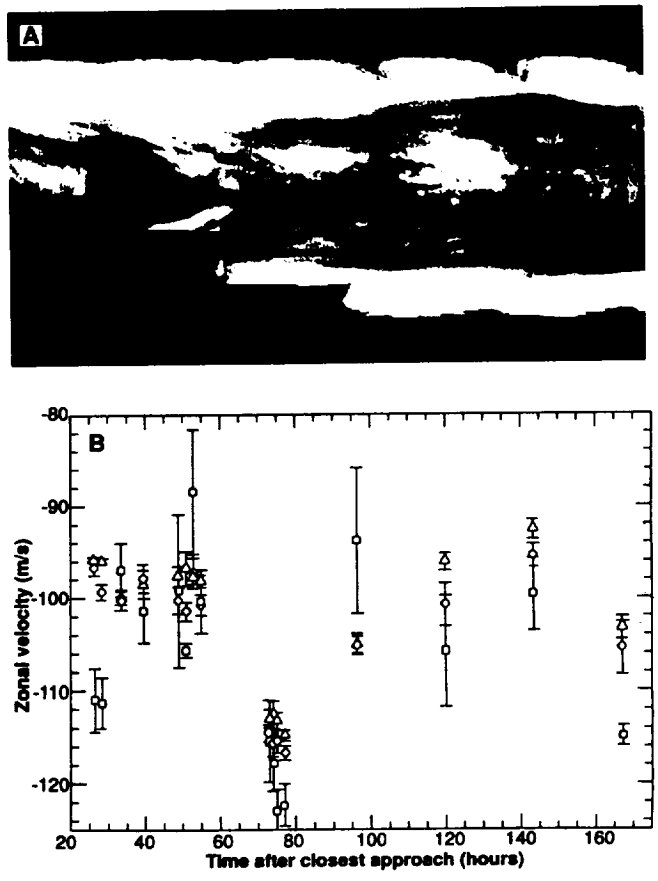

Fig. 1. (**A**) Rectangular projection of a set of Galileo images taken as the cloud system rotated under the spacecraft. (**B**) Wind measurements from the Galileo data (*8*). The data are shown as a time series for three different latitude bins: The triangles include measurements taken between 0° and 15° north, the diamonds between 15° and 30° north, and the squares between 30° and 45° north. A cyclical variation with an amplitude of ~10 m s^{-1} and a period of ~4 days is observed in all bins.

M. D. Smith and P. J. Gierasch, Astronomy Department, Space Sciences Building, Cornell University, Ithaca, NY 14853.
P. J. Schinder, Laboratory for Extraterrestrial Physics, National Aeronautics and Space Administration (NASA) Goddard Space Flight Center, Code 693, Greenbelt, MD 20771.

rotates as a rigid body. The velocity profile in height, and the temperature and stability profiles, are accurate reproductions of actual measurements (*11*). The vertical force balance is assumed to be hydrostatic, because large-scale waves are being examined. Radiative damping varies with height in a realistic way (*12*). Vertical diffusion of both heat and momentum are included. The diffusion coefficients are small except near the top of the model atmosphere, at 25 pressure scale heights, or at an altitude of ~145 km, where they are artificially made large to absorb upward energy propagation. This is done to simulate dissipative processes that are known to act in the upper atmosphere. The bottom boundary condition is a rigid surface. A broad, smooth external thermal forcing over the altitude range 20 km < z < 50 km is used. Solutions are harmonic in time and are represented spatially as a series of spherical harmonics whose coefficients vary in height. These are evaluated at grid points. Because of the vertical wind shear in the basic state, the variables do not separate in their latitude and height dependence. Typically, 500 grid points used in the vertical and spherical harmonics up to $Y_{m,11}$ are retained.

Free modes of the system would be characterized by three numbers: (i) the longitudinal wave number m, (ii) a latitudinal count of nodes n, and (iii) a vertical index that measures the complexity of the mode in the radial direction. Each of these modes would have a characteristic frequency. Because the system always contains a certain amount of dissipation, our mathematical model does not have "free" modes. However, if we impose a forcing over a range of frequencies and examine the response of the system, we find maxima at a certain set of frequencies, analogous to those of the free modes that an idealized closed system would exhibit. The complete family of modes shows horizontally propagating acoustic modes at high frequencies and gravity waves at low frequencies. Of particular interest are those modes that have longitudinal velocities close to that of the mean wind at cloud-top level because these are candidates for explaining the observed traveling mode. These turn out to be the lowest gravity modes, those with a small number of nodes in the vertical and in the horizontal.

Primarily because of the dissipation at the top of the system, none of these modes is highly tuned. The wave energy divided by the energy loss per period, or Q, is relatively small, on the order of five. Because the period is about 4 days, these modes will decay with a characteristic time of about 20 days. Thus, a process of excitation must be identified. Cloud feedback is a possibility. Measurements by Pioneer Venus probes show that the densest part of the Venus clouds is at an altitude of ~50 km, near their base (*13*). We hypothesize that vertical motions associated with the large-scale wave lead to evaporation (for downward motion, which produces compressional heating) or condensation (upward). In the optically thick regime (*14*), the infrared heat flux is inversely proportional to the cloud number density. Thus evaporation of particles will increase the upward radiative flux at the cloud base, leading to an increased heating just above the cloud base and to cooling just below it. Solar heating is of secondary importance at these depths, because the solar flux is attenuated by a factor of about 5 from its cloud-top value (*15*).

The cloud feedback can be parameterized if we add to the mathematical model a heating of the form (*16*)

$$Q' = \beta f(z) \frac{T}{t_R} \frac{\delta z}{H} \qquad (1)$$

where $f(z)$ is a profile function whose maximum is unity and whose shape and width are chosen to simulate the cloud effect, T is the temperature, t_R is the radiative time constant for temperature perturbations with a length scale of a scale height (*12*), δz is the vertical displacement associated with the wave, and H is the scale height of the atmosphere at cloud level; β sets the amplitude of the effect and is a parameter to be varied. This formulation is used to study cloud feedback heating caused by vertical motions. Other possibilities, such as cloud feedback heating caused by temperature perturbations, are not considered here. We have experimented with a detailed radiative transfer model to determine the effect of removing the bottom 2 km of the cloud deck. Guided by these results, we have chosen a smooth $f(z)$ with maximum modulus equal to unity, $f(z) > 0$ for 45 km < z < 49 km, $f(z) < 0$ for 49 km < z < 53 km, and $f(z) = 0$ elsewhere. For $\beta = 1$, a vertical displacement of one scale height produces a heating rate equal to the local temperature divided by the local radiative time constant. This means that a displacement of one scale height changes the radi-

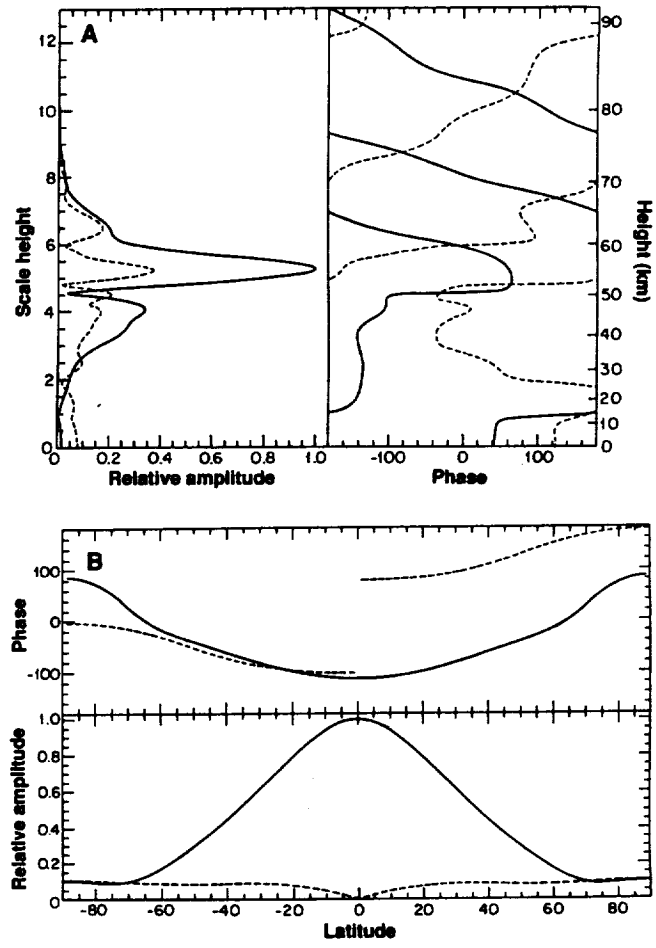

Fig. 2. Structure of the most unstable wave mode, with β adjusted to give zero growth rate. This structure is independent of the artificial external thermal forcing used to excite the system and is very nearly independent of β. For the neutral mode there is a resonance, and the free response has been isolated by subtracting two forced solutions in the immediate neighborhood of the resonance frequency. This has the effect of retaining only that part of the solution whose amplitude peaks near the resonance. This free response is then independent of the form of the external thermal forcing used, but the scaling is arbitrary. The solid line shows zonal velocities and the dashed line shows meridional velocities. In (**A**) the zonal velocity is taken at the equator, and the meridional velocity is taken at 30° north. The amplitude of the meridional velocity component has been multiplied by ten. The phases are shown relative to the longitude at which the zonal or meridional oscillation is completely real and positive (eastward or southward, respectively). In (**B**) both profiles are taken at a pressure scale height of 6.5 (63 km). Above ~55 km, the zonal velocity profile shows propagation upward; below 55 km, the wave is standing. The 180° changes in phase near 15 and 50 km are nodes.

ative flux by its own order of magnitude. If the cloud feedback effect occurs in a layer of thickness less than a scale height, as indicated by our $f(z)$, then values of β greater than unity are physically possible.

For $m = 1$ and $\beta = 1.217$, a moderately large but still physically reasonable value for the instability parameter, there is a neutrally stable mode whose phase speed is -102 m s^{-1}. The effect of β on the growth rate of the wave is roughly linear. Values of β larger than 1.217 will produce instability.

The most unstable mode has two nodes in the vertical and no nodes in the horizontal (see Fig. 2). The phase speed of -102 m s^{-1} is consistent with the wave observed in the Galileo images, although there is probably about a 20% uncertainty in the Galileo wave estimate because an observation period of only 7 days was used. The wave amplitude in zonal velocity is about five times the wave amplitude in meridional velocity at the cloud-top level, consistent with the Galileo wind measurements. The calculated zonal velocity amplitude is largest at the equator and has a full width at half maximum of about 70° (35°S to 35°N). Dynamically this wave is in the Kelvin class (*17*), as anticipated by DelGenio and Rossow (6), but global in scale. It propagates in the direction of the atmospheric rotation, the restoring force is gravity, and rotation acts to confine the amplitude in latitude.

The vertical structure of the wave shows strong attenuation above an altitude of ~60 km, suggesting that the visibility of the wave may depend on exactly where the cloud tops are located at a particular instant. There is evidence that the location of the Venus cloud tops is variable (*18*). The maximum amplitude of the zonal velocity fluctuation associated with the wave is near 55 km. We would anticipate that wind variations should be detectable in ground-based near-infrared images of Venus. A typical zonal velocity fluctuation observed at cloud top in the violet is 5 m s^{-1} (6), and the fluctuation at cloud base should be several times larger. Current near-infrared measurements (9) show large scatter in zonal velocity and can neither confirm nor rule out the presence of a wave with an amplitude of 25 m s^{-1}.

A spectrum showing the rates of energy inputs and outputs for the case with $\beta = 1.217$ (neutral stability) is shown in Fig. 3. For the most unstable mode (-102 m s^{-1}) the heating caused by cloud feedback is the largest source of energy input, while thermal diffusion and radiative damping act as energy sinks. Other sinks of energy, including friction and momentum coupling to the mean flow, are smaller.

For higher values of m, instabilities also exist. The critical value of β for the onset of instability is nearly independent of m for $m < 10$ and becomes large for $m > 10$. Thus we expect smaller scale modes to exist in addition to the $m = 1$ mode. The vertical structure of modes for $m > 1$ is confined to deeper levels and is probably not visible at 70 km where the violet features are formed. At cloud base the higher modes may have significant amplitude, and indeed small-scale structure is observed in the near-infrared (9).

An important property of a wave is the degree and sense of correlation between zonal, meridional, and vertical motions. We calculated the correlations and associated momentum fluxes of zonal angular momentum through surfaces of constant latitude and height for the most unstable mode. The lower atmosphere and cloud-top levels are accelerated at the expense of the forcing level, and the equator is accelerated at the expense of mid-latitudes. This is the correct sense of angular momentum transport needed to contribute to the maintenance of the cloud-top superrotation. The absolute correlation of the wave velocities is large, indicating that the direction of momentum transport is not sensitive to details in the vertical and horizontal structure of the wave.

In an earlier paper we postulated that the mid-latitude streaky pattern of clouds seen on Venus is attributable to the formation of clouds near the equator and the subsequent poleward advection and shearing of the clouds by the winds (*19*). Expanding on that idea, we performed a numerical experiment in which we released clouds at random locations near the equator and let the measured Galileo Venus mean wind (8) and a superimposed wave advect them forward. Figure 4 shows the results of this experiment based on the most unstable mode found above and typical values for the zonal and meridional wave amplitudes and phasing (*20*). We see a modulation of the cloud shapes and orientations of the cloud streaks at mid-latitudes caused by the wave, which are similar to those seen in the observations (Fig. 1). This suggests that the Ψ or Y feature is caused by the wave modulating the advective patterns of the clouds.

The oscillation of wind velocities seems to be sporadic in nature. In the Galileo data set the wave was very pronounced (8), but at times during the Pioneer Venus mission no wave was detected (6). Our calculation

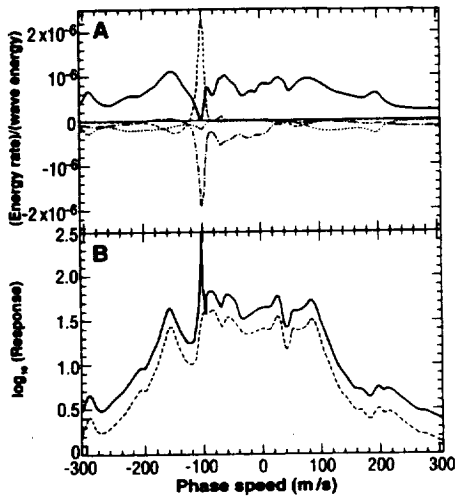

Fig. 3. (**A**) Spectrum of $m = 1$ wave energetics. The solid line shows the external thermal heating rate, the dashed line the cloud heating rate, the dash-dot line the rate of thermal diffusion, and the dotted line the rate of cooling by radiation. The cloud heating is only important in the region near the most unstable mode. At that frequency the heating rate from the external source is zero, indicating a neutral mode, and cloud heating is balanced primarily by thermal diffusion. For this value of β, all other wave modes show decay in time. (**B**) The response of the system as a function of frequency. The solid line shows the response with β set to give zero growth rate to the mode at -102 m s^{-1}. The dashed line shows the response when $\beta = 0$. The $\beta = 0$ spectrum has been offset downward by 0.25 unit. Shown without the offset, the two curves would be indistinguishable except near the frequency of the neutrally stable mode.

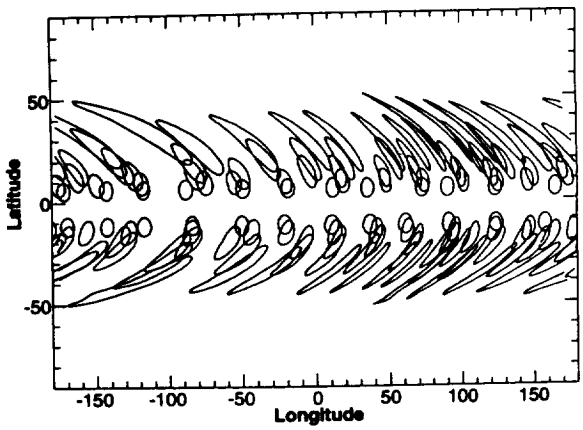

Fig. 4. Simulated cloud pattern. Circular bubbles are released at random longitudes near the equator and are then advected under the influence of the mean flow with an added wave. The mean flow is as measured from Galileo images (*8*) and includes poleward drift and mid-latitude jets.

shows that the wave amplitude of the most unstable mode varies strongly with height. It is possible that variation in the level of the observed cloud top contributes to the irregularity of the observed wind oscillations. A variation in the zonal wind profile or in the trapping properties of the atmosphere could also cause the wave to appear sometimes but not at other times. Our analysis of Pioneer Venus observations shows that velocity oscillations may appear for a few days, disappear, and then reappear with a phasing unrelated to the previously observed oscillation. This sort of behavior is consistent with the low Q associated with the waves in our computation.

Energy sources other than cloud feedback are possible. Instability of horizontal shear is an obvious candidate excluded by assumption from the modeling reported here. The key point is that a low-order global wave mode that appears to have the correct kinematic properties has been identified. In the absence of a forcing mechanism, it is estimated to decay with about a 20-day time scale. Cloud feedback seems to have the right magnitude to provide the forcing and also seems to pick out the correct phase velocity for the most unstable mode, but we have not excluded other possibilities for excitation.

REFERENCES AND NOTES

1. A. Seiff *et al.* [*J. Geophys. Res.* **85**, 7903 (1980)] reported the thermodynamic structure of the Venus atmosphere as measured by the NASA Pioneer Venus probes in 1979. Optical properties of the cloud tops were discussed by K. Kawabata *et al.* (*ibid.*, p. 8129).
2. The latitudinal profile of cloud-top winds varies over time, and the mid-latitude jets are sometimes almost absent. The 1974 profile was measured by S. S. Limaye and V. E. Suomi [*J. Atmos. Sci.* **38**, 1220 (1981)]; the 1979 profile by W. B. Rossow, A. D. DelGenio, S. S. Limaye, and L. D. Travis [*J. Geophys. Res.* **85**, 8107 (1980)]; and the 1982 profile by S. S. Limaye, C. Grassotti, and M. J. Kuetemeyer [*Icarus* **73**, 193 (1988)]. Profiles for 1980 and 1983 were measured by us and are presented in (*19*).
3. The vertical wind profile, based on tracking Pioneer Venus probe drifts, was found to be similar at four widely separated locations [C. C. Counselman III, S. A. Gourevitch, R. W. King, G. B. Loriot, *J. Geophys. Res.* **85**, 8026 (1980)].
4. M. J. S. Belton, G. R. Smith, D. A. Elliott, K. Klaasen, G. E. Danielson, *J. Atmos. Sci.* **33**, 1383 (1976); W. B. Rossow, A. D. DelGenio, S. S. Limaye, L. D. Travis, *J. Geophys. Res.* **85**, 8107 (1980).
5. M. J. S. Belton, G. R. Smith, G. Schubert, A. D. DelGenio, *J. Atmos. Sci.* **33**, 1394 (1976).
6. A. D. DelGenio and W. B. Rossow, *ibid.* **47**, 293 (1990).
7. A collection of articles on the Galileo flyby and the associated ground-based campaign was published in *Science* [**253**, 1516–1550 (1991)].
8. M. J. S. Belton *et al.*, *ibid.*, p. 1531.
9. See D. Crisp *et al.*, *ibid.*, p. 1538, and references therein.
10. C. Covey and G. Schubert, *J. Atmos. Sci.* **39**, 2397 (1982).
11. A convenient parameterization of the basic state wind and temperature profiles in the Venus atmosphere was introduced by R. E. Young *et al.*, *ibid.* **44**, 2628 (1987). We experimented with the sensitivity of wave modes to alterations in the basic state. The lowest modes, which turn out to be the ones of principal interest, are not highly sensitive to variations of the basic state that are consistent with observational variability or uncertainty.
12. We fitted a smooth function to the radiative time constant estimates by D. Crisp [*Icarus* **77**, 391 (1989)] for altitudes above ~60 km, and for a disturbance with vertical wavelength of ~20 km, roughly consistent with our calculated results. At altitudes less than 60 km, we followed the estimates by J. B. Pechmann and A. P. Ingersoll [*J. Atmos. Sci.* **41**, 3290 (1984)].
13. R. G. Knollenberg and D. M. Hunten [*J. Geophys Res.* **85**, 8039 (1980)] presented data from the Pioneer Venus particle size spectrometer experiment.
14. R. G. Knollenberg *et al.* (*ibid.*, p. 8059) calculated optical depths from the data presented in (*13*). There are about 20 optical depths at visible wavelengths within a layer that is 7 km thick (this is approximately a pressure scale height). M. G. Tomasko *et al.* (*ibid.*, p. 8187) estimated cross sections in the thermal infrared to be about half of those in the visible, which places the cloud in the optically thick regime.
15. M. G. Tomasko, L. R. Doose, P. H. Smith, A. P. Odell, *ibid.*, p. 8167.
16. Cloud instabilities of this type have been studied by P. J. Gierasch, A. P. Ingersoll, and R. T. Williams [*Icarus* **19**, 473 (1973)] and by S. J. Ghan [*J. Atmos. Sci* **46**, 2529 (1989)].
17. M. S. Longuet-Higgins [*Proc. R Soc. London Ser A* **262**, 511 (1968)] discussed the horizontal structure of waves on a rotating planet. We used his calculations to check our numerical procedure.
18. L. W. Esposito, *Science* **223**, 1072 (1984).
19. P. J. Schinder, P. J. Gierasch, S. S. Leroy, M. D. Smith, *J. Atmos. Sci.* **47**, 2037 (1990).
20. The phasing is chosen so that the maximum eastward perturbation in zonal velocities is in phase with the maximum northward perturbation in meridional velocities. The zonal wave amplitude is 10 m s^{-1}, and the meridional wave amplitude is 2 m s^{-1}. This phasing and amplitude are consistent with the results of our computation and with observations.

21. This work was supported by the NASA Galileo Project, the NASA Pioneer Venus Project, and the NASA Planetary Atmospheres Program. The computations were performed at the Cornell National Supercomputer Facility, which is supported by Cornell University, IBM, and the National Science Foundation. We thank M. J. S. Belton, C. Leovy, and two anonymous referees for helpful criticism.

24 December 1991, accepted 9 March 1992

GLOBAL-SCALE WAVES IN THE VENUS ATMOSPHERE

Michael D. Smith and Peter J. Gierasch,
Astronomy Department, Space Sciences Building,
Cornell University,
Ithaca NY 14853.

Paul J. Schinder
Laboratory for Extraterrestrial Physics,
NASA Goddard Space Flight Center, Code 693,
Greenbelt MD 20771.

Accepted by *Journal of the Atmospheric Sciences*, in press
June 1992
Revised April 1993

ABSTRACT:

The nature of global-scale waves that can exist in the atmosphere of Venus is examined. A linear three-dimensional model atmosphere with spherical geometry is used to study large-scale forced and free waves. Solutions are obtained numerically with grid points in the vertical and a spherical harmonic expansion in the horizontal. Observations have shown a global-scale traveling wave with phase speed near the cloud top wind velocity. Global-scale wavemodes are found to exist in the model at this velocity. When a radiative-dynamic cloud feedback is added to the model, the most unstable wavemode is found to have the same phase speed as the observed wave. The horizontal structure of this wave is consistent with the observed horizontal structure of the "Y" feature seen in ultraviolet images of the Venus cloud top.

1. INTRODUCTION:

At the time of the Galileo spacecraft's flyby of Venus in February 1990 an especially strong global-scale oscillation in zonal wind velocity was observed, with an amplitude of about 10 m s^{-1} and a period of about 4 days (Belton et al. 1991, Smith et al. 1992). Figure 1 shows the zonal wind speeds we have measured from the Galileo images of Venus. An oscillation of about 10 m s^{-1} is apparent with the same phase in three different latitude bands. Meridional velocities measured at the same time show no detectable oscillation. This is strong evidence for the presence of a Kelvin-like wave.

Global-scale waves were first observed at the Venus cloud top by Belton et al. (1976) using Mariner 10 images. They discovered that small-scale markings in the cloud top had a different rotational period than large-scale markings, indicating the propagation of global-scale waves. They identified the waves as of Kelvin type. Del Genio and Rossow (1982) detected several different periodicities in time series of cloud top brightness in Pioneer Venus images which were different than the period derived from the velocity of cloud-tracked winds. This was attributed to the presence of global-scale waves. They speculated that two wave types exist: an equatorial Kelvin wave, and a mid-latitude Rossby wave. Later, Del Genio and Rossow (1990) confirmed their earlier wave identifications, and in addition, measured velocity oscillations associated with the waves in a detailed analysis of

the Pioneer Venus image data set. They also found that while global-scale waves exist at some times in the Pioneer Venus data set, they are not apparent at other times.

Previous computations of global-scale oscillations in the Venus atmosphere have primarily concentrated on solar thermal tides (for example Pechmann and Ingersoll 1984, Fels 1986), and their interaction with the mean zonal flow (for example Leovy 1987, Baker and Leovy 1987, Newman and Leovy 1992). The present work investigates the general question of the nature of global-scale waves that can exist in the Venus atmosphere. No comprehensive search and classification of Venus wavemodes has ever been done before. Covey and Schubert (1982) carried out the pioneering study of this subject. We are now able to achieve much higher latitudinal and spectral resolution because of computational advances. We have utilized two numerical models. To help in the classification of wavemodes, we explore a simple 2-D cartesian geometry model which is very useful for exhibiting the fundamental classes of waves. Parameter space can be explored easily to find which qualities of the atmosphere affect the frequency and structure of wavemodes. In sections 2 and 3 a linear, three-dimensional model in spherical coordinates is presented. This model attempts to more accurately simulate the Venus atmosphere. Radiative damping and the vertical diffusion of heat and momentum are included. As in Smith et al. (1992), a radiative-dynamic cloud feedback heating is proposed as a possible excitation mechanism for the wavemodes that we find. In section 4 we look at the energetics and momentum transports of the waves, and in section 5 we carry out sensitivity studies to see what properties affect the structure and frequency of the computed waves. In section 6 we summarize our findings and discuss implications of the global-scale waves including a possible explanation for the "Y" feature.

2. THE 3-D SPHERICAL GEOMETRY MODEL:

a. Basic Equations

The fluid equations in spherical coordinates are:

$$\frac{\mathrm{D}u}{\mathrm{D}t} + v\cos\theta\left(2\Omega + \frac{u}{a\sin\theta}\right) + \frac{1}{a\sin\theta}\frac{\partial\Phi}{\partial\phi} = -F_\phi \qquad (1)$$

$$\frac{\mathrm{D}v}{\mathrm{D}t} - u\cos\theta\left(2\Omega + \frac{u}{a\sin\theta}\right) + \frac{1}{a}\frac{\partial\Phi}{\partial\theta} = -F_\theta \tag{2}$$

$$\frac{\partial\Phi}{\partial z} = RT \tag{3}$$

$$c_p\frac{\mathrm{D}T}{\mathrm{D}t} + RTw = Q_{\mathrm{ext}} \tag{4}$$

$$\frac{1}{a\sin\theta}\frac{\partial u}{\partial\phi} + \frac{1}{a\sin\theta}\frac{\partial}{\partial\phi}\left(v\sin\theta\right) + \frac{\partial w}{\partial z} - w = 0 \tag{5}$$

where

$$\frac{\mathrm{D}}{\mathrm{D}t} = \frac{\partial}{\partial t} + \frac{u}{a\sin\theta}\frac{\partial}{\partial\phi} + \frac{v}{a}\frac{\partial}{\partial\theta} + w\frac{\partial}{\partial z} \tag{6}$$

and the vertical coordinate z is measured in pressure scale heights, $z = -\ln(p/p_{\mathrm{surface}})$. The angular coordinates θ and ϕ correspond to co-latitude and east longitude respectively, and u, v, and w are the velocities of the fluid in the $\hat{\phi}, \hat{\theta}$, and $\hat{z}$ directions. T is temperature, Φ is geopotential, c_p is the specific heat, R is the gas constant, a is the planet radius, and Ω is the rotation rate of the coordinate system with respect to inertial space. On the right hand side, an external mechanical forcing $\mathbf{F}$ and an external thermal forcing Q_{ext} may be applied.

Following Covey and Shubert (1982), we replace the horizontal momentum equations with equations for the horizontal divergence and the vertical component of vorticity. The horizontal velocities u and v are expressed by $\mathbf{u} = \nabla\chi + \nabla\times\hat{z}\Psi$ where ∇ is the horizontal gradient operator and $\mathbf{u} \equiv (u, v)$ is the horizontal velocity vector. This gives us:

$$\frac{\partial_m^*(\nabla^2\chi)}{\partial t} + 2\frac{\partial\bar{\Omega}}{\partial z}\frac{\partial w}{\partial\phi} + \nabla^2\Phi + (2\bar{\Omega} - 2\Omega)\left(\cos\theta\nabla^2\Psi + \frac{1}{a^2}\frac{\partial\chi}{\partial\phi} - \frac{\sin\theta}{a^2}\frac{\partial\Psi}{\partial\theta}\right) = -\nabla\cdot\mathbf{F} \tag{7}$$

$$-\frac{\partial_m^*(\nabla^2\Psi)}{\partial t} + \frac{\partial\bar{\Omega}}{\partial z}(4w\cos\theta + 2\frac{\partial w}{\partial\theta}\sin\theta) + (2\bar{\Omega} - 2\Omega)\left(\cos\theta\nabla^2\chi - \frac{1}{a^2}\frac{\partial\Psi}{\partial\phi} - \frac{\sin\theta}{a^2}\frac{\partial\chi}{\partial\theta}\right) = -\nabla\times\mathbf{F} \tag{8}$$

$$\frac{\partial_r^*(RT)}{\partial t} + H^2N^2w + \frac{\partial}{\partial z}(\bar{\Omega} - \Omega)^2\left(\frac{\partial\chi}{\partial\theta}\sin\theta\cos\theta + \frac{\partial\Psi}{\partial\phi}\cos\theta\right) = \frac{RQ}{c_p} \tag{9}$$

$$\frac{\partial\Phi}{\partial z} = RT \tag{10}$$

$$\nabla^2\chi + \frac{\partial w}{\partial z} - w = 0 \tag{11}$$

where,

$$\frac{\partial^*_{m,r}}{\partial t} = \frac{\partial}{\partial t} + \gamma_{m,r} - \frac{1}{p}\frac{\partial}{\partial z}\frac{pK_{m,r}}{H^2}\frac{\partial}{\partial z} + 2(\bar{\Omega} - \Omega)\frac{\partial}{\partial \phi} \tag{12}$$

Rayleigh friction and Newtonian cooling rates have been included and are given by γ_m and γ_r respectively. $K_{m,r}$ are the mechanical and thermal vertical diffusion coefficients, and H is the pressure scale height. The zonal wind enters through the definition $\bar{\Omega} \equiv \Omega + \bar{u}/(a\sin\theta)$.

We write $\{\chi, \Psi, T, \Phi, w\} = \{\bar{\chi}, \bar{\Psi}, \bar{T}, \bar{\Phi}, \bar{w}\} + \{\chi', \Psi', T', \Phi', w'\}$. The barred quantities are a time independent solution to the equations (1)–(5), and the primed quantities are small perturbations about the barred quantity basic state. Next, for each layer j we expand each quantity in a sum of spherical harmonics:

$$\{\chi', \Psi', T', \Phi', w'\}_j(\theta,\phi) = \sum_{\ell,m} \{\chi', \Psi', T', \Phi', w'\}_{j,\ell,m} Y_{\ell,m}(\theta,\phi)\, e^{-i\omega t} \tag{13}$$

Finally, we expand to first order in the primed quantities and finite difference the equations. The combinations $\cos\theta Y_{\ell m}$ and $\sin\theta \frac{\partial Y_{\ell m}}{\partial \theta}$ that are found in the resulting equations can be rewritten in terms of $Y_{\ell+1,m}$ and $Y_{\ell-1,m}$ so that for each level j and set of Fourier components ℓ and m there is a set of five unknowns $(\chi', \Psi', T', \Phi', w')$ and five equations (7)–(11).

b. Boundary Conditions

The upper boundary condition is taken to be a free surface at $z = 25H$ with:

$$\frac{\partial \chi'}{\partial z} = 0 \tag{14}$$

$$\frac{\partial \Psi'}{\partial z} = 0 \tag{15}$$

$$\frac{\partial T'}{\partial z} = 0 \tag{16}$$

$$w' = 0 \tag{17}$$

Upper atmospheric wave absorption is simulated by placing a highly dissipative layer in the upper few scale heights of the model.

The lower boundary of the model is an impenetrable rigid flat surface whose linearized position is $z = 0$. The lower boundary conditions are the same as the upper boundary conditions except that (17) is replaced by:

$$RTw' + \left(-i\omega + im\left(\bar{\Omega} - \Omega\right)\right)\Phi' = 0 \tag{18}$$

or equivalently, that the Lagrangian time derivative of Φ=0.

c. Basic State

Each spherical shell of the atmosphere is assumed to have constant angular velocity. The vertical profiles of wind and static stability are similar to those of Young et al. (1987), but with a few modifications. Figure 2 shows the nominal zonal wind velocity $\bar{u}(z)$ and Brunt-Väisälä frequency $N^2(z)$ profiles. Both profiles are chosen to be consistent with Pioneer Venus descent probe data (Seiff et al. 1980 and Councelman et al. 1980).

In this model, we use vertical diffusion, Rayleigh friction and Newtonian thermal damping for dissipation. The vertical profile of the radiative time constant $t_r \equiv 1/\gamma_r$ is shown in Fig. 3. It was chosen to be consistent with the radiative time constant computed by Crisp (1989) for the Venus atmosphere at altitudes above 50 km, and with the profiles computed by Hou et. al. (1989) at lower altitudes. This profile of t_r is very similar to that used in the thermal tide model of Pechmann and Ingersoll (1984) at altitudes in and above the clouds. The mechanical friction rate γ_m was set to be small enough not to contribute significantly to the energetics of the wave. Figure 3 also shows the values used for the vertical diffusion coefficients of momentum and heat ($K_m = K_r$ for all cases presented). Except at the very top, they were chosen to be just large enough to damp features smaller than the vertical grid size. Structure with vertical scale larger than the grid size is retained. In the upper few scale heights the vertical diffusion coefficients were made artificially large to simulate upper atmospheric dissipation, and to damp reflections from the upper boundary.

The external heating rate Q_{ext} shown in Fig. 3 was chosen to be a broad, smooth function so that it would excite a wide range of wavemodes that exist in and near the Venus cloud deck. This forcing is artificial. It is used only to excite wavemodes and is not meant to accurately describe thermal forcing in the Venus atmosphere. As is shown later in section 3, the exact shape and height of $Q_{ext}(z)$ is not important since we are primarily concerned with the free wave component of the forced waves we compute. In all the cases presented here we have used no mechanical forcing, so $\mathbf{F} = 0$.

d. Method of Solution

For each layer j and set of spectral components (ℓ, m), we have the five equations (7)–(11). There are an equal number of unknowns $(\chi'_{j\ell m}, \Psi'_{j\ell m}, T'_{j\ell m}, \Phi_{j\ell m}, w'_{j\ell m})$. This is a set of linear equations, and the system is solved by rewriting the set as a matrix equation. The matrix is filled with the appropriate coefficients, inverted, and multiplied by the right hand side. The inversion is accomplished using the LINPACK routines ZGBFA and ZGBSL (Dongarra et al. 1979). The final solutions are then obtained by plugging the coefficients $\chi'_{j\ell m}$ *etc.* back into (13). The quantities u' and v' can be reconstructed from χ' and Ψ' using:

$$u' = \frac{1}{a \sin\theta} \frac{\partial \chi'}{\partial \phi} - \frac{1}{a} \frac{\partial \Psi'}{\partial \theta} \tag{19}$$

$$v' = \frac{1}{a \sin\theta} \frac{\partial \Psi'}{\partial \phi} + \frac{1}{a} \frac{\partial \chi'}{\partial \theta} \tag{20}$$

We found through experimentation that 500 layers in the vertical will adequately resolve the structure of the wavemodes of interest. The layers are spaced equally in pressure scale heights giving a resolution of .05 scale heights, or about .3 km, near the cloud top. We are mainly interested in global-scale waves with low wavenumber m, so spherical harmonics through $Y_{11,m}(\theta, \phi)$ were kept to insure accuracy. The computation was carried out at the Cornell National Supercomputer Facility.

The model was tested against the structure of Hough modes on a sphere calculated by Longuet-Higgins (1968). Specifically, $m = 1$ wavemodes with no nodes in the vertical, and zero or two nodes in the horizontal were compared for both a fast and a slow rotation rate.

Our model is not directly comparable to the work of Longuet-Higgins since we compute forced waves. However, by looking at the "free wave" component of the forced waves (see section 3 below) we find excellent agreement between the results of our model and of Longuet-Higgins. By setting the external thermal forcing to the appropriate frequency, we can investigate thermally driven solar tides. Using Earthlike basic state parameters, we compared the results of our model to classical tidal theory calculations for the diurnal and semidiurnal tides on the Earth (Lindzen 1967, Chapman and Lindzen 1970). The results of our computations generally agree well but differ for wavemodes with very short vertical wavelengths. However, in the present paper we are primarily concerned with higher frequencies and larger vertical wavelengths and this limitation is not a concern. As a final test, the model was set up to have a simple three-layer vertical structure and parabolic zonal wind profile. A run with $m = 11$ (for shorter wavelengths which minimize the effect of spherical geometry) was compared against the results of a simple 2-D cartesian geometry model and good agreement was found. The 2-D model was also used to help interpret results from the 3-D model.

c. Cloud Feedback Heating

We have experimented with a heuristic radiative feedback near the base of the cloud deck. Leovy (1966) pointed out that a heating rate proportional to vertical displacement can lead to linear instability of gravity wave modes. Gierasch et al. (1973) and Ghan (1989) show that dynamical perturbation of clouds can alter heating rates in this manner. Recent observations of Venus at near infrared wavelengths (Carlson et al., 1991) suggest that there are 25% fluctuations in the optical depth of the cloud deck, with fluctuations concentrated near the cloud base at an elevation of about 50 km. The microphysics of the Venus clouds are not well understood. We have simply parameterized the assumption that vertical displacement near the cloud base causes evaporation or condensation, altering the number density which in turn alters the radiative flux and thus the heating rate.

The net radiative effect of the Venus cloud deck is to produce warming near its base and cooling above the base. This is demonstrated by the observed temperature profile, which shows a relatively large gradient within the lower part of the cloud (Pioneer measurements

of cloud density are presented by Knollenberg and Hunten, 1980, and measurements of temperature by Seiff et al., 1980.). If the cloud is made more dense by upward vertical motion, the amplitude of the maximum heating and cooling are increased. Thus the heating perturbation is negative just above the cloud base and positive just below it. Heating perturbations far from the cloud base are negligible. Conversely if vertical motion is downward and the cloud base is made less dense, the heating perturbation is positive just above the cloud base location and negative just beneath it.

We have experimented with simple models of the cloud radiative transfer and find that the width of the affected layer is typically a few optical depths, which is a few kilometers (Knollenberg and Hunten, 1980). Guided by these considerations, we introduce a perturbation heating profile that is proportional to the vertical displacement, with an amplitude set by the local radiative time constant:

$$Q_{\text{cloud}} = \beta f(z) \frac{T}{t_r} \frac{\delta z}{H}, \tag{21}$$

where β is an amplitude parameter, $f(z)$ is a shape profile (maximum amplitude unity, positive below the base and negative above the base), T is the full temperature, t_r is the radiative time constant based on a length of a scale height, δz is the vertical displacement and H is the local scale height. For $\beta = 1$, this parameterization sets the amplitude of the cloud heating to be on the order of T/t_r for a vertical displacement of one scale height. If β is set larger than unity, the heating rate can be larger than this limit. This can be appropriate if the vertical scale of $f(z)$ is smaller than a scale height. The $f(z)$ adopted for the calculations reported in this paper is displayed in Fig. 4. It is characterized by a length scale of about half a scale height.

3. 3-D SPHERICAL GEOMETRY MODEL RESULTS:

a. Nominal Basic State

By imposing the forcing over a range of frequencies, we find maxima in the response of the system at certain frequencies. Figure 5 shows a spectrum of the response (defined as the maximum value of $w'(z)\, e^{-z/2}$ anywhere in the domain of z) for the nominal basic state and wavenumber $m = 1$. We see a series of peaks in the response which indicate

"preferred" frequencies. Since our model contains dissipation it does not have true resonant modes. In fact, primarily because of the large amount of dissipation placed in the upper few scale heights of the model, the peaks seen in the spectrum are relatively wide and none of the wavemodes is highly tuned. The wave energy divided by the energy loss per period, or the "Q", is small, on the order of five. Since the period of the waves is typically around four days, they will decay with a characteristic time of about 20 days.

The peaks in Fig. 5 are forced waves, but if the wave response is the sum of a component which varies slowly with frequency near the resonant frequency plus a "free wave" component whose amplitude is peaked at the resonant frequency, then the "free wave component" can be separated out by taking

$$X_{\text{free}} = X_{\text{forced}}(\omega_1) - X_{\text{forced}}(\omega_2) \tag{22}$$

where ω_1 and ω_2 are two forcing frequencies near the resonant frequency, and $X = (\chi', \Psi', T', \Phi, w')$. There is a complex scaling factor left undetermined in the resulting free wave component which is dependent on the choice of $\omega_{1,2}$.

Using (22), Fig. 6 shows the vertical structure of the free wave zonal wind amplitude of four of the lower wavemodes in Fig. 5 (phase speeds of –295, –156, –102, and –85 m s^{-1}) for the nominal basic state. These are gravity waves with no nodes in the latitudinal direction and increasingly complicated vertical structure with decreasing phase speed. The degree to which each wavemode penetrates to high altitudes is one factor which determines how highly tuned the wavemode is. The two lowest wavemodes shown have significant amplitude high in the atmosphere and are damped by the high diffusion placed at the top of the model. Diffusion also damps waves which have large vertical gradients. Higher wavemodes than those shown in Fig. 6 have very large vertical gradients and are damped by diffusion so much that they do not appear as peaks in the spectrum shown in Fig 5. The third and fourth lowest wavemodes seem to strike the best compromise between these two limits. They show the highest amplitudes in the spectra and are the most highly tuned. The vertical structure of the meridional wave component of these waves is not as confined in general, and has much smaller amplitude.

b. Cloud Feedback Added

To explore a possible excitation mechanism for these waves, cloud feedback heating [see equation (21)] has been added in some of the runs. Figure 7 shows the same spectrum as the nominal case (Fig. 5) except that a cloud feedback has been added with amplitude $\beta = 1.217$. Figures 5 and 7 are nearly identical except in the region near phase speed -100 m s^{-1}. For $m = 1$ and this $\beta = 1.217 \equiv \beta_{crit}$ there is one wavemode which has become neutrally stable. For smaller values of β there are no unstable wavemodes. For $\beta > \beta_{crit}$ one or more wavemodes will be unstable. The wavemode which has become neutrally stable at $\beta = \beta_{crit}$ is the most unstable wavemode and has an equatorial phase speed of -102 m s^{-1}. This represents a period of about 4.3 days, consistent with the period of the wave observed in Galileo zonal wind speed data and with the low latitude wave identified by Del Genio and Rossow (1990).

Figure 8 shows the vertical structure of the free wave component of the wavemode with phase speed -102 m s^{-1} for the nominal basic state with $\beta = \beta_{crit}$. The vertical structure is nearly identical to the structure of the wavemode at the same phase speed shown in Fig. 6. This is a gravity wave with two nodes in the vertical. The wave zonal wind has most of its amplitude confined to an altitude between about 50 km and 60 km. The peak amplitude is located at 55 km or in the lower part of the cloud deck. There is a strong attenuation of the zonal wave amplitude above 60 km. The meridional component is not as confined and has a much smaller amplitude. The phasing of the wave shows standing behavior below 53 km and upward propagation above.

Figure 9 shows the horizontal structure of the free wave component of the wavemode with phase speed -102 m s^{-1} for the nominal basic state with $\beta = \beta_{crit}$. The horizontal structure is nearly identical to the case with $\beta = 0$. This wavemode has no nodes in the horizontal. In our model we only look for wavemodes whose wave zonal wind is hemispherically symmetric, and whose wave meridional wind is antisymmetric. The zonal wind component of the wave is confined in latitude as well as in height and has a full width half maximum of about 70 degrees (35° S to 35°N). This indicates an equivalent depth of about 100 meters. The phase of this wave shows some change near the poles, but only

a small gradual change in phase where most of the wave amplitude is. This is consistent with Galileo observations which show little change in the phase of the wave with latitude. The very small meridional amplitude, the zonal amplitude confined to low latitudes, and the Doppler shifted phase velocity in the direction of rotation identifies this gravity wave as a Kelvin-like wave.

c. Rossby Waves

Figure 10 shows the spectrum for a Venus-like stability profile, a constant zonal wind of –50 m s^{-1}, and an artificially very small radiative damping. In addition to the prograde and retrograde gravity waves, the spherical geometry allows other classes of wavemodes to exist. In the region between -38 and –50 m s^{-1} there are small peaks in the spectra which correspond to the two lowest Rossby waves with vertical structure similar to the gravity waves with one and two nodes.

4. ENERGETICS AND MOMENTUM TRANSPORTS:

a. Energetics

To learn more about the wavemodes we have described above it is useful to calculate the energetics of the waves. Let $\mathbf{v}'_{\mathbf{h}} = (u', v', 0)$, then dot (1) and (2) with $\mathbf{v}'^{*}_{\mathbf{h}}$ and add to the dot product of the complex conjugate of (1) and (2) with $\mathbf{v}'_{\mathbf{h}}$,

$$2(D + D^*)(u'u'^* + v'v'^*) + 2\frac{\partial \bar{\Omega}}{\partial z} a \sin\theta \, (u'w'^* + u'^*w') = -(\mathbf{v}'^{*}_{\mathbf{h}} \cdot \mathbf{F} + \mathbf{v}'_{\mathbf{h}} \cdot \mathbf{F}^*) \qquad (23)$$

Adding $(\partial\Phi'/\partial z) \cdot (9)^* + (\partial\Phi'/\partial z)^* \cdot (9)$ and using $D + D^* = 2\mathrm{Im}(\omega)$ and the continuity equation (11) we find,

$$\mathrm{Im}(\omega)(KE + PE) + C_1 + C_2 = -W + H \qquad (24)$$

where,

$$KE = \frac{1}{2} e^{-z} \left(|u'|^2 + |v'|^2 \right) \qquad = \text{Kinetic Energy} \quad (25)$$

$$PE = \frac{1}{2}\frac{\epsilon^{-z}}{H^2N^2}\left|\frac{\partial\Phi'}{\partial z}\right|^2 \qquad = \text{Potential Energy} \quad (26)$$

$$C_1 = 2\frac{\partial\bar{\Omega}}{\partial z}a\sin\theta\,\epsilon^{-z}\frac{u'w'^* + u'^*w'}{4} \qquad = \text{Stress Work on Mean Flow} \quad (27)$$

$$C_2 = a\cos\theta\sin\theta\frac{\partial}{\partial z}\left((2\bar{\Omega}-\Omega)^2\right)\frac{\epsilon^{-z}}{4H^2N^2}\left(v'\frac{\partial\Phi'^*}{\partial z} + v'^*\frac{\partial\Phi'}{\partial z}\right)$$
$$= \text{Horiz. Transfer of Buoyancy} \quad (28)$$

$$W = \frac{\epsilon^{-z}}{4}\left(\mathbf{v}_\mathbf{h}'^* \cdot \mathbf{F} + \mathbf{v}_\mathbf{h}' \cdot \mathbf{F}^*\right) \qquad = \text{Work Done} \quad (29)$$

$$H = \frac{R\epsilon^{-z}}{4c_pN^2H^2}\left(Q'\frac{\partial\Phi'^*}{\partial z} + Q'^*\frac{\partial\Phi'}{\partial z}\right) \qquad = \text{Heating} \quad (30)$$

The "work done" and "heating" terms may be expanded still further. The "work done" term contains contributions from Rayleigh friction and from the vertical diffusion of momentum. Likewise, the "heating" term contains contributions from external forcing, cloud feedback heating, Newtonian cooling, and the vertical diffusion of heat.

$$W = W_1 + W_2, \qquad H = H_1 + H_2 + H_3 + H_4$$

$$W_1 = 2\left(\mathbf{v}_\mathbf{h}'^* \cdot \mathbf{v}_\mathbf{h}'\right) \qquad = \text{Rayleigh Friction} \quad (31)$$

$$W_2 = u'^*x_1 + v'^*x_2 + u'x_1^* + v'x_2^* \qquad = \text{Momentum Diffusion} \quad (32)$$

$$x_1 = \frac{1}{p}\left(\frac{\partial\left(pK_m/H^2\right)}{\partial z}\frac{\partial u'}{\partial z} + \frac{pK_m}{H^2}\frac{\partial^2 u'}{\partial z^2}\right) \quad (33a)$$

$$x_2 = \frac{1}{p}\left(\frac{\partial\left(pK_m/H^2\right)}{\partial z}\frac{\partial v'}{\partial z} + \frac{pK_m}{H^2}\frac{\partial^2 v'}{\partial z^2}\right) \quad (33b)$$

$$H_1 = R^2\left(Q_{\text{ext}}^*\frac{\partial\Phi'}{\partial z} + Q_{\text{ext}}\frac{\partial\Phi'^*}{\partial z}\right) \qquad = \text{External Heating} \quad (34)$$

$$H_2 = \frac{i\beta gRH}{t_r\left(\omega - 2m\left(\bar{\Omega}-\Omega\right)\right)}\left(w'^*\frac{\partial\Phi'}{\partial z} + w'\frac{\partial\Phi'^*}{\partial z}\right) \qquad = \text{Cloud Feedback Heating} \quad (35)$$

$$H_3 = -\frac{2R^2}{t_r}\left(T'T'^*\right) \qquad = \text{Radiative Cooling} \quad (36)$$

$$H_4 = R^2\left(T'x_3^* + T'^*x_3\right) \qquad = \text{Thermal Diffusion} \quad (37)$$

$$x_3 = \frac{1}{p}\left(\frac{\partial\left(pK_t/H^2\right)}{\partial z}\frac{\partial T'}{\partial z} + \frac{pK_t}{H^2}\frac{\partial^2 T'}{\partial z^2}\right) \quad (38)$$

The calculation of the energy components provides an independent check on the accuracy of the entire computation. In our computations an external forcing exists and $\mathrm{Imag}(\omega) = 0$, so we should have $C_1 + C_2 - H - W = 0$. Figure 11 shows an estimate of the error: $(C_1 + C_2 - W_1 - W_2 - H_1 - H_2 - H_3 - H_4)/(\text{Largest Term})$ for the nominal case as a function of frequency. A perfectly accurate computation would return a value of zero for this error estimate. For most of the frequency range the error is less than one percent indicating no numerical problems. At a few frequencies, vertical wavelengths become very short and there are larger errors. At the frequencies of the wavemodes discussed above, this error estimate indicates that the computation of the wave structure and the associated energy components is accurate to within one percent.

In Figure 12 a spectrum of the contribution of the individual energy components is shown for the nominal case, and for the case with cloud feedback of strength $\beta = \beta_{\mathrm{crit}}$ added. Energy sources are plotted as positive energy rates, while energy sinks are plotted as negative energy rates. For the nominal case, external heating is the main source of energy and thermal diffusion is the major energy sink. For the most unstable wavemode (-102 m s^{-1}) with cloud feedback heating added, the major source of energy input is from cloud feedback heating and again thermal diffusion acts as the main energy sink.

The effect of the instability scaling parameter β on the energetics of the most unstable wavemode is only roughly linear. Figure 13 shows spectra of the growth rate in the region of the most unstable wave for three different values of β. The growth rate of the wave can be estimated by taking the opposite of the external heating rate. The region where the effect of cloud feedback heating is significant is rather narrowly confined in frequency for values of $\beta \leq \beta_{\mathrm{crit}}$. The effect of cloud feedback heating is present in the other wavemodes, but they apparently require a much larger (and probably unphysical) value of β to become unstable.

b. Momentum Transports

An important property of a wave is the degree and sense of correlation between zonal, meridional, and vertical motions. Let the rate of angular momentum transported per second through a surface of constant height be $\dot{L}_{u\dot{w}}$ and the rate of angular momentum

transported per second through a surface of constant latitude be $\dot{L}_{uv}$. Then,

$$\dot{L}_{uw} = \int 0a^2 \sin\theta \mathrm{d}\theta \mathrm{d}\phi \, \rho(a\sin\theta) < u'\hat{w}' >$$
$$= \frac{a^3 p}{4gH(z)} \int (u'\hat{w}'^* + u'^*\hat{w}') \sin^2\theta \, \mathrm{d}\theta \mathrm{d}\phi \tag{39}$$

$$\dot{L}_{uv} = \int H \mathrm{d}z \, \mathrm{d}\phi \, \rho(a\sin\theta)^2 < u'v' >$$
$$= \frac{2\pi a^2 p \sin^2\theta}{4g} \int (u'v'^* + u'^*v') \, \mathrm{d}z \tag{40}$$

where $\hat{w} = H(z)w$ is the vertical velocity in centimeters per second, $< u'\hat{w}' >$ is the quantity $u'\hat{w}'$ averaged over latitude and longitude at a given height, and $< u'v' >$ is the quantity $u'v'$ averaged over height and longitude at a given latitude.

We can also calculate a dimensionless correlation coefficient to give a measure of the degree of correlation between wave velocities,

$$r_{uv} = \frac{< u'v' >}{(< u'u' >< v'v' >)^{1/2}} \tag{41}$$

$$r_{uw} = \frac{< u'w' >}{(< u'u' >< w'w' >)^{1/2}} \tag{42}$$

With our linear computation we can only determine relative amplitude and phasing of the various physical quantities. An overall complex wave amplitude is arbitrary, but can be estimated using the observed zonal velocity oscillation amplitude. Figure 14 shows angular momentum transports for the nominal case with and without cloud feedback heating. The numerical values for angular momentum transports are for the computed wave scaled to match the observed Galileo zonal velocity amplitude. The profile of $\dot{L}_{u\hat{w}}$ shows that the atmosphere at cloud top levels is accelerated at the expense of the forcing level. In the case with cloud feedback heating the forcing is primarily from the cloud feedback and is located near 50 km. Without cloud feedback heating, the forcing level is that of the external forcing (35 km, see Fig. 3). The profile of $\dot{L}_{uv}$ shows that the equatorial region

is accelerated at the expense of midlatitudes when no cloud feedback heating is present, but reverses sign when cloud feedback heating is added. The correlation coefficient, r_{uv}, in both cases is relatively small. This, and the small value of $\dot{L}_{uv}$ indicates that the horizontal transport of momentum is probably not important for this wave. The vertical transport of angular momentum could be important since it is larger in magnitude, has a relatively high correlation coefficient r_{uw}, and has the correct sense needed to contribute to the maintenance of the cloud top superrotation.

5. SENSITIVITY STUDIES:

To test the sensitivity of the spectrum and wave structure to the details of the basic state, we ran the model with a variety of different basic states. Several different zonal wavenumbers m were also tried. In the following paragraphs we describe the sensitivity of the spectra and wave structure to variations in the basic state variables.

a. Different $\bar{u}(z)$

The major effect of changing the basic state $\bar{u}(z)$ is to Doppler shift spectral peaks in frequency without changing the frequency differences between peaks. In addition, depending on the shape of the $\bar{u}(z)$ profile, additional spectral peaks may appear. The relative amplitudes of spectral peaks may change as well, but usually not much. Therefore, as long as the magnitude of the $\bar{u}$ profile is about the same in the region where wavemodes have significant amplitude, the spectrum is not much affected. Figure 15 illustrates this point by showing spectra using three very different $\bar{u}(z)$ profiles. In the region from 40–55 km, where the wavemodes have significant amplitude, the basic state wind speed is fastest in the constant $\bar{u}$ case and slowest in the Young et. al. (1987) case. The three spectra reflect this ordering. The gravity waves between –50 and –200 m s^{-1} have correspondingly higher phase velocities in the constant $\bar{u}$ case and lower phase velocities in the Young et. al. (1987) case. Thus it seems that the frequency of the spectral peaks we compute has relatively little to do with the details of the $\bar{u}(z)$ profile, and is mainly dependent on the amplitude of $\bar{u}$ where the wave amplitude is significant.

b. Different External Heating

The amplitude, shape, and position of the external heating should have no effect on

the frequency or amplitude of spectral peaks if we are really looking at free waves. But, since we are imperfectly isolating the "free wave" component of forced waves the shape and amplitude of the external heating will affect the relative amplitudes of different free wave modes that are excited. For effective forcing of the waves there needs to be some significant amount of overlap between the external heating profile $Q_{ext}(z)$ and the vertical structure of the wavemode. The shape and amplitude of the external forcing will set the relative amplitudes between free wave components in the forced wave. However, as long as the first condition is met, the frequency and vertical structures of free wave components are nearly unaffected (up to a complex scaling factor) by the details of the external forcing. Figure 16 shows spectra for three very different forcings. Although the relative amplitude of spectral peaks varies, the frequency differences between spectral peaks, and the associated vertical structure of wavemodes remains very nearly the same. This gives us confidence that our procedure for separating the free wave component is acceptable.

c. Different $f(z)$

The nominal profile of $f(z)$ given in Fig. 4 was chosen to simulate the expected cloud feedback heating caused by vertical motions associated with the wave. The general shape of $f(z)$ is set by the physics of the problem. Because we are considering the optically thick absorption of infrared emission from below, we must have $f(z) > 0$ below the cloud base, and $f(z) < 0$ above. Also, the vertical integral of $f(z)$ must be zero for an optically thick cloud. We have experimented with several different $f(z)$ profiles. These experiments show that it is the $f(z) < 0$ part of the profile that creates the instability, and that the exact shape of $f(z)$ has little effect on spectra. Increasing the width of $f(z)$ has much the same effect as increasing β as long as $f(z)$ has a vertical scale not too much larger than a scale height. We have chosen the width of $f(z)$ to be about one-half of a scale height to be consistent with the width of the thick lower cloud (Knollenberg and Hunten, 1980).

d. Higher m

For higher values of the longitudinal wavenumber m instabilities can also exist. We have found that the critical value of β for the onset of instability is nearly independent of m for $m < 10$, and then becomes large for $m > 10$. Thus we expect wavemodes with

smaller scale structure to exist in addition to the $m = 1$ wavemodes. Figure 17 shows the vertical and horizontal structure of the zonal wind component of waves for m =1, 4, and 11 (nominal basic state with cloud feedback heating added). The wavemodes with higher m are confined to deeper levels and have smaller amplitudes than the $m = 1$ wavemode at 65–70 km where the violet features are thought to be formed. Wavemodes with higher m are also more confined in latitude. While the $m = 1$ wavemode appears to have the largest amplitude at 65–70 km, other wavemodes with small m have amplitudes nearly as large. The apparent dominance of the $m = 1$ wavemode in the Galileo data cannot be explained by the simple feedback and artificial forcing of our computation alone. A more realistic forcing function or a slightly different $\bar{u}(z)$ may match the vertical structure of the $m = 1$ wavemode better, or perhaps another mechanism not modeled by our computation is necessary to more clearly select the $m = 1$ wavemode. The frequency of sampling in the Galileo data is only once per day during the second half of the data set (see figure 1). Therefore, although we have not observed the signature of $m > 1$ wavemodes, we do not expect to see wavemodes higher than $m = 2$ in our analysis of the Galileo data. Certainly at the cloud base wavemodes with higher m may have significant amplitude, and indeed small-scale structure in the near infrared has been observed both in ground-based observations (Crisp et al. 1991) and in Galileo NIMS maps (Carlson et al. 1991).

6. DISCUSSION:

a. The "Y" feature:

In an earlier paper we postulated that the midlatitude streaky pattern of clouds seen on Venus is attributable to the formation of clouds near the equator and the subsequent poleward advection and shearing of the clouds by the winds (Schinder et al. 1990). Expanding on that idea, we perform a numerical experiment where we release clouds at random locations near the equator, and let the measured Galileo Venus mean wind (Belton et al. 1991) and a superimposed wave advect them forward. Figure 18 shows the results of this experiment using the phase speed of the most unstable wavemode, and values for the zonal and meridional wave amplitudes and phasing chosen to be consistent with the results of the 3-D spherical geometry computation and with Galileo wind velocity measurements.

The maximum zonal wave amplitude used is 10 m s^{-1} (at the equator) to be consistent with Galileo Venus wave measurements (Smith et al, 1992). The maximum meridional amplitude and phases are then obtained from the computation. The maximum westward perturbation in zonal velocities follows the maximum northward perturbation in meridional velocities by 90 degrees in the northern hemisphere. Galileo observations show that the maximum westward wave velocity is found near the dark vertex of the "Y" feature. Thus, this choice of phasing is also consistent with the findings of Del Genio and Rossow (1990). We see a modulation of the cloud shapes and orientations of the cloud streaks at midlatitudes caused by the wave which are similar to those seen in the observations shown in Fig. 19. This suggests the idea that the "Ψ" or "Y" feature is caused by the wave modulating the advective patterns of the clouds.

b. General Comments:

Atmospheric resonances at long wavelengths are common. Whenever there is a forcing layer and some atmospheric structure, for a given wavenumber some frequencies will be picked out which "fit" the atmosphere and the boundary conditions particularly well. The atmospheric structure can be formed by either variations in the stability profile, or by wind shear. In the Venus atmosphere, structure in the stability profile is the largest factor which determines which frequencies are preferred. Wind shear acts mainly to modify the strength and to shift spectral peaks by the Doppler effect.

The existence of resonances does not necessarily mean that a particular resonance will be excited. The external thermal forcing we use here is an artifact to excite waves. A more realistic forcing may well pick out only certain wavemodes, leaving others unexcited. Indeed, the cloud feedback heating picks out only the wavemode at –102 m s^{-1} and has very little effect on other wavemodes.

The reason that the cloud feedback picks out the wavemode with phase speed –102 m s^{-1} is the location of the Venus cloud and its relation to the static stability profile. The fact that the phase speed is very nearly equal to the maximum $\bar{u}(z)$ is coincidence, as far as the present computation is concerned. When the basic state $\bar{u}(z)$ is set to a constant –50 m s^{-1}, for example, the cloud feedback picks out the wavemode with the same vertical

structure even though it no longer has a phase speed very near $\bar{u}$. Since the cloud feedback heating profile function $f(z)$ has a node at 49 km (altitude of the cloud base), those vertical profiles that also have a node at or near 49 km will have less cancellation and will maximize the cloud feedback effect. Looking back at Fig. 17 we see that at $m = 11$ (dashed line) the cloud feedback has picked out the wavemode with three nodes in the vertical where for $m = 1, 4$ the wavemode with two nodes in the vertical is the most unstable. At $m = 11$ the waves are more confined in altitude and it happens that the wavemode with more vertical structure is the one with a node near 49 km. Too much vertical structure will damp wavemodes by diffusion, so those wavemodes with the combination of a moderate vertical structure (two or three nodes in the vertical) and a node near 49 km are picked out by the cloud feedback effect. For the Venus static stability (which determines the vertical structure of wavemodes) and wind speed (which Doppler shifts wavemodes), these two conditions are met only for the wavemode at phase speed –102 m s^{-1}.

The oscillation of wind velocities seems to be sporadic in nature. In the Galileo data set the wave is very pronounced (Belton et al. 1991), but at times during the Pioneer Venus mission no wave is detected (Del Genio and Rossow 1990). Our calculation shows that the amplitude of the most unstable wavemode varies strongly with height. It is possible that variation in the level of the cloud top contributes to the irregularity of the observed wind oscillations. A variation in the zonal wind profile, or in the trapping properties of the atmosphere could also play a role in causing the wave to appear sometimes, but not to appear at other times. Our analysis of Pioneer Venus images shows that velocity oscillations may appear for a few days, disappear, then reappear with a phasing unrelated to the previously observed oscillation. This sort of behavior is consistent with the low "Q" associated with the waves in our computation.

Energy sources other than cloud feedback are possible. Instability of horizontal shear is an obvious candidate excluded by assumption from the modeling reported here. Baroclinic instability is also not possible given the assumptions of our model. The key point is that a low order global wavemode that appears to have the correct kinematical properties has been identified. In the absence of a forcing mechanism it is estimated to decay with

about a 20 day time scale. Cloud feedback seems to have the right magnitude to provide the forcing, and also seems to pick out the correct phase velocity for the most unstable wavemode, but we have not excluded other possibilities for excitation.

Acknowledgments. This work has been supported by the NASA Planetary Atmospheres Program, the Pioneer Venus Project, and the NASA Graduate Student Researchers Program. The computations were performed at the Cornell National Supercomputer Facility, which is supported by Cornell University, IBM, and the National Science Foundation.

References

Baker, N. L., and C. B. Leovy, 1987: Zonal Winds near Venus' Cloud Top Level: A Model Study of the Interaction between the Zonal Mean Circulation and the Semidiurnal Tide. *Icarus*, **69**, 202–220.

Belton, M.J.S., G. R. Smith, G. Schubert, and A. D. DelGenio, 1976: Cloud Patterns, Waves and Convection in the Venus Atmosphere. *J. Atmos. Sci.*, **33**, 1394–1417.

Belton, M.J.S., P.J. Gierasch, M.D. Smith, P. Helfenstein, P.J. Schinder, J.B. Pollack, K.A. Rages, A.P. Ingersoll, K.P. Klaasen, J. Veverka, C.D. Anger, M.H. Carr, C.R. Chapman, M.E. Davies, F.P. Fanale, R. Greeley, R. Greenberg, J.W. Head III, D. Morrison, G. Neukum, and C. Pilcher, 1991: Images from Galileo of the Venus Cloud Deck. *Science*, **253**, 1531–1536.

Carlson, R. W., K. H. Baines, Th. Encrenaz, F. W. Taylor, P. Drossart, L. W. Camp, J. B. Pollack, E. Lellouch, A. D. Collard, S. B. Calcutt, D. Grinspoon, P. R. Weissman, W. D. Smythe, A. .C. Ocampo, G. E. Danielson, F. P. Fanale, T. V. Johnson, H. H. Kieffer, D. L. Matson, T. B. McCord and L. A. Soderblum, 1991: Galileo infrared imaging spectroscopy measurements at Venus. *Science*, **253**, 1541–1548.

Chapman, S. and R. S. Lindzen 1970: *Atmospheric Tides; Thermal and Gravitational.* Gordon and Breach Science Publishers Inc., New York, 130–156.

Councelman, C. C. III, S. A. Gourevitch, R. W. King, G. B. Loriot, and E. Sinsberg, 1980: Zonal and meridional circulation of the lower atmosphere of Venus determined by radio interferometry. *J. Geophys. Res.*, **85**, No. A13, 8026–8030.

Covey, C., and G. Schubert, 1982: Planetary-Scale Waves in the Venus Atmosphere. *J. Atmos. Sci.*, **39**, 2397–2413.

Crisp, D., 1989: Radiative forcing of the Venus mesosphere. II. Thermal fluxes, cooling rates, and radiative equilibrium temperature. *Icarus*, **77**, 391–413.

Crisp, D., S. McMuldroch, S. K. Stephens, W. M. Sinton, B. Ragent, K.-W. Hodapp, R. G. Probst, L. R. Doyle, D. A. Allen, and J. Elias, 1991: Overview of Ground-Based Near-Infrared Imaging Observations of Venus during the Galileo Encounter. *Science*,

253, 1538–1541.

Del Genio, A. D., and W. B. Rossow, 1982: Temporal Variability of Ultraviolet Cloud Features in the Venus Stratosphere. *Icarus*, **51**, 391–415.

Del Genio, A. D., and W. B. Rossow, 1990: Planetary-Scale Waves and the Cyclic Nature of Cloud Top Dynamics on Venus *J. Atmos. Sci.*, **47**, 293–318.

Dongarra, J. J., J. R. Bunch, C. B. Moler, and G. W. Stewart, 1979: *LINPACK Users' Guide.* Society for Industrial and Applied Mathematics, Philadelphia, 2.1–2.12.

Fels, S. B., 1986: An Approximate Analytical Method for Calculating Tides in the Atmosphere of Venus. *J. Atmos. Sci.*, **43**, 2757–2772.

Ghan, S. J., 1989: Unstable Radiative-Dynamic Interactions. Part I: Basic Theory. *J. Atmos. Sci.*, **46**, 2528–2561.

Gierasch, P. J., A. P. Ingersoll, and R. T. Williams, 1973: Radiative Instability of a Cloudy Planetary Atmosphere. *Icarus*, **19**, 473–481.

Hou, A. Y., S. B. Fels, R. M. Goody, 1990: Zonal Superrotation above Venus' Cloud Base Induced by the Semidiurnal Tide and the Mean Meridional Circulation. *J. Atmos. Sci.*, **47**, 1894–1901.

Knollenberg, R. G., and D. M. Hunten, 1980: The Microphysics of the Clouds of Venus: Results of the Pioneer Venus Particle Size Spectrometer Experiment. *J. Geophys. Res.*, **85**, No. A13, 8039–8058.

Knollenberg, R. G., L. Travis, M. Tomasko, P. Smith, B. Ragent, L. Esposito, D. McCleese, J. Martonchik, and R. Beer, 1980: The Clouds of Venus: A Synthesis Report. *J. Geophys. Res.*, **85**, No. A13, 8059–8081.

Lamb, H., 1890: On Atmospheric Oscillations. *Proc. Roy. Soc. Lon. A.*, **84**, 551–572.

Leovy, C. B., 1966: Photochemical destabilization of gravity waves near the mesopause. *J. Atmos. Sci.*, **23**, 223–232.

Leovy, C. B., 1987: Zonal Winds near Venus' Cloud Top Level: An Analytical Model of the Equatorial Wind Speed. *Icarus*, **69**, 193–201.

Lindzen, R. S., 1967: Thermally Driven Diurnal Tide in the Atmosphere. *Q. J. R. Mete-*

orol. Soc., **93**, 18–42.

Longuet-Higgins, M. S., 1968: The Eigenfunctions of Laplace's Tidal Equations over a Sphere. *Philos. Trans. R. Soc. London. Ser. A*, **262**, 511–607.

Newman, M., and C. Leovy, 1992: Maintenance of Strong Rotational Winds in Venus' Middle Atmosphere by Thermal Tides. *Science*, **257**, 647–650.

Pechmann, J. B., and A. P. Ingersoll, 1984: Thermal Tides in the Atmosphere of Venus: Comparison of Model Results with Observations. *J. Atmos. Sci.*, **41**, 3290–3313.

Schinder, P. J., P. J. Gierasch, S. S. Leroy, and M. D. Smith, 1990: Waves, Advection, and Cloud Patterns on Venus. *J. Atmos. Sci.*, **47**, 2037–2052.

Seiff, A., D. B. Kirk, R. E. Young, R. C. Blanchard, J. T. Findlay, G. M. Kelly, and S. C. Sommer, 1980: Measurements of Thermal Structure and Thermal Contrasts in the Atmosphere of Venus and Related Dynamical Observations: Results From the Four Pioneer Venus Probes. *J. Geophys. Res.*, **85**, No. A13, 7903–7933.

Smith, M. D., P. J. Gierasch, and P. J. Schinder, 1992: A Global Traveling Wave on Venus. *Science*, **256**, 652–655.

Young, R. E., R. L. Walterscheid, G. Schubert, and A. Seiff, 1987: Characteristics of Gravity Waves Generated by Surface Topography on Venus: Comparison with the VEGA Balloon Results. *J. Atmos. Sci.*, **44**, 2628–2639.

Figure captions

Fig. 1. Wind measurements from the Galileo data (Belton et al. 1991). The data is shown as a time series for three latitude bands. An oscillation with a period of about 4 days and an amplitude of about 10 m s^{-1} is evident in all three bands.

Fig. 2. Vertical structure of the Brunt-Väisälä frequency $N^2(z)$ and zonal wind speed $\bar{u}(z)$ used for the nominal case.

Fig. 3. Nominal case vertical structure of the other basic state variables.

Fig. 4. Vertical profile of $f(z)$ function for the case with cloud feedback heating.

Fig. 5. The response of the system is shown as a function of frequency for the nominal case with $m = 1$ and no cloud feedback heating.

Fig. 6. Vertical structure of the free wave zonal kinetic energy component of four low wavemodes with phase speeds of -295 (dotted line) , -156 (solid line), -102 (dash-dot), and -85 (dashed line) m s^{-1} for the nominal basic state

Fig. 7. Same as Fig. 5, except that a cloud feedback heating has been added with strength $\beta = \beta_{\text{crit}}$. The two spectra are nearly identical except in the region around the most unstable wavemode at -102 m s^{-1}.

Fig. 8. Vertical structure of the free mode component of the most unstable wavemode (phase speed of -102 m s^{-1}) with $\beta = \beta_{\text{crit}}$. The solid line shows zonal velocity and phase, and the dashed line shows meridional velocity and phase. The zonal velocities are taken at the equator while the meridional velocities are taken at 30 degrees north latitude and are multiplied by ten. The overall scaling is arbitrary, but the relative scaling between zonal and meridional velocities is correct. The phases of the zonal and meridional components are shown relative to the longitude where the oscillation is completely real and positive (eastward/southward).

Fig. 9. Horizontal structure of the wavemode shown in Fig. 8. Again the solid line shows horizontal velocity and phase, and the dashed line shows meridional velocity and phase. The relative amplitudes between the zonal and meridional components are correct (there has been no multiplication of the meridional component), but the

overall scaling is arbitrary. The horizontal structure has been taken at a pressure scale height of 6.5 (63 km). The phase of the waves has the same meaning as in Fig. 8.

Fig. 10. Spectrum for an atmosphere with constant basic state zonal wind speed of –50 m s^{-1} (indicated by dotted line). In this case the radiative time constant has been set to be very long, and the diffusion has been lowered as much as numeric stability will allow. The small "peak" at –150 m s^{-1} is an artifact. Peaks between –50 and –150 m s^{-1} are gravity waves, as are the peaks between 0 and 50 m s^{-1}. The small peaks and "shoulders" in the spectrum between –50 and –38 m s^{-1} are Rossby waves.

Fig. 11. Estimate of the error for the nominal case with $\beta = \beta_{\text{crit}}$.

Fig. 12. Spectrum of $m = 1$ nominal case energetics for the cases with (top) and without (bottom) cloud feedback heating of strength $\beta = \beta_{\text{crit}}$. The solid line shows the external heating rate, the short dashed line shows the cloud feedback heating rate, the dash-dot line shows the rate of thermal diffusion, and the dotted line shows the rate of cooling by radiation. The total of other sources and sinks of energy are shown by the long dashed line. The cloud feedback heating is only important in the region near the most unstable wavemode. For $\beta = \beta_{\text{crit}}$ all other wavemodes show decay in time.

Fig. 13. Growth rate as a function of β. In this representation, a local maximum in the growth rate corresponds to a spectral peak in previous figures. The solid line shows the growth rate for the nominal basic state ($\beta = 0$) in the region around the most unstable wavemode. The dashed line shows the growth rate for $\beta = \beta_{\text{crit}}$, and the dotted line shows the growth rate for $\beta = \beta_{\text{crit}}/2$. Two things are apparent: the effect of the parameter β is only roughly linear, and the effect of the cloud feedback heating is concentrated in a small region of frequency around the most unstable wavemode (–102 m s^{-1}).

Fig. 14. Vertical and horizontal momentum transports for the most unstable wavemode with and without cloud feedback heating. The top two figures show $< u'w' >$ angular momentum transport averaged over latitude and longitude which is the angular momentum transported per second through a surface at a given height. The bottom

two figures show $< u'v' >$ angular momentum transport averaged over height and longitude which is the angular momentum transported per second through a surface at a given latitude.

Fig. 15. Spectra for three different $\bar{u}(z)$ profiles. The solid line (in both plots) is the nominal case. The dashed line is the Young et al. (1987) profile. The frequencies of wavemodes shift according the value of $\bar{u}(z)$ in the region where the wavemode has significant amplitude. The overall shape of $\bar{u}(z)$ may change the relative amplitudes of wavemodes, but does not significantly change the frequency difference between wavemodes.

Fig. 16. Spectrum for three different external heating profiles. The solid line (in both plots) shows the nominal case values. Even vastly different profiles (dotted and dashed lines) for the external heating do not affect the frequencies (or free mode structure) of wavemodes significantly. Different external heating profiles do, however, excite different wavemodes more effectively which changes the relative amplitudes of wavemodes somewhat. Therefore, the nominal case external heating was chosen to be a broad profile which would excite all wavemodes.

Fig. 17. Vertical and horizontal structure as a function of m. For each m, the most unstable wavemode was chosen. The solid line is $m = 1$, the dotted line $m = 4$, and the dashed line $m = 11$. For higher m, the wavemodes become more confined in altitude and in latitude.

Fig. 18. Simulated cloud pattern. Circular clouds are released at random longitudes near the equator, and are then advected under the influence of the mean flow with an added wave. The mean flow is as measured from Galileo images (Belton et al. 1991) and includes poleward drift and midlatitude jets. The added wave has structure and phase velocity consistent with the computed structure of the most unstable wavemode, and an amplitude consistent with Galileo observations.

Fig. 19. Simple cylindrical projection of a set of Galileo images taken as the cloud system rotated under the spacecraft.

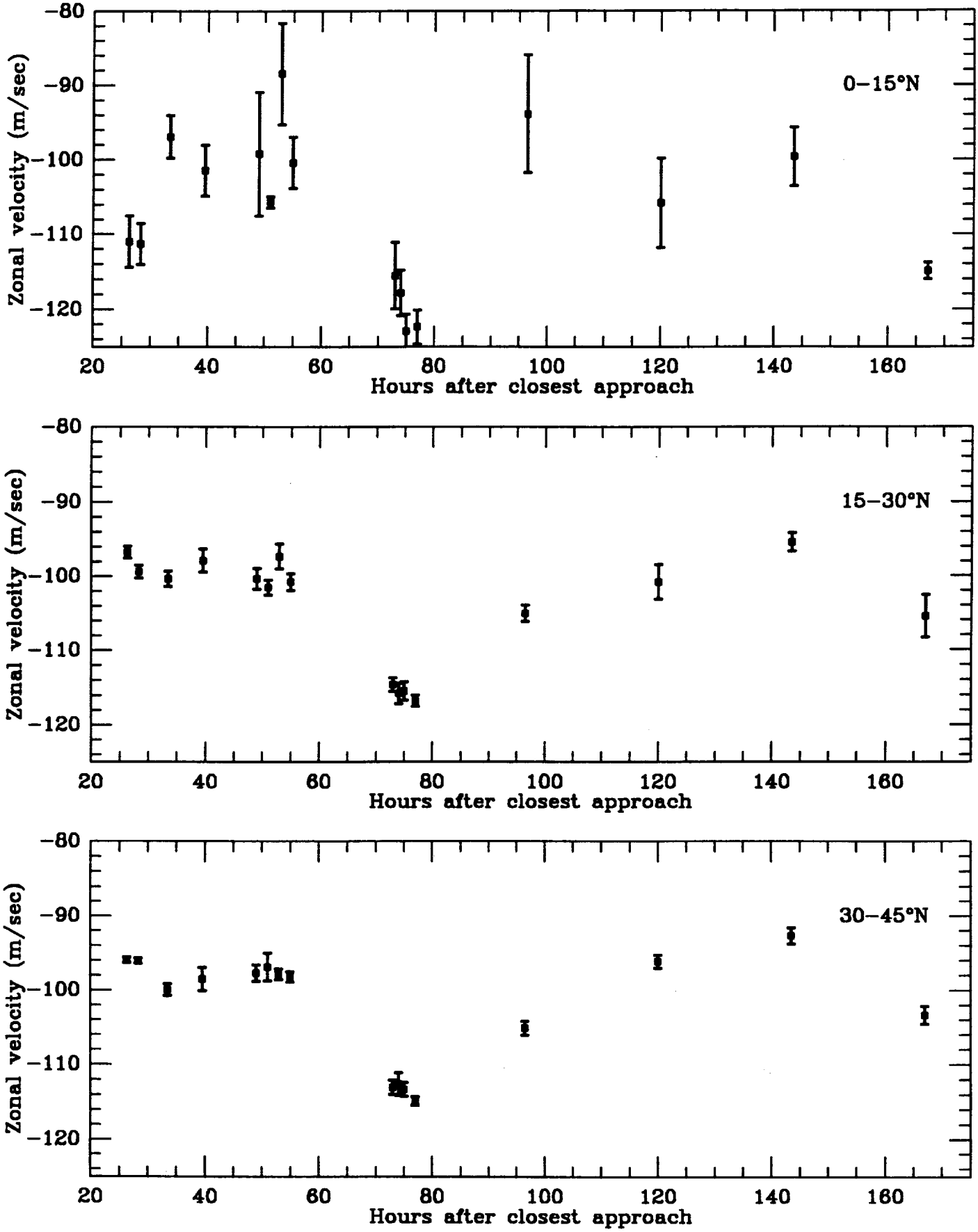
0–15°N
15–30°N
30–45°N
Zonal velocity (m/sec)
Hours after closest approach
−80
−90
−100
−110
−120
20
40
60
80
100
120
140
160

Fig. 1

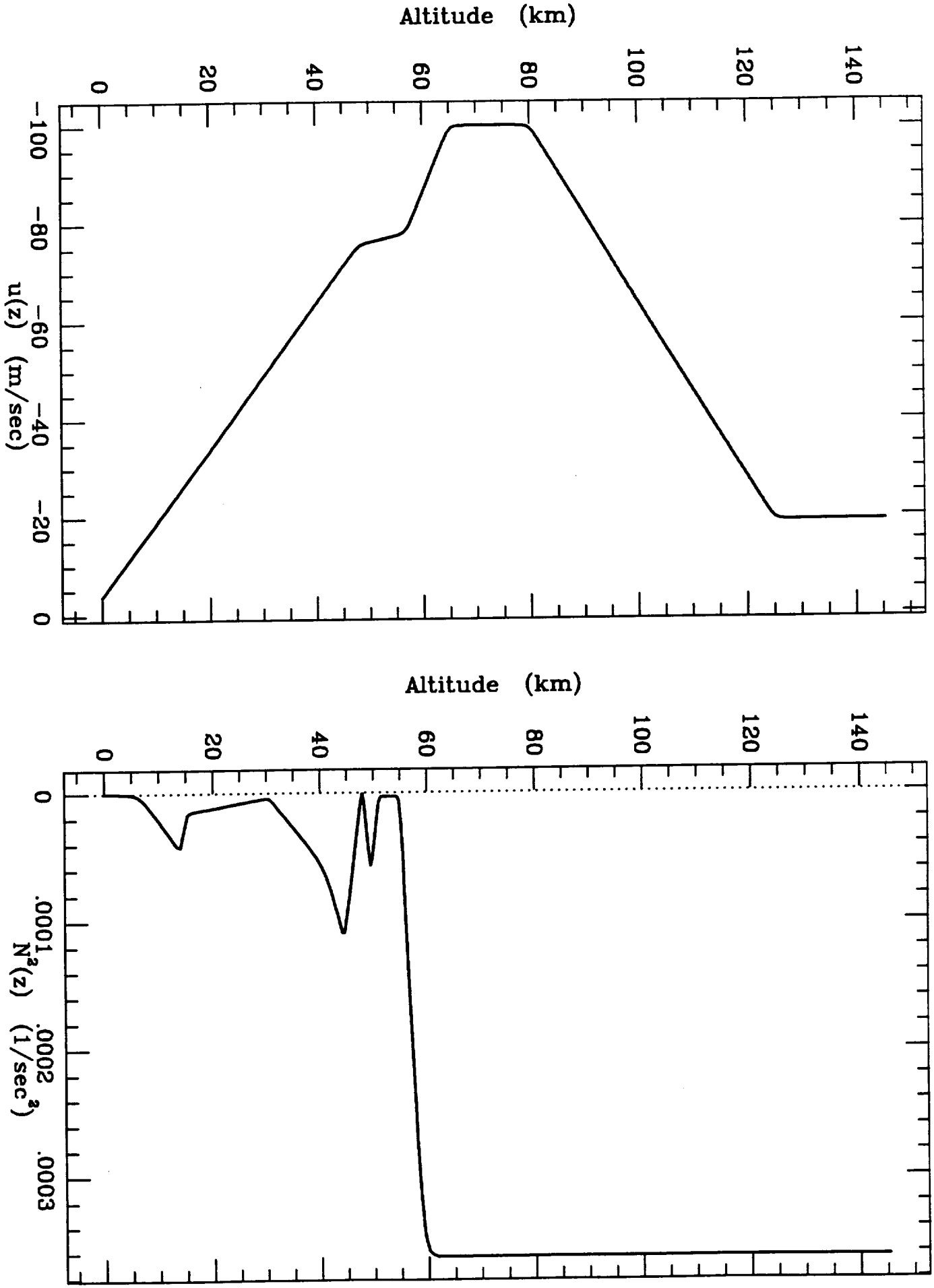
Altitude (km)
0
20
40
60
80
100
120
140
u(z) (m/sec)
-100
-80
-60
-40
-20
0
Altitude (km)
0
20
40
60
80
100
120
140
N²(z) (1/sec²)
0
.0001
.0002
.0003

Fig. 2

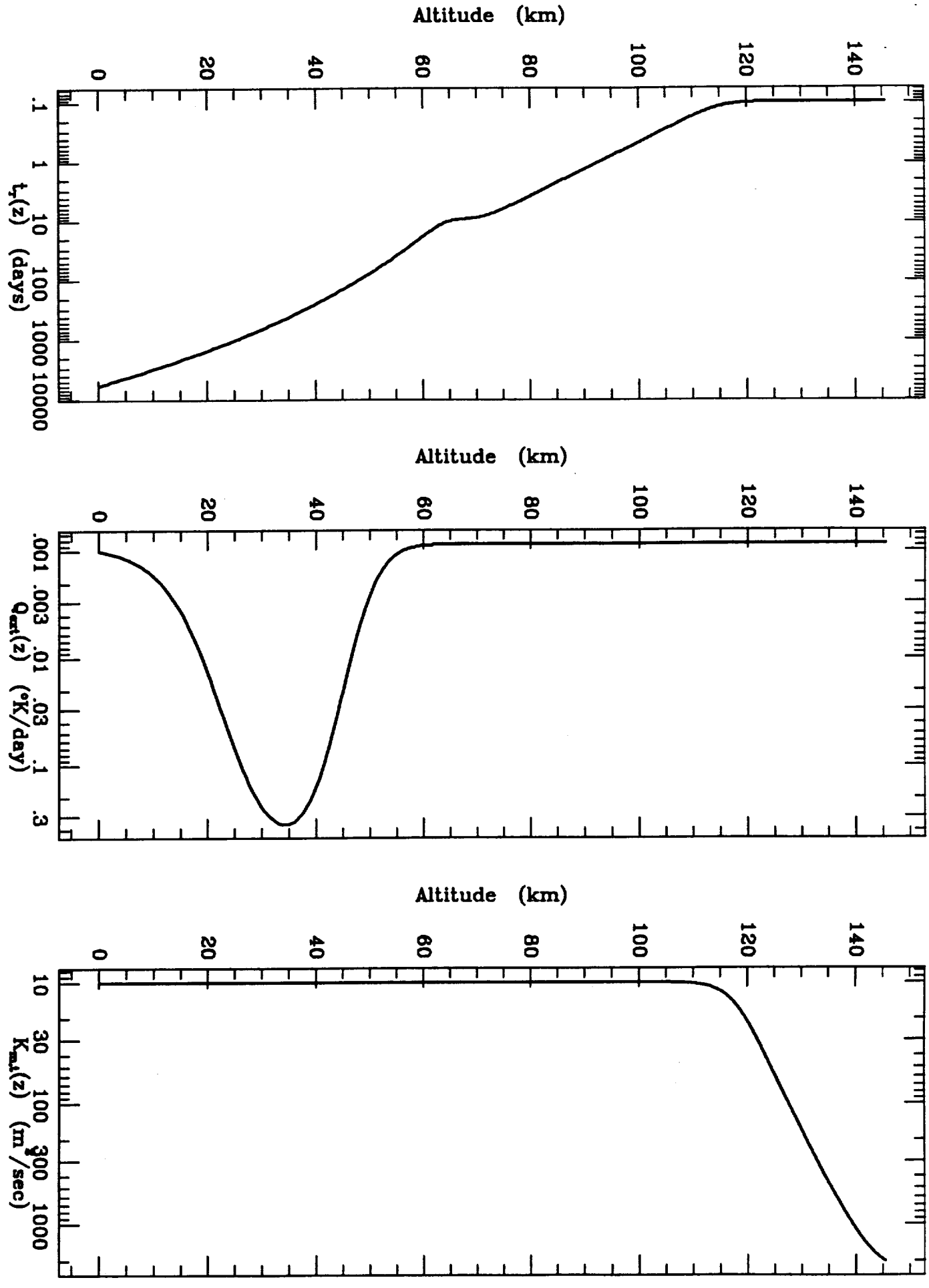
Altitude (km)
0
20
40
60
80
100
120
140
.1
1
10
100
1000
10000
$t_r(z)$ (days)
Altitude (km)
0
20
40
60
80
100
120
140
.001
.003
.01
.03
.1
.3
$Q_{rad}(z)$ (°K/day)
Altitude (km)
0
20
40
60
80
100
120
140
10
30
100
300
1000
$K_{mol}(z)$ (m²/sec)

Fig. 3

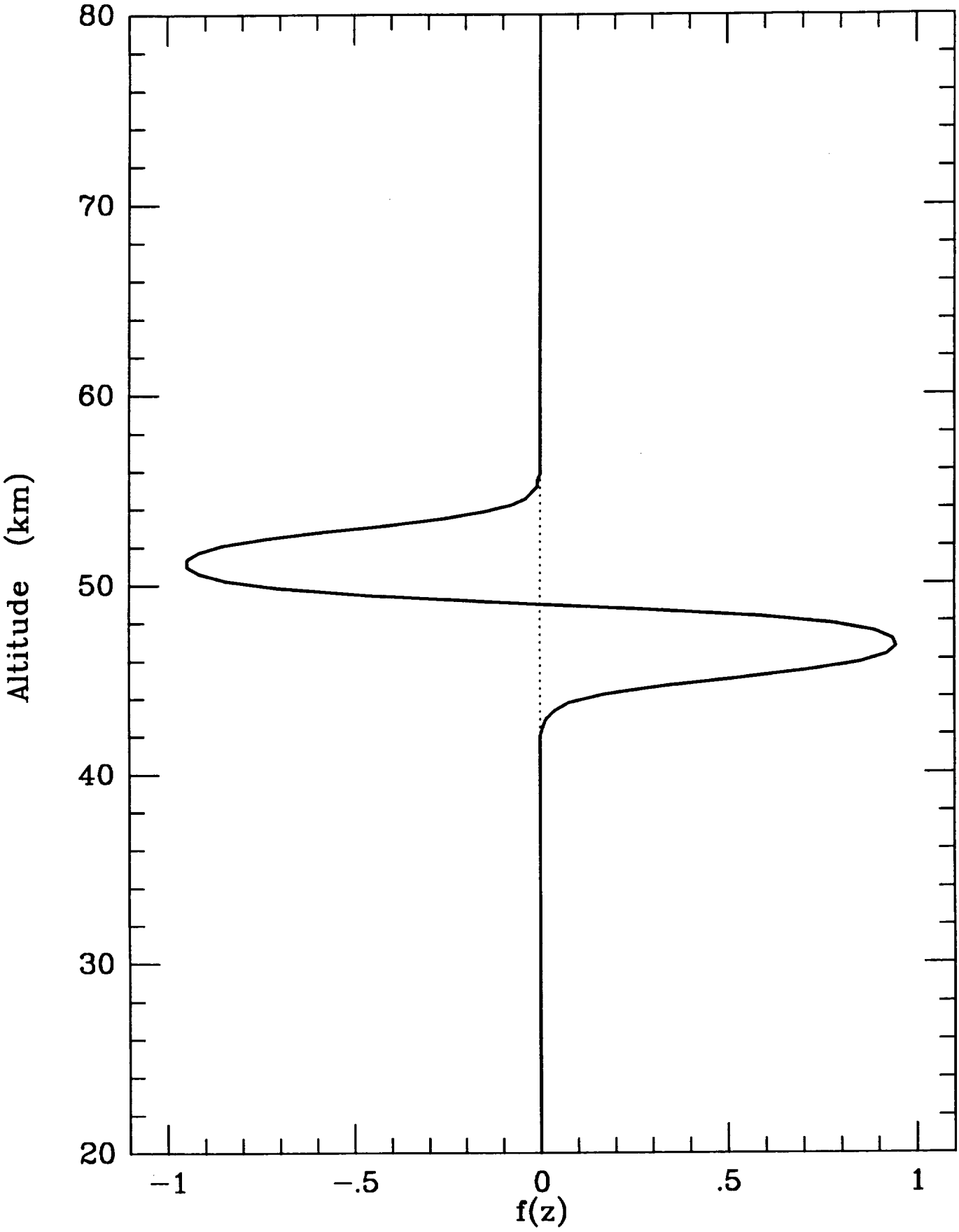

Fig. 4

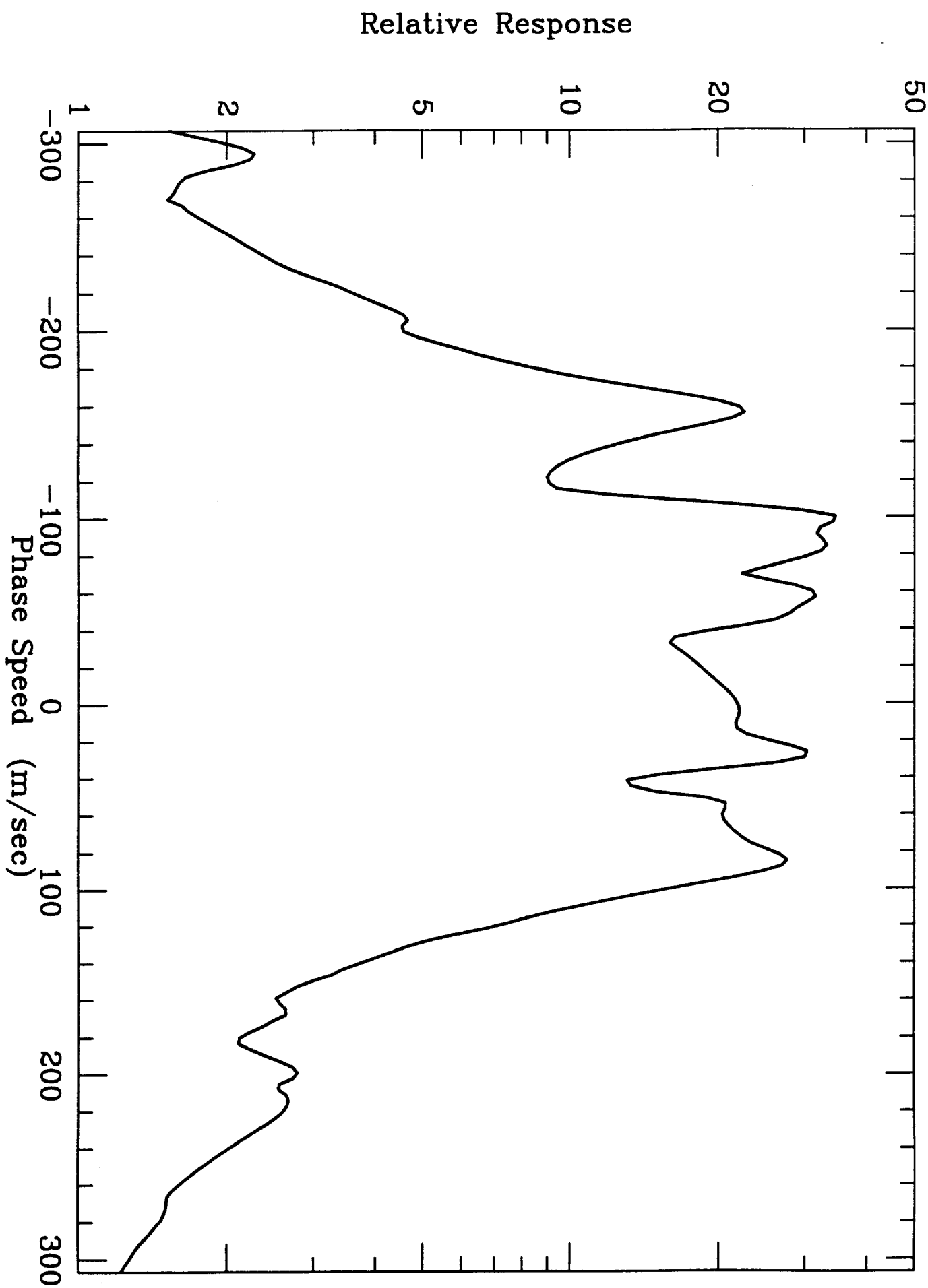
Relative Response
1
2
5
10
20
50
−300
−200
−100
0
100
200
300
Phase Speed (m/sec)

Fig. 5

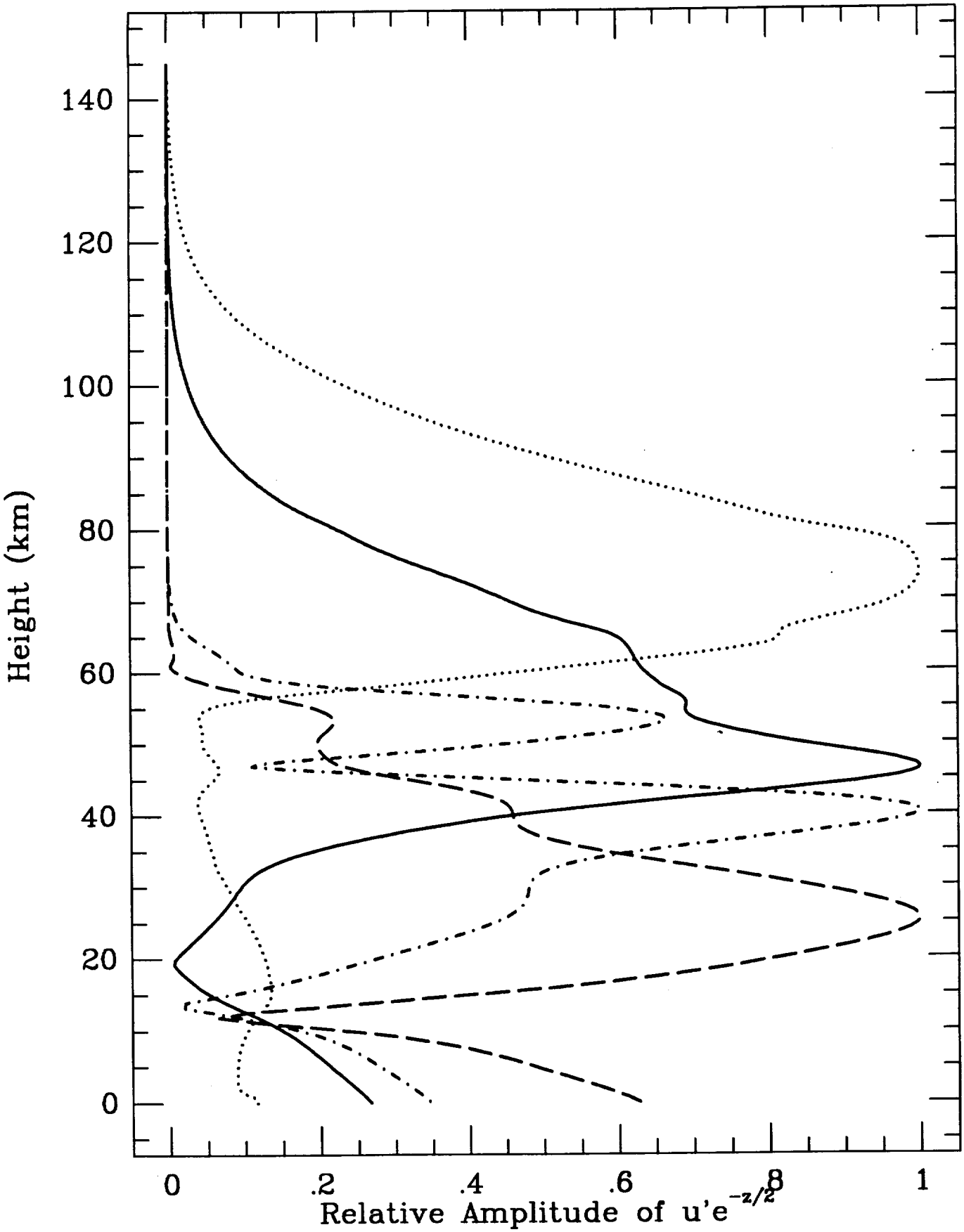
140
120
100
80
60
40
20
0
Height (km)
0
.2
.4
.6
.8
1
Relative Amplitude of u'e^-z/2

Fig. 6

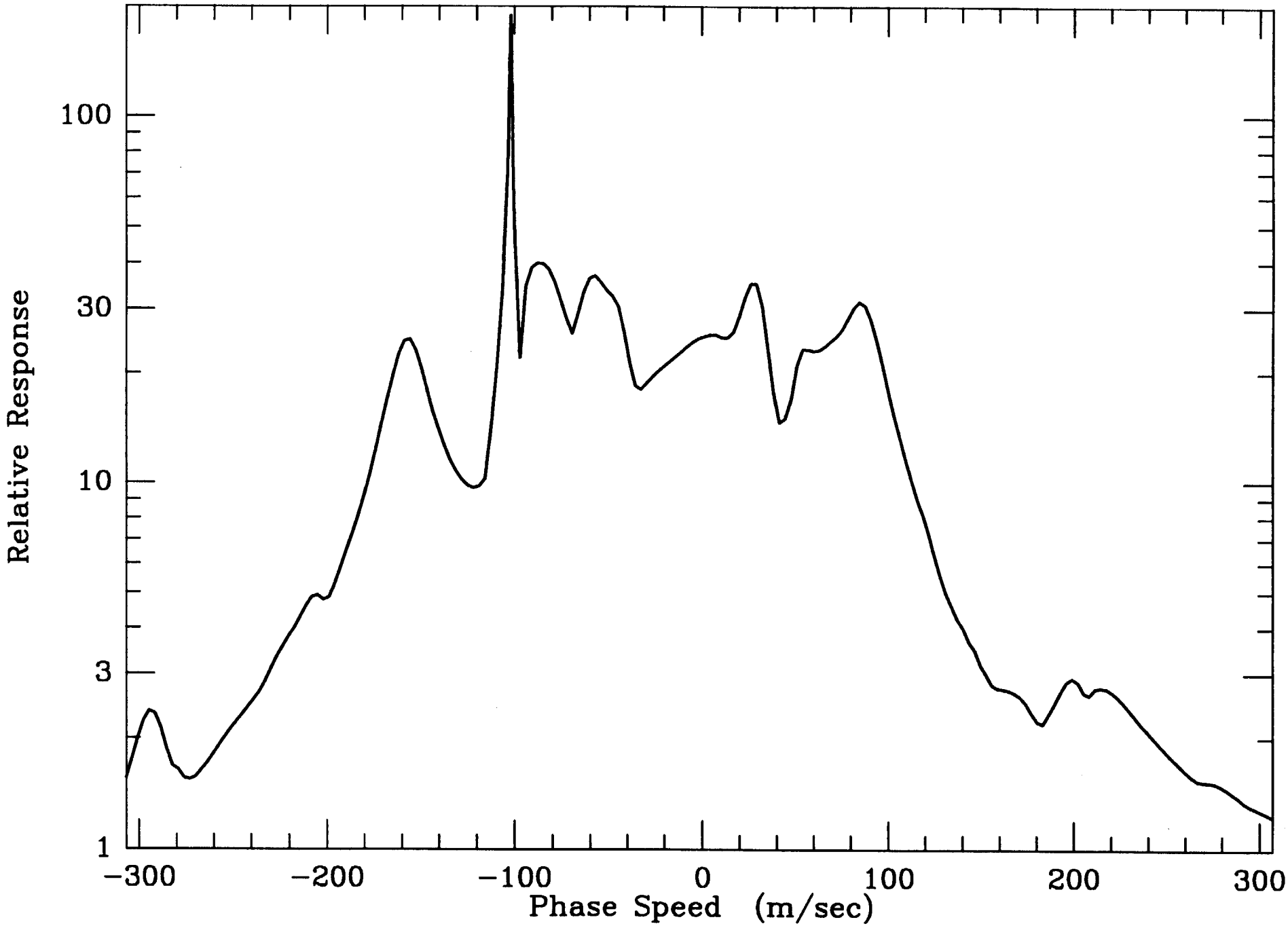
Relative Response
100
30
10
3
1
−300
−200
−100
0
100
200
300
Phase Speed (m/sec)

Fig. 7

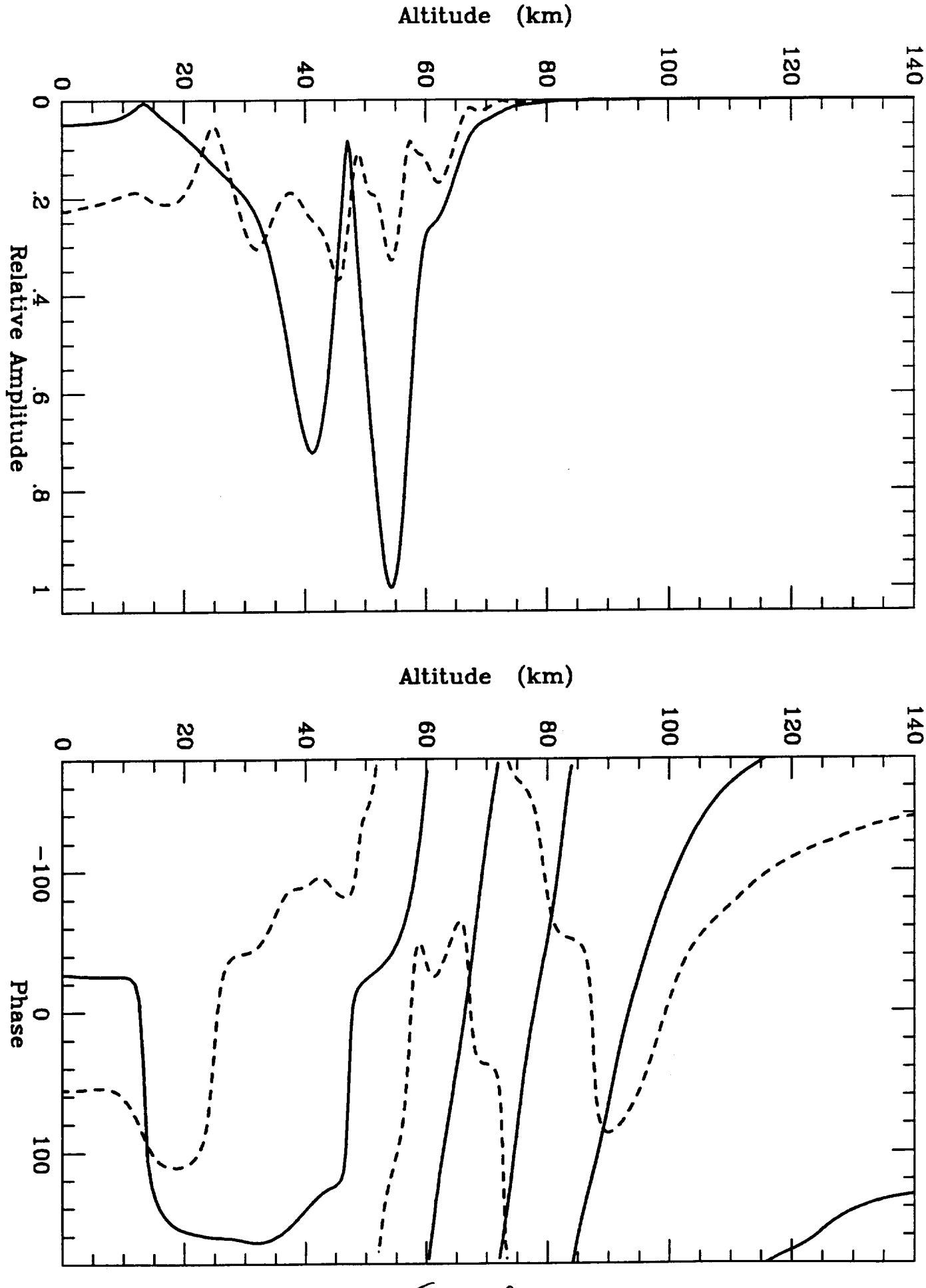
Altitude (km)
0
20
40
60
80
100
120
140
Relative Amplitude
0
.2
.4
.6
.8
1
Altitude (km)
0
20
40
60
80
100
120
140
Phase
-100
0
100

Fig. 8

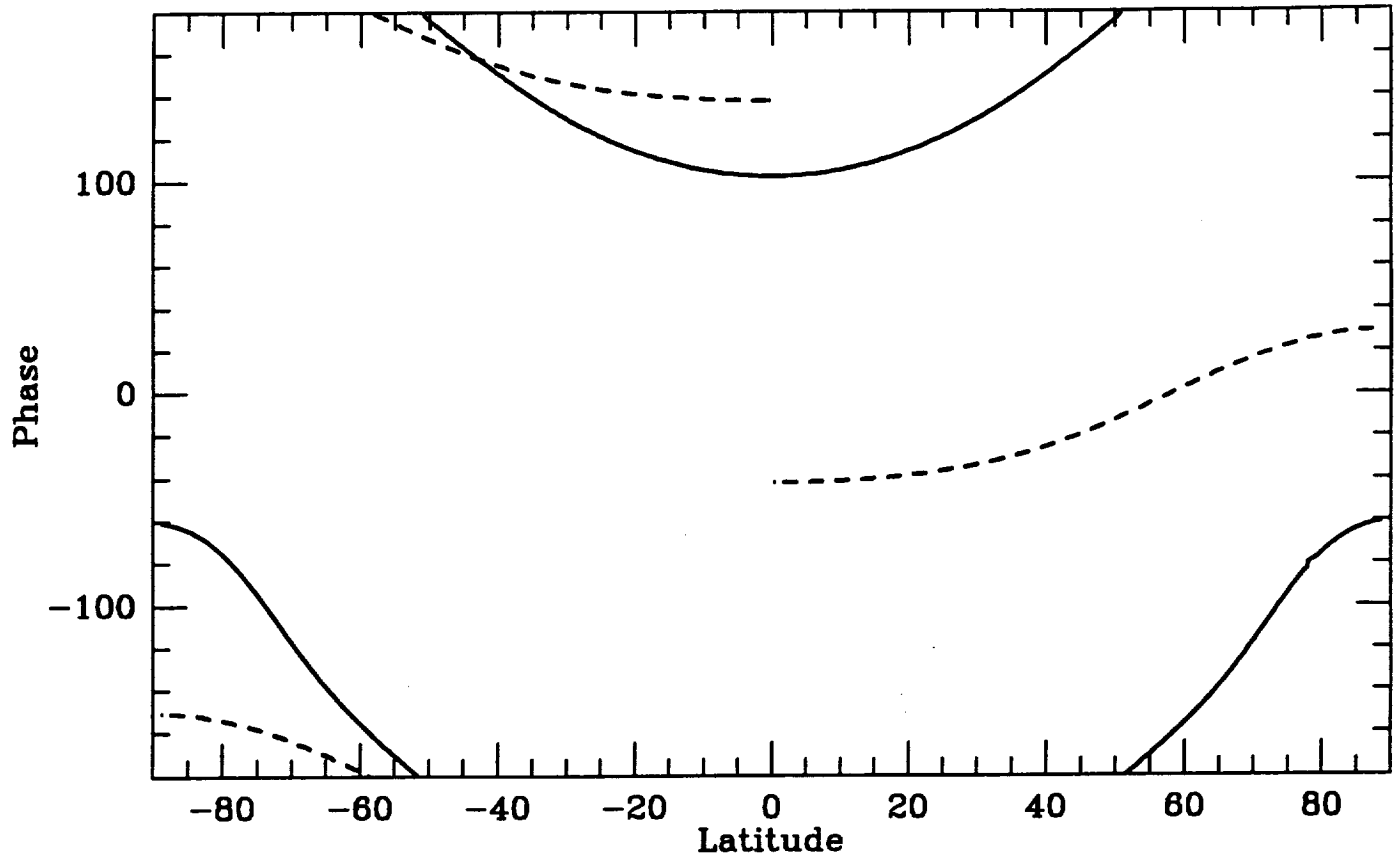
Phase
100
0
−100
−80
−60
−40
−20
0
20
40
60
80
Latitude

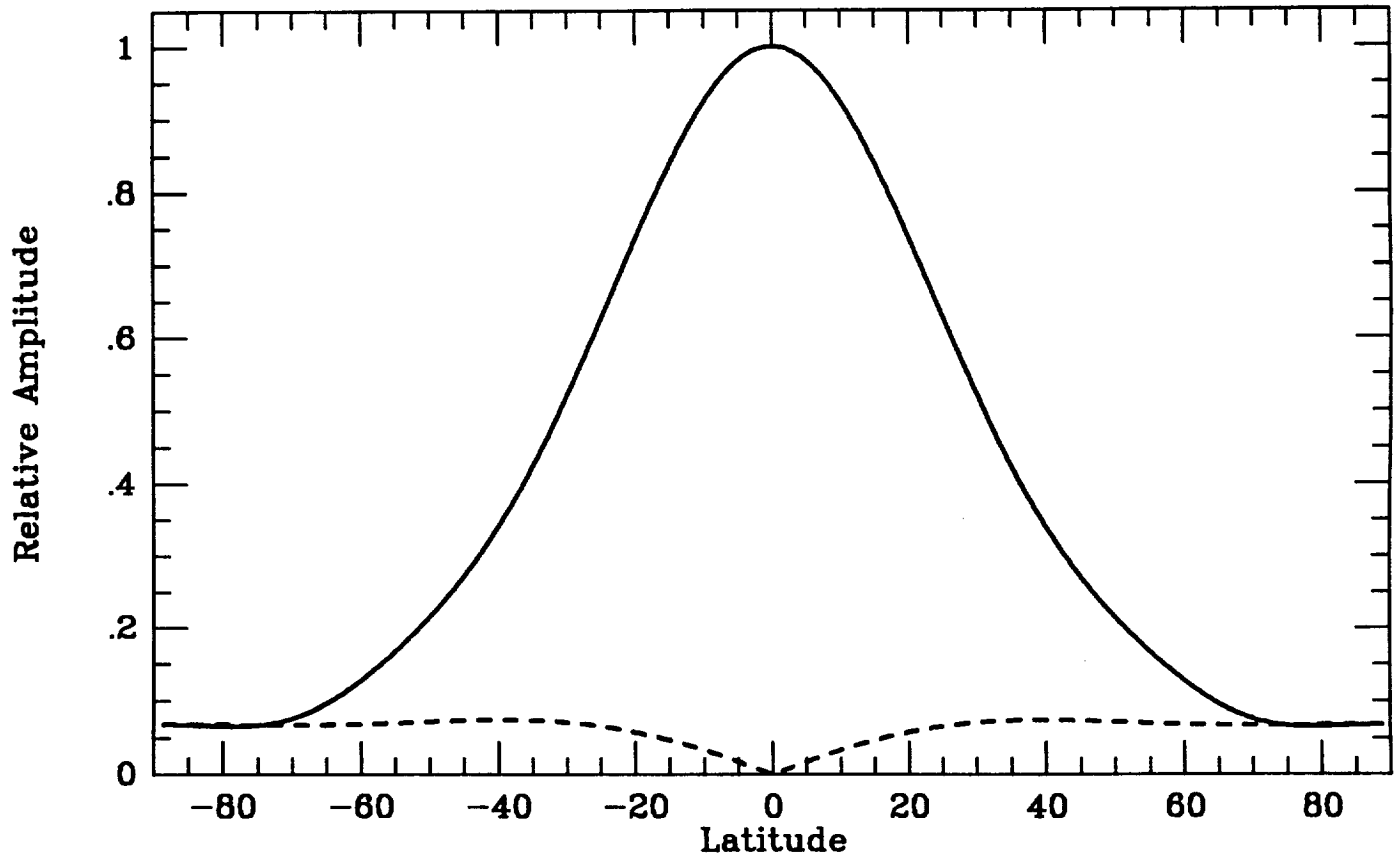
Relative Amplitude
1
.8
.6
.4
.2
0
−80
−60
−40
−20
0
20
40
60
80
Latitude

Fig. 9

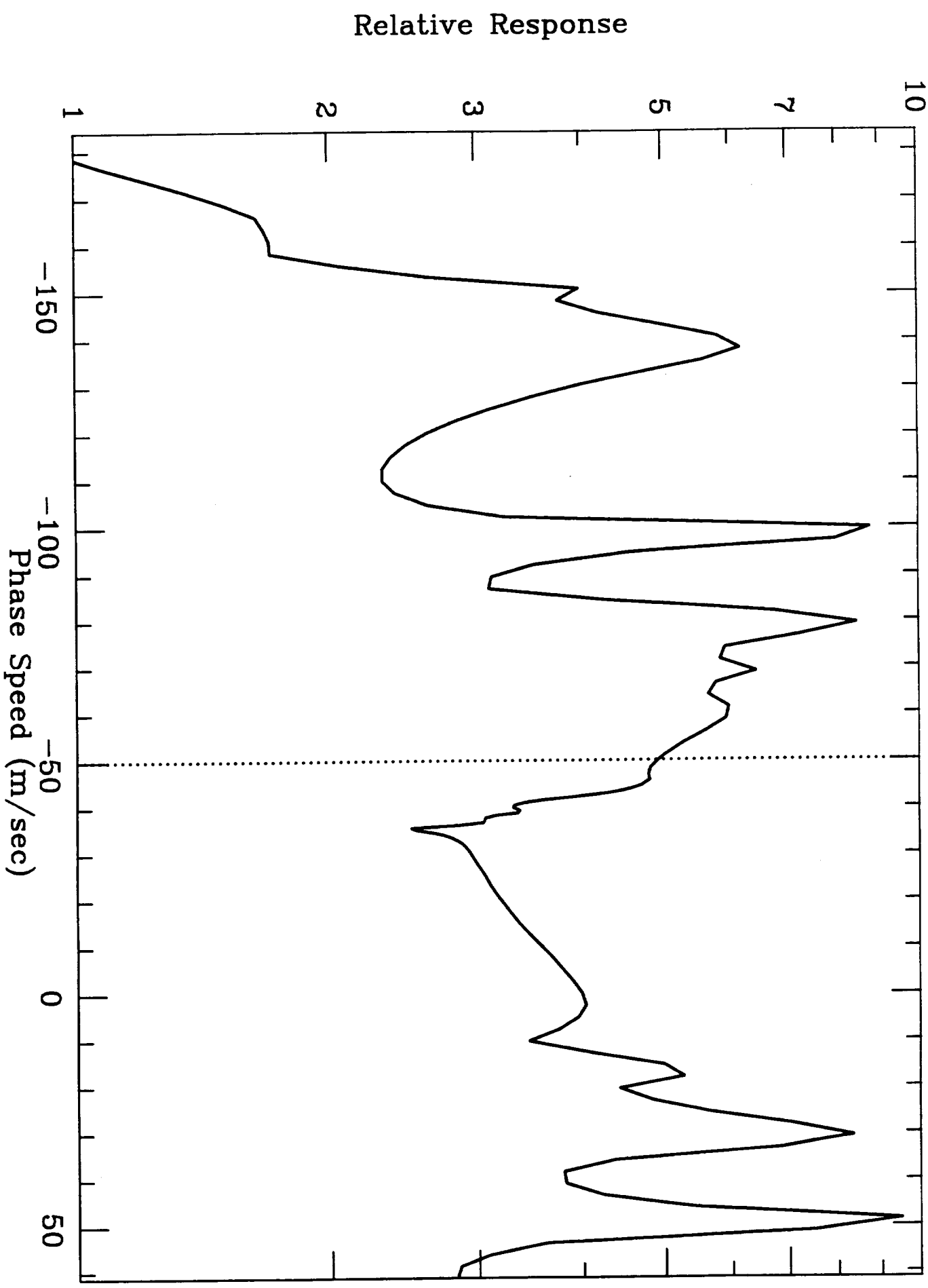

Fig. 10

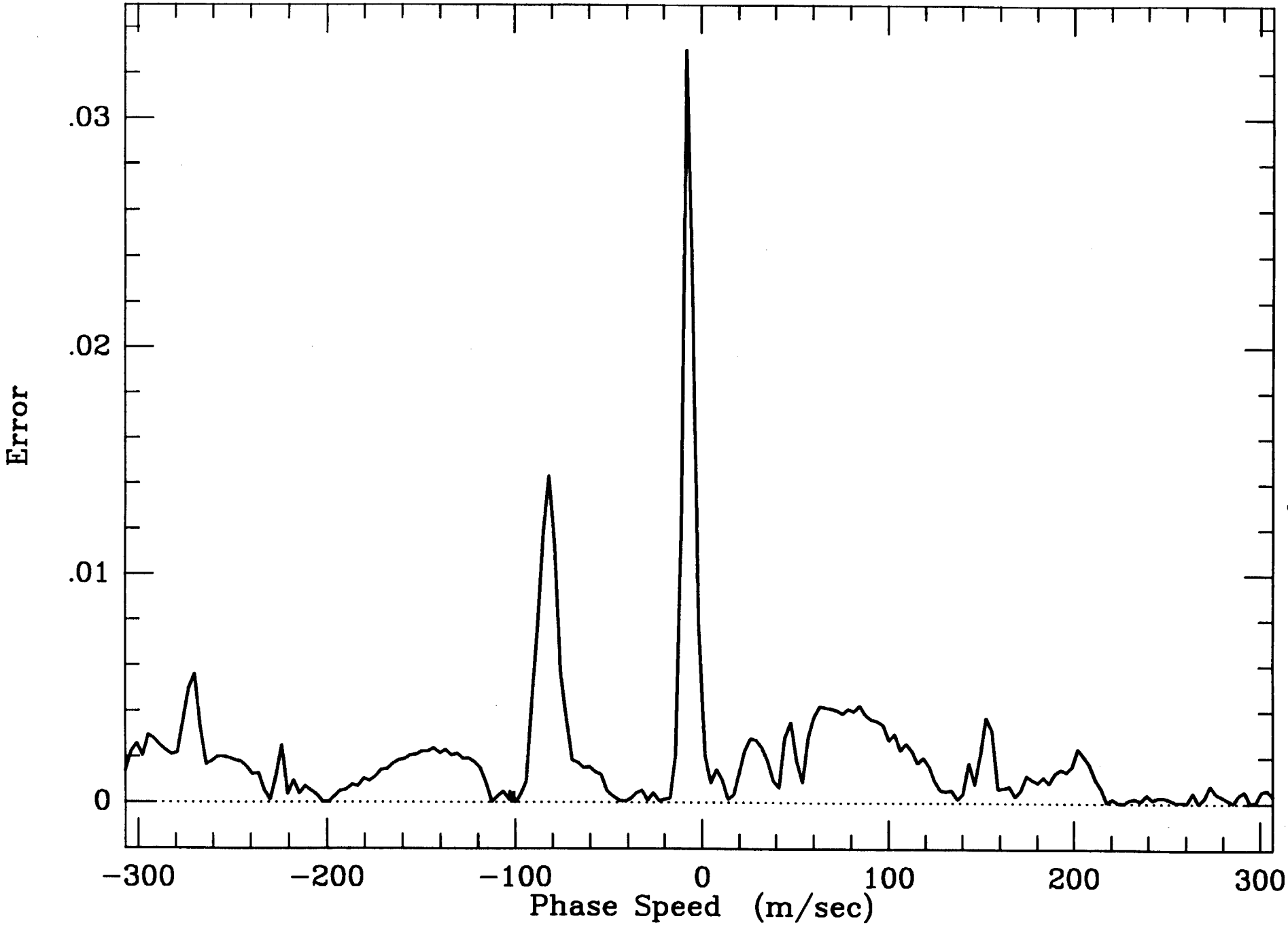

Fig. 11

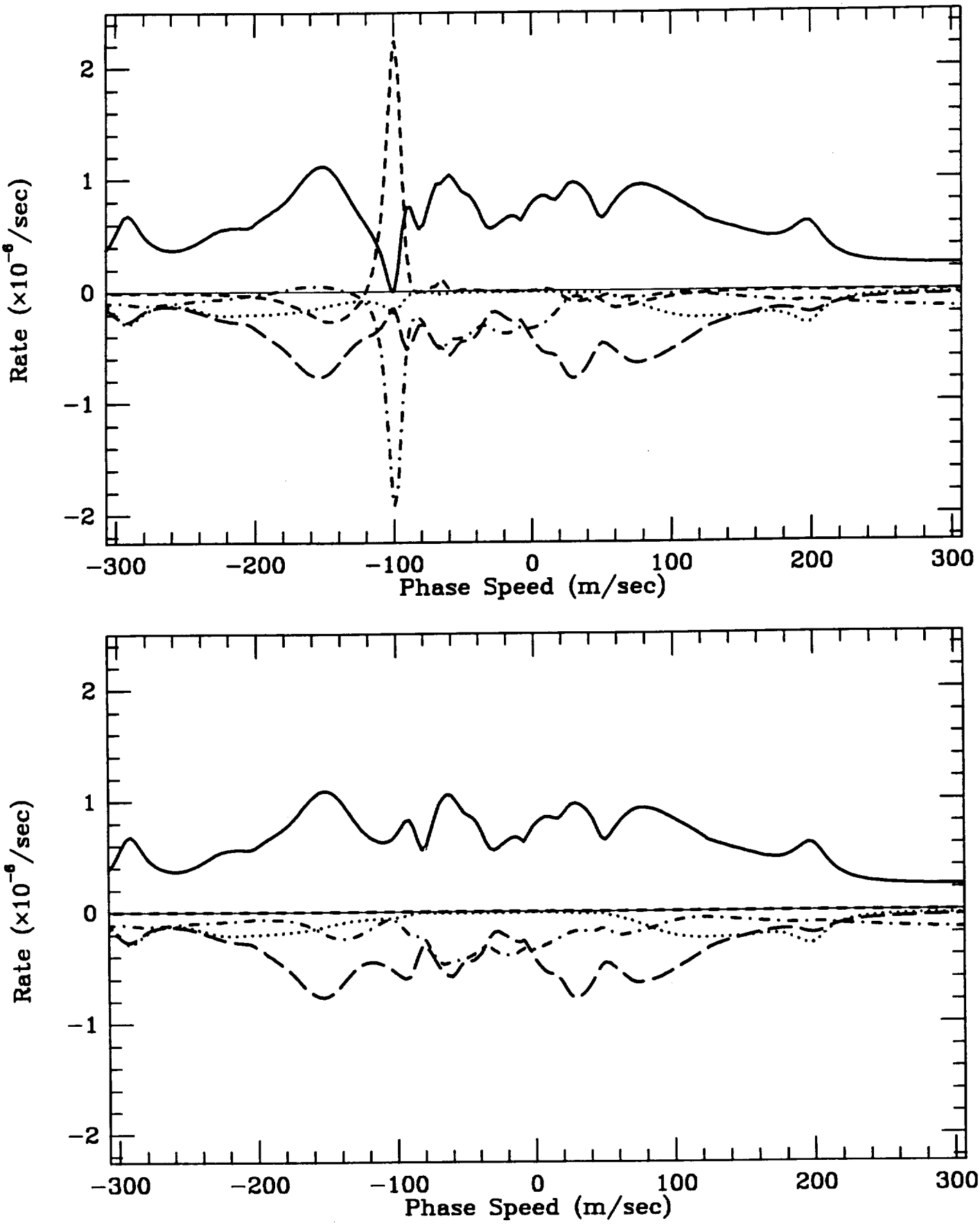
Rate (×10⁻⁶/sec)
2
1
0
−1
−2
−300
−200
−100
0
100
200
300
Phase Speed (m/sec)
Rate (×10⁻⁶/sec)
2
1
0
−1
−2
−300
−200
−100
0
100
200
300
Phase Speed (m/sec)

Fig. 12

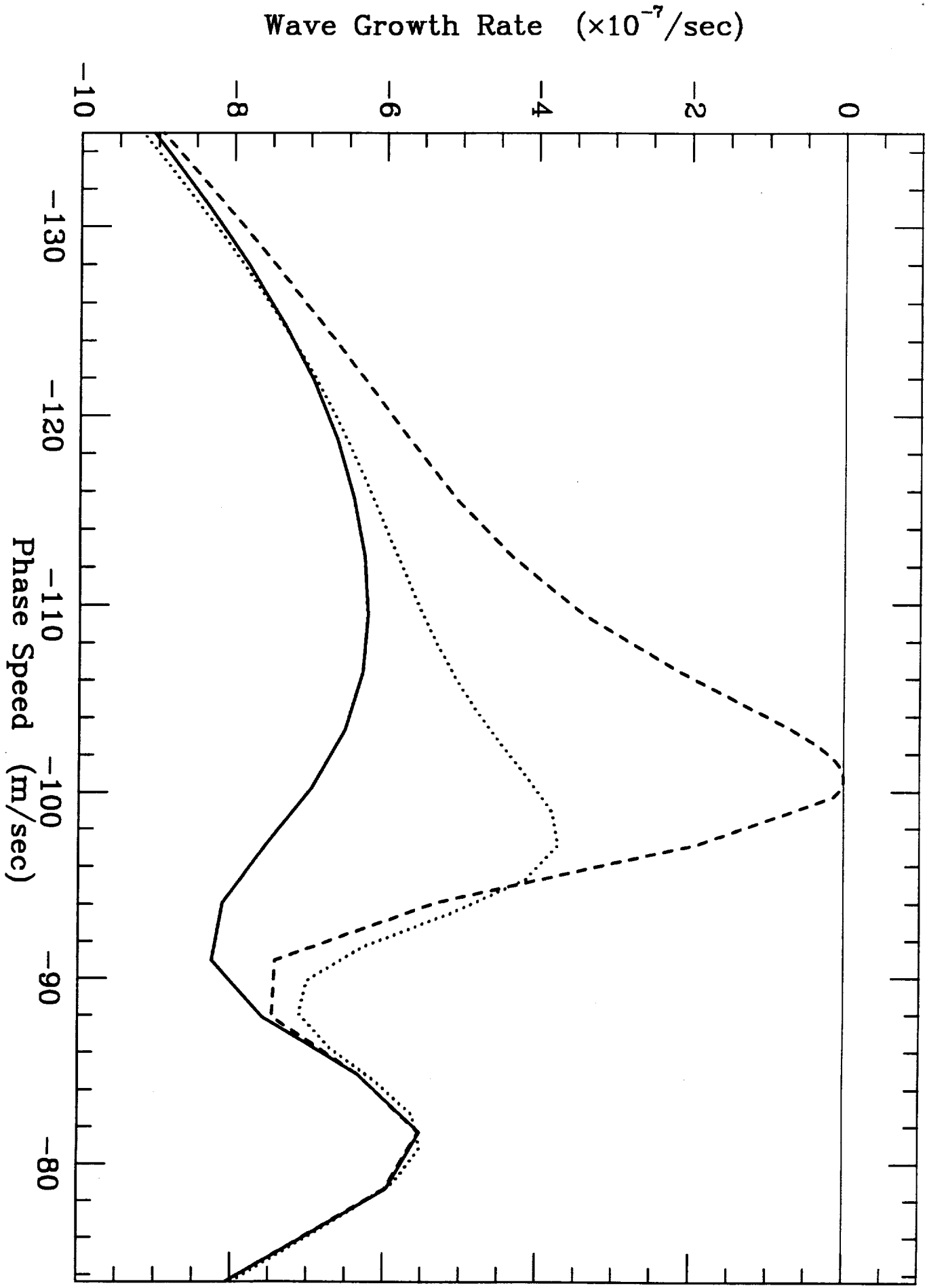
Wave Growth Rate (×10⁻⁷/sec)
−10
−8
−6
−4
−2
0
−130
−120
−110
−100
−90
−80
Phase Speed (m/sec)

Fig. 13

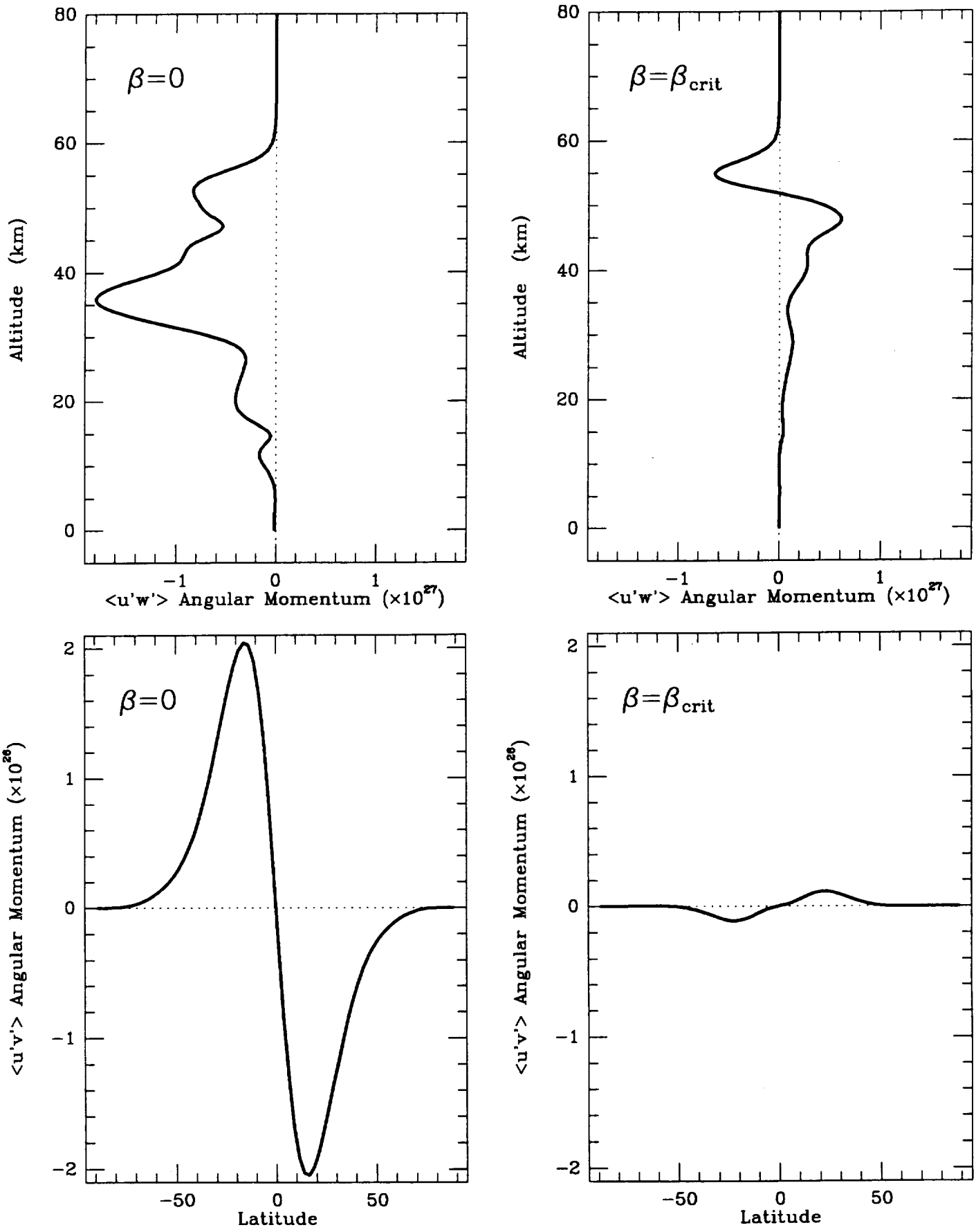
β=0
β=β crit
Altitude (km)
<u'w'> Angular Momentum (×10^27)
<u'v'> Angular Momentum (×10^26)
Latitude
80
60
40
20
0
2
1
0
−1
−2
−50
50

Fig. 14

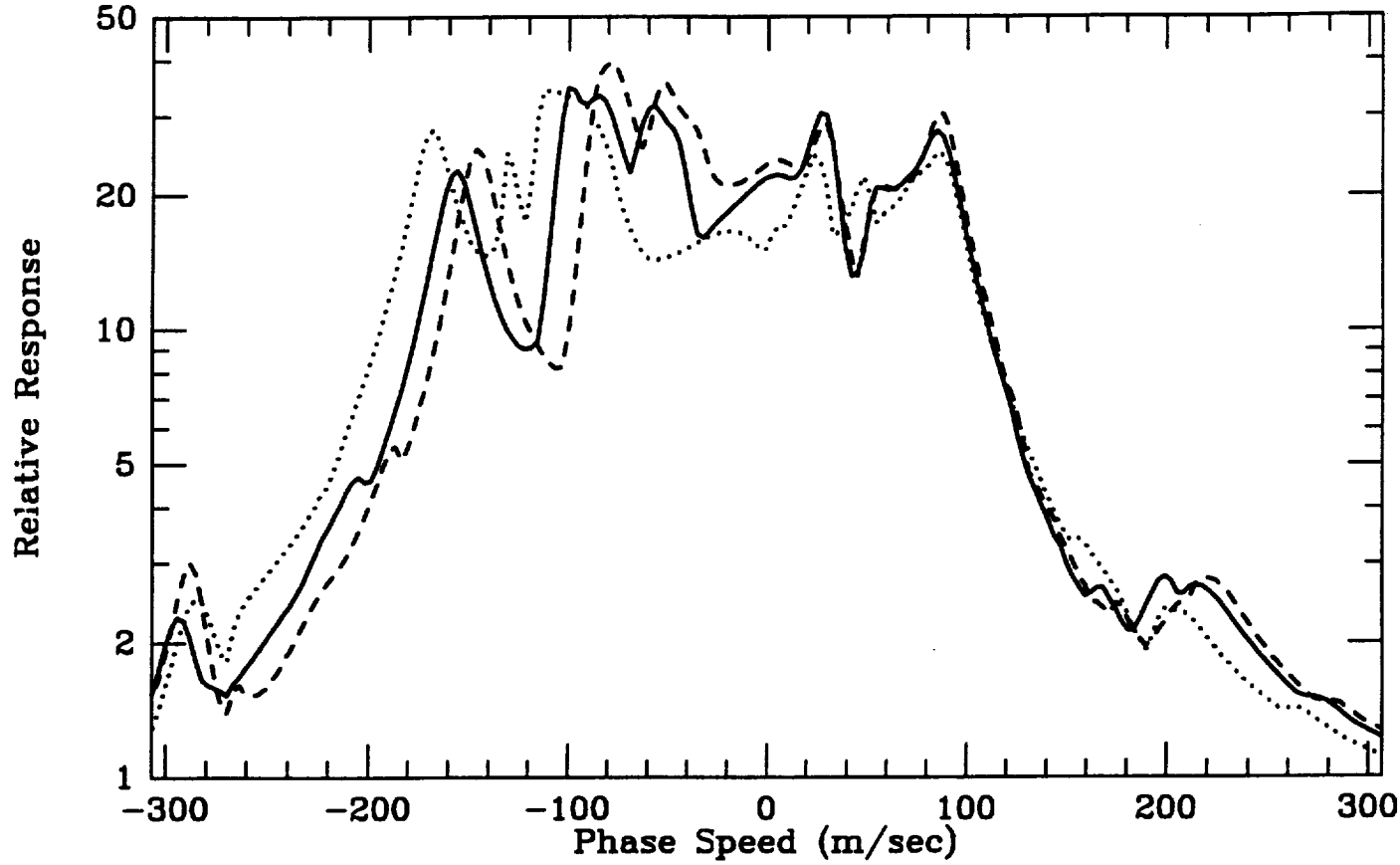
Relative Response
50
20
10
5
2
1
−300
−200
−100
0
100
200
300
Phase Speed (m/sec)

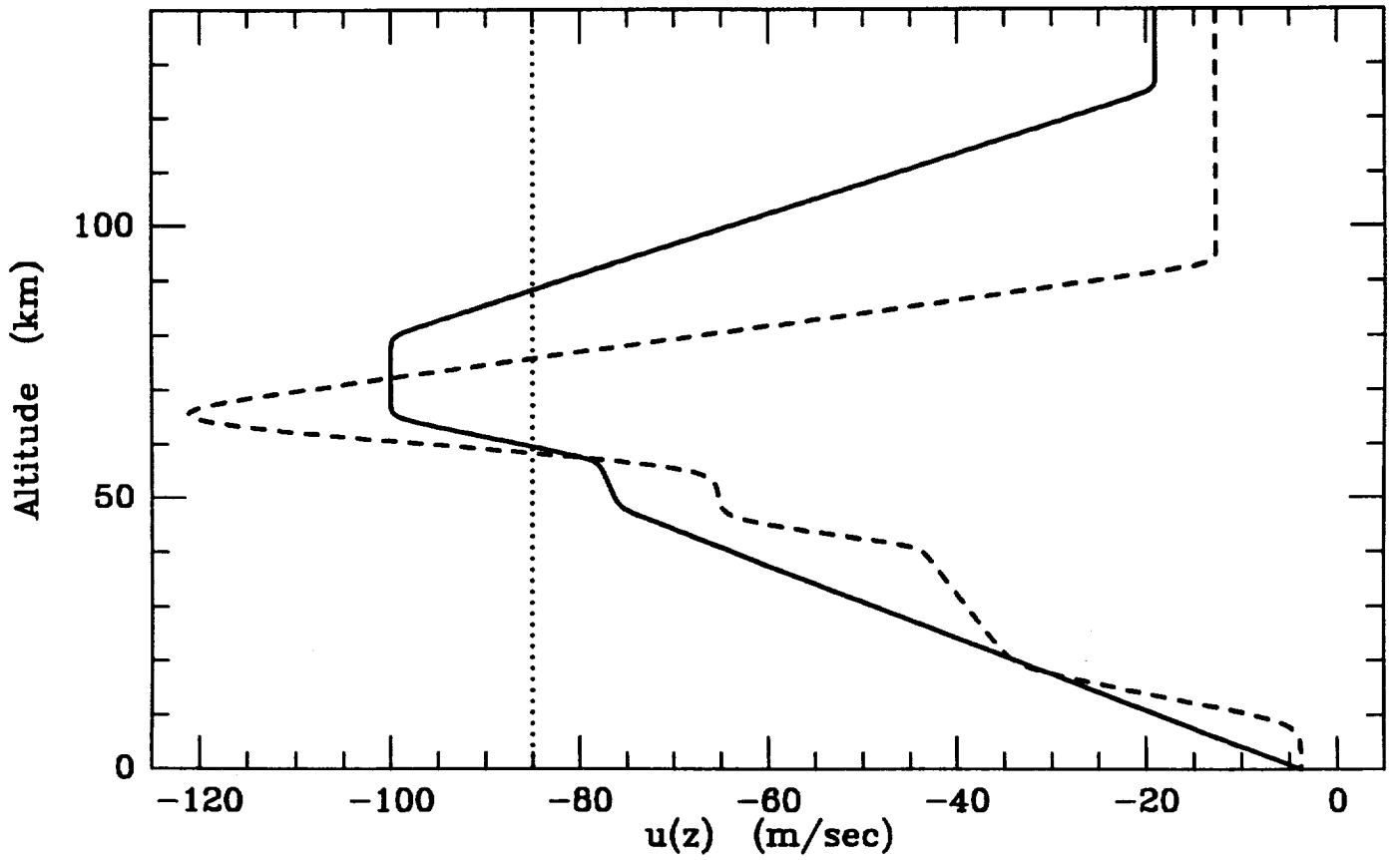
Altitude (km)
100
50
0
−120
−100
−80
−60
−40
−20
0
u(z) (m/sec)

Fig. 15

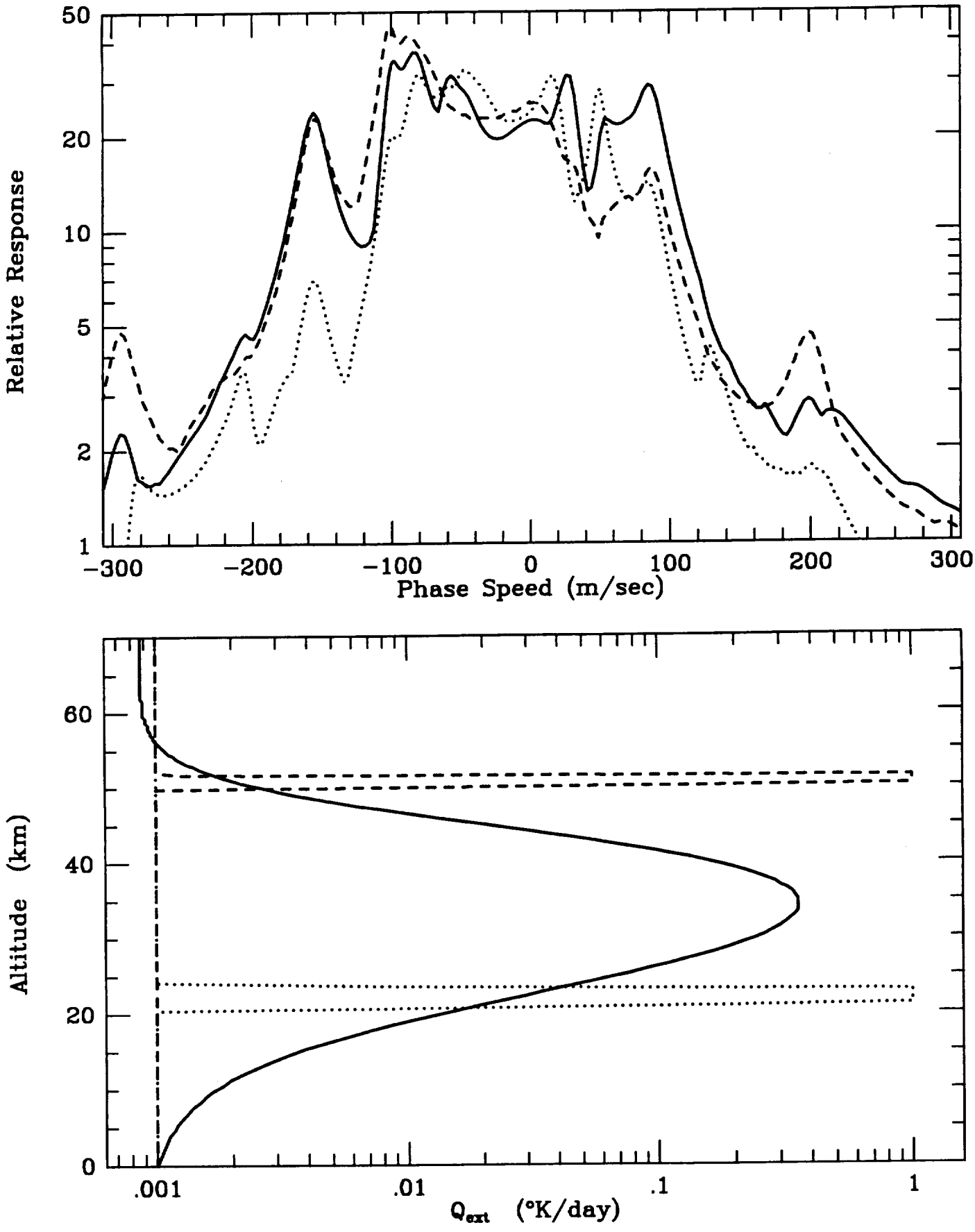
50
20
10
5
2
1
Relative Response
−300
−200
−100
0
100
200
300
Phase Speed (m/sec)
60
40
20
0
Altitude (km)
.001
.01
.1
1
Q_{ext} (°K/day)

Fig. 16

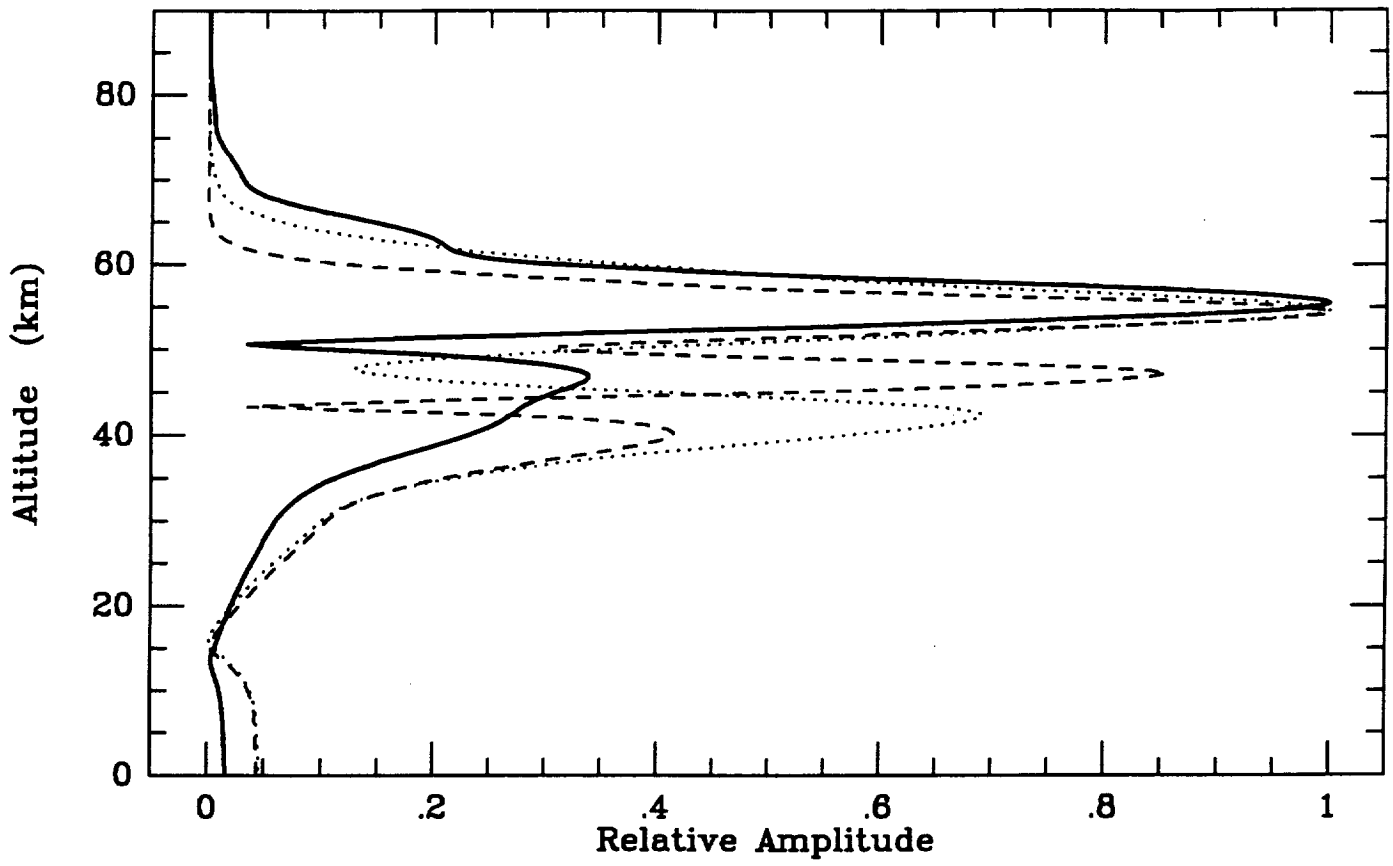
Altitude (km)
80
60
40
20
0
0
.2
.4
.6
.8
1
Relative Amplitude

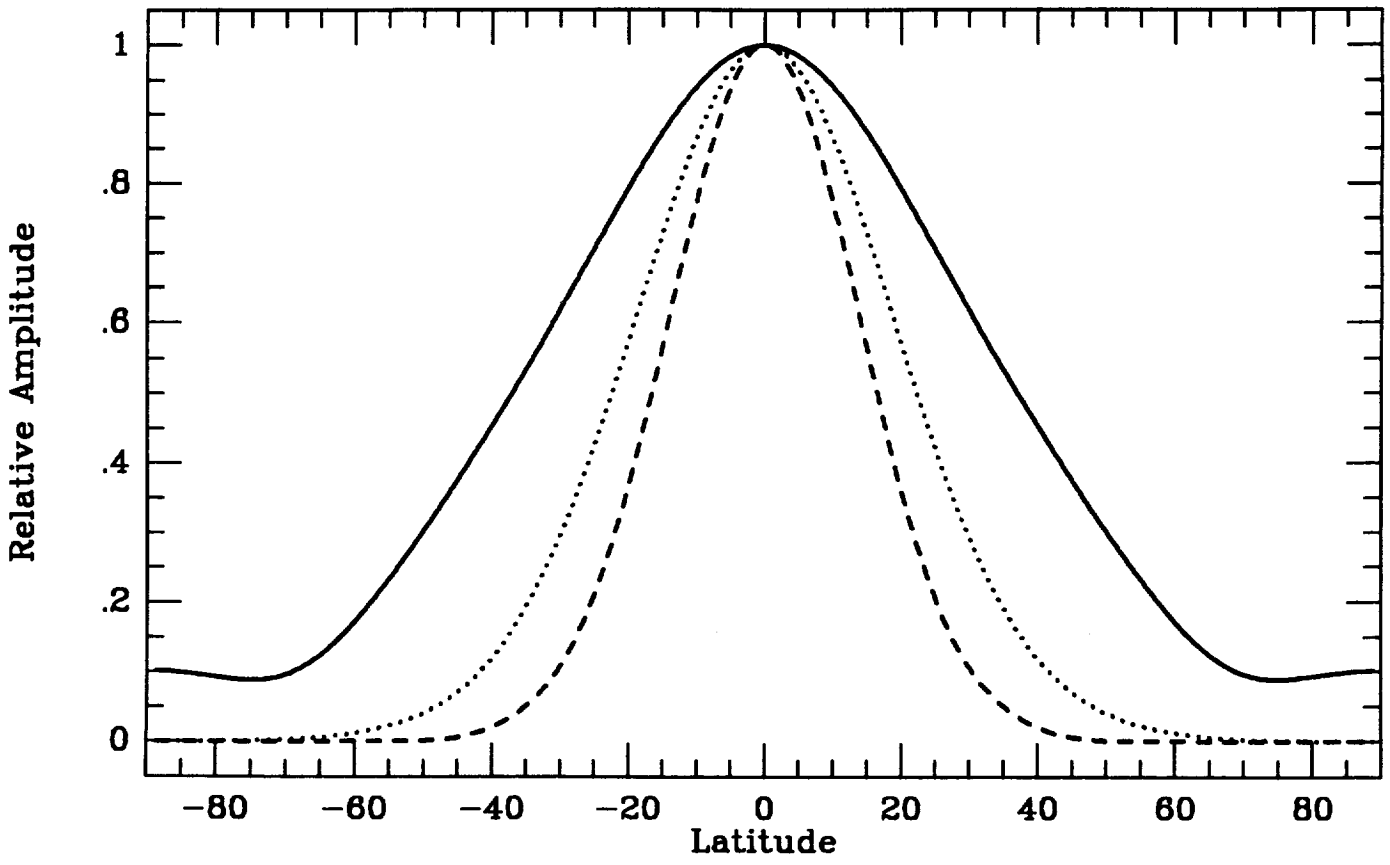
Relative Amplitude
1
.8
.6
.4
.2
0
−80
−60
−40
−20
0
20
40
60
80
Latitude

Fig. 17

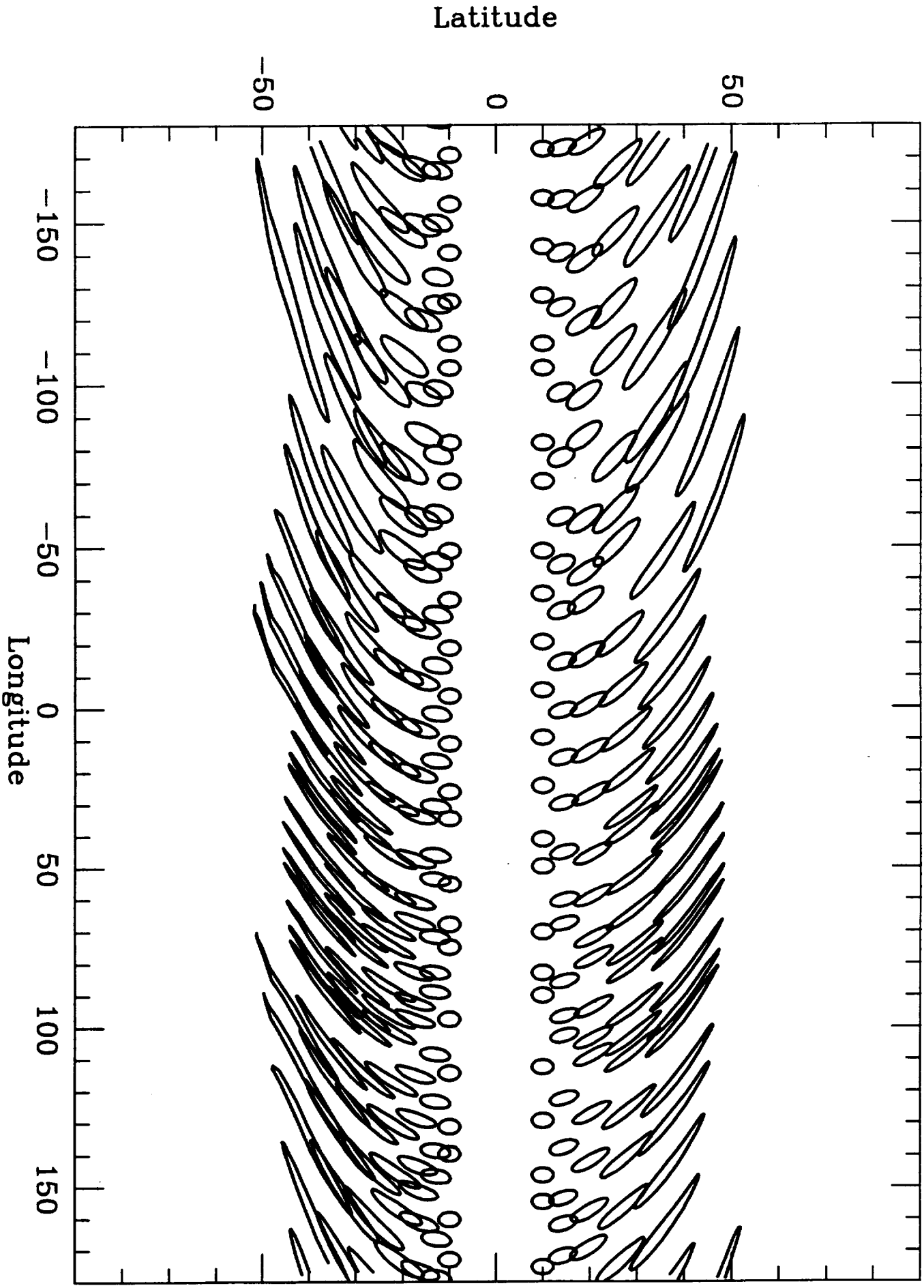

Fig. 1B

Fig. 19

High Resolution Cloud Feature Tracking on Venus by Galileo

Anthony Toigo
Division of Geological and Planetary Sciences
California Institute of Technology
Pasadena CA 91125

Peter J. Gierasch and Michael D. Smith
Astronomy Department, Space Sciences Building
Cornell University
Ithaca NY 14853

Submitted to *Icarus*

April 1993

22 pages

11 figures

0 tables

Proposed Running Head: "Venus Cloud Feature Tracking"

Index subjects: Atmospheres, Dynamics; Venus, Atmosphere

Please address editorial correspondence to:

Michael D. Smith
320 Space Sciences Bldg.
Cornell University
Ithaca, NY 14853

(607) 255-3933, FAX: (607) 255-9002
msmith@astrosun.tn.cornell.edu (Internet)

ABSTRACT

The Venus cloud deck was monitored for 32 hours at 400 nanometers wavelength by the Galileo imaging system, with a spatial resolution exceeding 15 km and with image time separations as small as 10 minutes. There is no evidence, to a level of approximately 4 m s^{-1}, of periodic or oscillatory wavelike activity at small scales. The dominant size of albedo features is 200-500 km, and their contrast is approximately 5%. At low latitudes the features are sometimes isotropic and blotchy and sometimes streaky. At high latitudes they are streaky. At low latitudes the contrast of blotchy features increases as they drift from the morning quadrant into the afternoon. There is no evidence, at the 4 m s^{-1} level, of eddy activity at scales intermediate between that of the blotches and of the planetary radius. It is speculated that the blotchy clouds are caused by a radiative-dynamical instability driven by differential absorption of sunlight by the clouds, that they are only about one half scale height deep, and that their horizontal scale is controlled by a deformation radius criterion.

1. INTRODUCTION

The Galileo spacecraft flew past Venus in February of 1990, and carried out a series of investigations of the atmosphere and environment of the planet. Preliminary reports are collected in a series of papers in *Science*, **253**, p. 1457-1612 (1991). An overview of the imaging experiment is given by Belton *et al.* (1991). Here we report on analysis of the high spatial resolution feature tracking observations made by the imaging system just after closest approach. Images were obtained over a period of 32 hours, with time sampling at a variety of intervals from 10 minutes to two hours. There is one gap of eight hours, between 16 and 24 hours after the sequence start, but otherwise there are images at least every two hours.

The objective of this experiment was to characterize the dynamics of the Venus cloud top as detected at near ultraviolet wavelengths (400 nanometers) at short time scales and with a spatial resolution of about 15 km. The Pioneer Venus orbiter collected extensive imaging data from 1979 through 1986 (see, for example, Rossow *et al.*, 1980) but these frames are separated in time by about four hours, and do not monitor the illuminated side of the planet continuously because of the 24 hour orbital period of the spacecraft. Mariner 10 flew past Venus along a trajectory quite similar to that of the Galileo spacecraft and collected a large number of images of high resolution and at time separations of about two hours (Belton *et al.*, 1974a), but the quality of many of these images is not high, and it is not possible to navigate them with precision for cloud motion determination.

In the next section we describe the data. Section 3 presents morphology and velocity results. Section 4 discusses interpretation.

2. GALILEO FEATURE TRACK IMAGING DATA

Image numbers 18217000 through 18399400 comprise the high resolution feature track. For the first 16 hours the images are two frame mosaics with the limb in the east frame, from which the camera pointing can be deduced. The west frame of the mosaic must be navigated against the east one by using cloud tracers. This procedure was iterated after determining velocities from the west frame by requiring that the average velocity agree with that of the entire time series.

The images were calibrated and blemishes removed with standard software provided by the Multi-mission Image Processing Laboratory at the NASA Jet Propulsion Laboratory. Limb darkening was removed by dividing by a photometric fit as described by Belton *et al.* (1991). The images were then partially high-pass filtered by subtracting a square box average of size about 10% of the planetary diameter. Finally, the images were projected onto a simple cylindrical map with 8 pixels per degree, which is sufficient to retain their resolution. One degree of latitude is about 107 km on the Venus surface. The images form 24 maps in final form.

3. MORPHOLOGY AND VELOCITIES

Figure 1 displays one of the high resolution mosaics. Note the two patches of mottled clouds separated by a less distinct zone with faint streaks. We have made a movie of the sequence of frames which shows the mottled clouds increasing in contrast as they drift across the disk from east to west. At higher latitudes small features can be seen to drift along the streaky lineations, moving poleward and from east to west. The movie shows no apparent large scale eddy activity, and no periodic or wavelike small scale activity. The edges of the mottled clouds change with time but not in any periodic or wavelike way. Thus the impression from the movie is that there are two dominant components of activity: a smooth large scale flow with the scale of the planetary radius, and mesoscale cloud mottling, with a typical scale of 200-500 km.

Figure 2 shows brightness scans through one of the stronger local maximum cloud features in the mottled pattern. The maximum is centered in the figure, with an amplitude of approximately 30 data numbers and a width of about 200 km. Its shape changes with time. An amplitude of 30 data numbers corresponds to a difference in the 400 nanometer

reflectivity of approximately 5%. The apparent noise level is about 10 data numbers. This is consistent with amplification of digitization noise by our contrast enhancement processing. To search for evidence of real albedo structure at scales smaller than 200 km, we computed the spatial autocorrelation function for a large number of brightness scans. A typical example is displayed in Fig. 3. The halfwidth of the autocorrelation is just under ten pixels (100 km) consistent with an absence of smaller-scale features.

a. The Automatic feature tracker

The measurement of cloud velocities was performed by a new automated cloud feature tracker algorithm. The automatic feature tracker first selects cloud features to match by finding areas of local maxima or minima of brightness in the reference image. Maxima and minima are searched for by placing a circular template of radius 1.25 degrees at a regular grid of points. The size of the template is chosen to be consistent with the size of typical cloud features. If the brightness (DN) values around the circumference of the template are all more than 3 DN less than the DN value at the center, then the center point is identified as a maximum. Minima are determined in a similar way. Figure 1 shows the minima and maxima found by the automatic feature tracker for a typical image. Cloud features are found throughout the image, although more are found in the mottled regions near the equator.

Each maximum and minimum is matched to a feature in a second image by finding the maximum 2-D cross-correlation coefficient as a function of horizontal offset between the two images. The correlation is performed using a 4 x 4 degree box. After the maximum correlation is found several checks are made to determine if it is a correct match. First, if the region around the feature being matched in the reference image does not have enough contrasting features in it, or if it is too close to the edge of the image, then the point is rejected. The threshold of minimum contrast used was that the standard deviation of brightness variation be at least 9 DN. Second, if the second highest cross-correlation coefficient is more than two degrees away from the maximum then the match is rejected. This eliminates matches caused by single pixel correlation peaks or by very noisy correlation coefficient behavior. Third, if the maximum correlation coefficient is less than 0.5, the match is rejected.

The matches are then checked for self consistency. A point 0.25 degrees away in line and sample from the original feature location is put through the same process described above. If a match is found, and is located near to the original match, then the feature is accepted. The maximum acceptable difference in position allows a change of 0.25 degrees (invariant with the time separation between frames) from the position of the original match.

To further insure the validity of the velocity vectors, the fastest 5% and the slowest 5% in zonal velocity are rejected. This kind of procedure can eliminate good vectors, but experience shows that the extreme 5% of vectors are often incorrect. Next, the remaining vectors are least-squares fit to a spherical harmonic expansion through Y_{22}. The 70% of the vectors closest to the fit are saved for a second least-squares fit to the spherical harmonic expansion. Any of the original vectors which are more than five standard deviations away from the second fit are rejected. All vectors that remain are saved and recorded.

A post-collection check was performed to verify the final data. The automatic feature tracker's results were compared to measurements made by a human operator. The correspondence is close. Several features picked by the automatic feature tracker were also tracked by a human. In almost every case (> 90 %), the human matched the same feature within five pixels (67 km) of the automatic feature tracker's match.

b. Results.

Using the automatic feature tracker, a total of 2588 vectors were obtained from 15 image pairs with time separations between 30 and 90 minutes. Of the 2588 vectors, 1255 came from cloud features that were local maxima and 1333 came from local minima. Figure 4 shows the averaged profile of all the local maxima cloud features and all the local minima cloud features. Local maxima and minima cloud features have the same average amplitude and similar profiles. Notice that on average a local maximum feature is surrounded by dark material and a local minimum cloud feature is surrounded by bright material at a distance of about 30 pixels (400 km).

Figure 5 shows contour plots of fits of the zonal and meridional wind velocities for both types of features together to the five lowest spherical harmonics ($Y_{00}, Y_{10}, Y_{11}, Y_{1-1}$, and Y_{20}). The results are consistent with earlier wind velocity profiles from this data set presented in Belton *et al.* (1991). In particular these results confirm a relatively flat zonal wind profile at about -100 m s^{-1} with weak mid-latitude jets during the Galileo encounter. Equatorial zonal wind velocities are slightly higher than those seen by Mariner 10 and Pioneer Venus. A divergence in the wind field centered just north of the equator in the early afternoon is observed. The meridional wind profile shows a poleward flow similar in magnitude to that seen by previous spacecraft.

To study the time dependence of the wind field the wind vector data were sorted in time. The list of wind vectors was searched to find features that had been identified in more that one image pair. Typically 60% of the features identified in one image pair were also identified in the next image pair. One feature was identified in ten consecutive image pairs,

but much more common are features that were identified in two, three, or four consecutive pairs. Figure 6 shows the paths of cloud features identified in three or more consecutive image pairs. The symbols mark the location of the feature in the earlier of the two images of each image pair. The general westward and poleward movement is immediately evident. When a large-scale average is removed, the lack of large eddies in the flow becomes apparent. Figure 7a shows the same cloud feature tracks for the local maxima cloud features with the spherical harmonic wind velocity fit shown in Fig. 5 removed. Figure 7b shows a small region from within Fig.7a, expanded to show displacements. These are consistent with one or two pixel locational uncertainties, and are probably caused by noise. The velocity corresponding to a one pixel displacement over a time difference of one hour is about 4 m s^{-1}, and this is the level to which we can state that there is no organized large-scale eddy activity.

Figure 8 shows the correlation between corresponding small regions as a function of time difference between the two images in an image pair for a number of cloud features. In all cases there is an initial relatively large drop in the correlation coefficient followed by a more gradual decrease. The initial drop is caused by digitization error while the gradual decrease is caused by deformation or by chemical, albedo, or other cloud property change. An estimate for the time scale, t_r, is given by

$$t_r = \left(\frac{\partial r}{\partial t}\right)^{-1},$$

where r is the correlation coefficient. Calculating a slope with the data from Fig. 8 we estimate t_r = 50 hours. This is consistent with the observation that well-defined small cloud features can sometimes be followed from limb to limb (two days of rotation), but are never seen to reappear on the next rotation another two days later.

The initial drop in the correlation coefficient is caused by digitization error. For any pair of non-identical images the correlation coefficient between corresponding regions is less than unity. As the time separation between images in an image pair approaches zero the effect of real physical change vanishes and the remaining difference from unity in the correlation coefficient is caused by other processes. In two non-identical images, the scene is sampled slightly differently because the camera pointing is different. This introduces a ± 1 DN digitization error, even for very short time separations. This error is magnified by the processing that occurs during our contrast enhancement and accounts for the drop in the correlation coefficient.

4. DISCUSSION AND INTERPRETATION

The general features of the velocity field are as follows. The large scale pattern is smooth and can be closely represented by only a few harmonics. It shows a poleward wind maximum just to the west of the noon meridian at midlatitudes, and a westward wind minimum near noon. There is a remarkable absence of eddy activity at intermediate scales between the planetary radius and 1000 km. In this particular data set, the dominant small-scale phenomena visible in ultraviolet images of Venus are 400 to 1000 km in wavelength, and therefore have gradients concentrated on spatial scales of about 200 to 500 km. They have a time scale for deformation, appearance or disappearance of about two days. They vary in morphology from quite isotropic blotches with contrast of about 5%, which occur in patches at low latitudes, to striated formations whose contrast is a bit less. The blotches and striations at low latitudes seem to spontaneously generate and amplify. There is indication from Pioneer Venus monitoring (Rossow *et al.*., 1980) that these blotches regularly appear at morning longitudes and amplify during passage through the afternoon. The striations at high latitudes do not amplify, but appear to be caused by shearing deformation of pre-existing blotches (Schinder *et al.*, 1990). Finally, the images do not show any evidence of high frequency spatial or temporal periodicities that would be evidence for internal gravity waves.

The next few paragraphs discuss several features of the data.

a. The large scale velocity field.

The large scale velocity field displayed in Fig. 5 is consistent with measurements from Pioneer Venus images and Mariner 10 images (Del Genio and Rossow,1990; Limaye,1987). The Galileo images contain no surprises but confirm that the pattern was unchanged in February of 1990. The velocity pattern is nicely consistent with predictions of the flow produced by the solar-fixed atmospheric tides, plus the mean flow associated with a Hadley circulation as modified by tidal transports of momentum (Newman and Leovy, 1992).

b. Shear

The lifetime of features puts an upper limit on the magnitude of the shear in the flow. Shear leads to a relative displacement, either horizontally from one side of a feature to the other, or vertically from the top to the bottom. The shear at most produces a relative

displacement across the feature in the time t_r that is equal to the feature size. In the case of horizontal shear,

$$|\nabla \mathbf{u}| \approx \frac{\text{relative displacement rate}}{\text{horizontal separation}} = \frac{L/t_r}{L} \leq \frac{1}{t_r} = \frac{1}{50\ \text{h}} \sim 0.5\ \text{m s}^{-1}\ (100\ \text{km})^{-1}.$$

In the case of vertical shear,

$$\frac{\partial \mathbf{u}}{\partial z} \approx \frac{\text{relative displacement rate}}{\text{vertical separation}} = \frac{L/t_r}{D} \leq \frac{L}{D}\frac{1}{t_r} \sim 0.5\ \text{m s}^{-1}\ \ \text{km}^{-1},$$

where we used $L = 200$ km and conservatively used a shallow depth, $D = 2$ km. The average vertical shear in the Venus atmosphere is about 100 m s^{-1} over a height of 70 km, or 1.4 m s^{-1} km^{-1}. The long lifetime of the blotchy features suggests that they reside where the vertical shear is smaller than average, probably near the zonal wind maximum.

c. The convection hypothesis

It was suggested by Belton *et al.* (1976) and again recently by Baker and Schubert (1992) that the low latitude blotches are caused by convection. The Venus atmosphere is stably stratified near the 70 km (40 mb) level (Seiff *et al.*, 1980; Seiff, 1987) where ultraviolet contrasts are formed (Kawabata *et al.*, 1980). The convection is proposed to be penetration of motion from deeper levels. The thermal structure deduced by Seiff *et al.* and by Venera probes (Avduevskiy *et al.*, 1983) shows two layers where the vertical temperature gradient is possibly very close to the adiabatic: a zone about one scale height thick where the thickest clouds are located (49 to 56 km elevation) and a zone near the planetary surface, also perhaps a scale height thick (15 km). The latter one is in more doubt because measurement errors are uncertain (Avduevskiy *et al.*, 1983).

The Galileo feature track data can neither confirm nor deny the convection hypothesis because the velocity information is restricted to the 70 km level. Several remarks can be made, however. (i) The dominant length scale in the data is a few hundred kilometers, which seems a bit large to originate from convection even in the deeper layer 15 km thick. Baker and Schubert discuss this point and argue that it is possible. (ii) The traditional free convection time scale estimate,

$$t \approx \left(\frac{\gamma}{\gamma - 1} \frac{pD^2}{gF} \right)^{1/3},$$

where D is the layer depth, F is the convective heat flux, γ is the ratio of specific heats, g is the acceleration of gravity and p is pressure can be compared with the approximately two day time scale for variation of the Venus blotches. Using a heat flux of $F = 20$ W m^{-2} and the local scale height for D gives $t \sim 1$ hour for the cloud layer and about half a day for the deeper layer near the surface. The latter is therefore consistent with the observations. (iii) The observed blotches drift with the cloud top wind speed and intensify while they drift. If they are part of a deep cell anchored in the bottom scale height of the atmosphere, they will shear half way around the planet during their lifetime of two days. This seems unlikely. Alternatively, they could be the manifestation of a sudden disturbance forced from below, which then merely drifts with the upper level winds. But if this is the case, why should their contrasts continue to intensify for periods of a day or more?

To confirm or deny the convection hypothesis will require data from beneath the cloud top level, simultaneously with ultraviolet monitoring of the top.

d. Local radiative forcing

Why does a horizontal scale of about 300 km appear in ultraviolet albedo features in the Venus cloud deck? The physical or chemical processes that alter cloud albedo are not known, but dynamical constraints on time scales and length scales can be examined. Here we shall assume that albedo or opacity contrasts lead to horizontal variations in radiative heating. The strength of a dynamical response is evaluated for different assumptions about the horizontal and vertical scales of the radiative forcing, to see under what conditions a scale of 300 km can emerge strongly. Surprisingly, the results show that the only consistent scaling is for albedo features only about 2 km thick.

(i) Physical conditions near the visible cloud top

Crisp (1986) discusses the absorption of sunlight in the Venus atmosphere. Near the cloud tops there were no direct measurements of solar fluxes or cloud particle properties by the Pioneer probes, and heating rates must be derived by radiative modeling, constrained by the flux and particle measurements at greater depth and by remote measurements of reflectivity and polarization. It is known that the ultraviolet contrasts in the Venus clouds

originate at a level deeper than optical depth unity at 365 nm wavelength, because the contrast decreases with increasing phase angle (Esposito, 1980; Pollack et al., 1980). Polarimetry can be used to identify the gas pressure at unit optical depth (Kawabata et al., 1980). It is about 28 mb and the elevation is about 71 km. On the other hand the measured solar fluxes from the Pioneer probe show that no significant ultraviolet absorption occurs at depths greater than about 320 mb, or 58 km elevation (Tomasko et al., 1985). Thus the absorption is located between about 58 km and 71 km elevation. Approximately half of the total solar flux absorption occurs in this layer. Of this absorption, Crisp shows that roughly half is due to the gases H_2O and SO_2, and the remainder is by an unknown constituent, probably a contaminant of the sulfuric acid droplets that make up the cloud.

The horizontal variability of the absorption is of particular interest for dynamics. SO_2 is variable over the disk on Venus and its occurrence correlates well with dark ultraviolet areas, but Esposito (1980) shows that the spectral dependence of the ultraviolet contrasts is not consistent with a cause purely in terms of SO_2 absorption. Esposito and Travis (1982) work with radiative transfer models in which they vary the cloud single scattering albedo and vertical distributions. They use Pioneer Venus polarimetry to constrain the modeling. They find consistent cloud models in which the variable ultraviolet absorption is due only to variations in cloud particle properties. The single scattering albedo and the cloud top height are both lower in dark regions. The level where the 365 nm optical depth is unity is about 29 mb in bright regions and 37 mb in dark regions, corresponding to elevations of about 70 km and 69 km. They also find the interesting and puzzling result that in order to explain the polarization the overlying submicron haze must also vary between dark and light regions. There is very little energy absorption in this haze but it affects the polarization. It is located above the main cloud deck, near a pressure of 5 mb and a height of 79 km. Esposito and Travis find that its optical depth is larger (0.025 at 270 nm compared to 0.014) over dark regions, and its height is about 2 km lower over dark regions.

Crisp examines the heating rate variations that are implied by these different cloud distributions. The variations are located near the 70 mb (approximately 66 km) level in the atmosphere, slightly deeper than the 365 nm optical depth unity level. The global mean solar heating shows a local maximum here due to the ultraviolet absorption. Figure 9 displays heating rate profiles from Crisp (1986). The difference between light and dark regions is about 2 K per day and extends over a height range of about one scale height, or 5 km, centered near 66 km. This global average difference in heating rate corresponds to about 8 K per day near the subsolar point. Crisp also shows a different heating rate profile, also consistent with the observational constraints, with a lower top to the ultraviolet absorbers and

a narrower width to their distribution. In this case the peak amplitude of the heating variations is about twice as large.

Crisp (1989) examines the influence of different distributions of the ultraviolet absorber on the mean radiative equilibrium temperature profile. He shows that the temperature gradient is affected by the peak in the heating rate near 66 km, and finds that in the extreme case of a low cloud top with a narrow heating distribution a thin convectively unstable layer is predicted between 64 and 65 km elevation. Unfortunately the vertical resolution of probe temperature measurements is probably not sufficient to test this prediction (see for example, Seiff, 1987). Crisp also evaluates the radiative damping rate near these levels and finds it to be about two days for a thermal disturbance of vertical wavelength 7 km. In this regime the damping rate should be approximately linear in the vertical scale (Goody and Yung, 1990).

In summary, the differential solar absorption between ultraviolet dark and light regions is on the order of 8 K per day near the subsolar point and peaks near a height of about 66 km. It is probably about a scale height in depth. It may be located a bit deeper in the atmosphere and if so, it is less vertically extended and of higher amplitude. The dark and light regions discussed above are large scale features, and heating variations associated with blotches and wisps of scale 200-500 km are probably smaller, and may also be more localized in height. The mean temperature profile may have a relatively large gradient near and just above the peak in the ultraviolet absorption, which would produce a layer of relatively small stratification. Finally, the radiative time constant for disturbances of vertical wavelength 7 km is about two days, and it is approximately proportional to the vertical scale.

(ii) Dynamical investigations - motivation

Because the nature of the ultraviolet absorber is unknown, it is not known how it is influenced by motions. Analysis of large scale waves in the Venus atmosphere suggests that regions of upward motion are dark (Del Genio and Rossow, 1990; Smith et al., 1993). For the small scale motions of interest here, there is no well founded observational or theoretical basis for predicting the influence of velocities on albedo. The possibilities are diverse. Motions could influence absorption by advection of either particles or gas. There might be time lags introduced by chemical or photochemical rates. In the absence of fundamental physical or chemical understanding a purely dynamical investigation may be useful. In the following discussion it will be assumed that horizontal variations of radiative heating are imposed, and the nature of the atmosphere's dynamical response will be addressed. The horizontal and vertical scales of the radiative forcing will be treated as parameters, and the

amplitude and structure of the dynamical response will be examined to determine if there is a dynamical reason to favor certain special scales.

The first investigation is a steady, nonlinear scaling analysis of a simple dynamical model in order to determine the fundamental regime. In the second investigation a linearized model is introduced to study the initial response of the system.

(iii) Nonlinear analysis

Assume steady flow forced by horizontal variations in radiative heating. Anticipate that the aspect ratio of the flow is small so that the hydrostatic approximation is valid. Assume that the circulation is shallow relative to a density scale height so that the Boussinesq approximation is valid. The governing equations can be written

$$wv_z + vv_y + \frac{1}{\rho_0} p_y = 0, \tag{1}$$

$$\frac{1}{\rho_0} p_z = g\frac{T'}{T_0}, \tag{2}$$

$$v_y + w_z = 0, \tag{3}$$

$$vT'_y + wT'_z = \frac{T'_E - T'}{t_R}. \tag{4}$$

Temperature, pressure and density are written as constants plus small perturbations, for example $T = T_0 + T'$. Radiative heating is parameterized by a radiative equilibrium distribution T'_E and a radiative time constant t_R. The specification of the model is completed by assuming a rectangular geometry with impermeable walls separated in the horizontal by $2L$ and in height by $2D$.

The radiative equilibrium distribution T'_E is characterized by a vertical contrast in the stable sense given by ΔT_{EV} and a horizontal contrast ΔT_{EH}. Let the unknown contrasts of the temperature itself be ΔT_H and ΔT_V. The amplitude of horizontal and vertical velocities are V and W. Horizontal and vertical length scales are L and D.The continuity equation (Eq. 3) and the force balances (Eqs. 1 and 2) give the scaling relations

$$\frac{V}{L} = \frac{W}{D}, \tag{5}$$

$$V^2 = gD\frac{\Delta T_H}{T_0}. \tag{6}$$

Rewrite the advective portion of the heat equation (Eq. 4) in flux form and integrate it first over the top half of the fluid volume, and then over the bottom half. Assume no flow out of the bounding container and subtract the two integrals. A statement is thereby derived relating the vertical difference in the radiative heating to the vertical heat flux by motions. Repeat the steps for the left and right halves of the domain to derive a statement about the horizontal heat flux. In scaled form the results are

$$-\frac{W\Delta T_H}{D} = \frac{\Delta T_{EV} - \Delta T_V}{t_R}, \tag{7}$$

$$\frac{V\Delta T_V}{L} = \frac{\Delta T_{EH} - \Delta T_H}{t_R}. \tag{8}$$

In writing Eqs. 7 and 8 the signs of all the scaling amplitudes are taken to be positive, and an assumption is made that the correlation between W and ΔT_H is thermodynamically direct. Subject to this assumption, the signs in Eqs. 5-8 are all meaningful, so the statements are slightly more than amplitude scalings.

Equations 5-8 are four equations for the four unknown amplitudes $V, W, \Delta T_H, \Delta T_V$. They can be reduced to one equation for the horizontal velocity. Let

$$V_0^2 = gD\frac{\Delta T_{EH}}{T_0}. \tag{9}$$

Eqs. 5-8 give

$$\left(\frac{V_0 t_R}{L}\right)^2\left(\frac{V}{V_0}\right)^4 + \left(\frac{V}{V_0}\right)^2 + \frac{V_0 t_R}{L}\frac{\Delta T_{EV}}{\Delta T_{EH}}\frac{V}{V_0} = 1. \tag{10}$$

There are three physically different solution regimes depending on which of the terms on the left hand side balances the one on the right., which originated from the ΔT_H term in Eq. 8 and is assumed to be the fundamental drive. After solving for the velocity, temperature contrasts can be evaluated from

$$\Delta T_H = \frac{V^2}{gD} T_0 \tag{11}$$

$$\Delta T_V = \Delta T_{EV} + \frac{V t_R}{L} \Delta T_H \tag{12}$$

The location of the solution regimes in parameter space is indicated in Fig. 10. The two parameters are $V_0 t_R / L$ and $\Delta T_{EV} / \Delta T_{EH}$. The regimes are labeled according to a qualitative description of the nature of the dynamics.

1) Radiative regime. Radiation controls the thermal structure when

$$\frac{V_0 t_R}{L} << 1, \quad \frac{V_0 t_R}{L} \frac{\Delta T_{EV}}{\Delta T_{EH}} << 1. \tag{13}$$

Solutions are given by

$$\begin{aligned} V &= V_0, \\ \Delta T_H &= \Delta T_{EH}, \\ \Delta T_V &= \Delta T_{EV} + \frac{V_0 t_R}{L} \Delta T_{EH}. \end{aligned} \tag{14}$$

Notice that this regime is really divided into two, since the vertical temperature gradient can be altered by dynamics if ΔT_{EH} is large enough.

2) Stratified regime. The vertical thermal structure is controlled by radiation while horizontal contrasts are controlled by dynamics when

$$\frac{V_0 t_R}{L} \frac{\Delta T_{EV}}{\Delta T_{EH}} >> 1, \quad \frac{V_0 t_R}{L} \left(\frac{\Delta T_{EV}}{\Delta T_{EH}} \right)^2 >> 1. \tag{15}$$

Solutions are given by

$$\begin{aligned} V &= \frac{L}{t_R} \frac{\Delta T_{EH}}{\Delta T_{EV}}, \\ \Delta T_H &= \left(\frac{L}{V_0 t_R} \right)^2 \left(\frac{\Delta T_{EH}}{\Delta T_{EV}} \right)^2 \Delta T_{EH}, \\ \Delta T_V &= \Delta T_{EV}. \end{aligned} \tag{16}$$

3) Convective regime. Thermal contrasts in both directions are dynamically determined. The conditions for this regime are

$$\frac{V_0 t_R}{L} >> 1, \quad \frac{V_0 t_R}{L}\left(\frac{\Delta T_{EV}}{\Delta T_{EH}}\right)^2 << 1. \tag{17}$$

Solutions are given by

$$\begin{aligned} V &= \sqrt{V_0}\sqrt{\frac{L}{t_R}}, \\ \Delta T_H &= \frac{L}{V_0 t_R}\Delta T_{EH}, \\ \Delta T_V &= \sqrt{\frac{L}{V_0 t_R}}\Delta T_{EH}. \end{aligned} \tag{18}$$

Knowledge of the physical state of the Venus system fixes most of the parameters of this interpretive model to within a factor of two or so. The vertical scale D is not well defined. The questions one can ask are: Is there a reason for a particular horizontal scale L to dominate even if the forcing does not select one? What is the depth of the flow regime that emerges from a consistent scaling and agrees with our physical knowledge?

As a first step, estimates of all parameters can be made in order to determine the general area of interest in the regime diagram. Based on the discussion above, estimates are

$$\begin{aligned} \Delta T_{EH} &= 4\ \mathrm{K}, \\ \Delta T_{EV} &= 20\ \mathrm{K}\left(\frac{D}{D_0}\right), \\ T_0 &= 230\ \mathrm{K}, \\ D_0 &= 5\ \mathrm{km}, \\ L &= 300\ \mathrm{km}, \\ t_R &= 2\ \mathrm{d}\left(\frac{D}{D_0}\right), \\ g &= 8.8\ \mathrm{m\ s^{-2}}. \end{aligned} \tag{19}$$

The reference vertical scale D_0 is a scale height. It is assumed that the radiative forcing tends to drive the system to a vertical gradient which is less steep than the adiabatic by 20 K per

scale height, and it is assumed that the radiative time constant is proportional to the vertical scale. The depth D cannot be precisely identified with any layer in the atmosphere. It would probably correspond to about half the depth of a hypothetical vertical cell since it is a scale for estimating gradients. These estimates give the numerical parameter values:

$$V_0 = 28 \text{ m s}^{-1} \sqrt{\frac{D}{D_0}},$$

$$\frac{V_0 t_R}{L} = 16 \left(\frac{D}{D_0}\right)^{3/2}, \tag{20}$$

$$\frac{\Delta T_{EV}}{\Delta T_{EH}} = 5 \left(\frac{D}{D_0}\right).$$

If $D = D_0$ this places the parameters in the stratified regime. The solution for the velocity using Eq. 16 gives

$$V = 0.35 \text{ m s}^{-1} \left(\frac{D_0}{D}\right)^2. \tag{21}$$

This estimate, based on a depth of a scale height, is perplexing. The amplitude is small. Near these levels on Venus one expects vertical shear of a few meters per second per scale height to be common, and such a shear would overwhelm the velocity indicated by Eq. 21. Secondly, there is no apparent reason for the selection of a particular L.

Suppose that cloud inhomogeneities of different length scales are imposed. For what scale will the dynamical response be most vigorous? In the stratified regime the horizontal velocity is proportional to the horizontal scale, so large scales are favored. The overturning rate, V / L, is independent of scale and will impose no particular selection. But when L becomes large enough, the transition to a convective regime will occur. From Eq. 18, in this regime the velocity still increases with increasing scale, but only as the square root. The overturning rate, V / L, actually decreases with further increase in scale. Therefore it seems most likely that horizontal scales which place the dynamics on the border between stratified and convective will be favored. From Eqs. 15 and 17 this border is given by

$$\frac{V_0 t_R}{L} \left(\frac{\Delta T_{EV}}{\Delta T_{EH}}\right)^2 = 1. \tag{22}$$

Inserting Eq. 20 and solving for the value of D that satisfies this criterion gives

$$\frac{D}{D_0} = 0.18. \tag{23}$$

Since D represents about half the depth of the dynamical layer, this implies a layer thickness of about 2 km. Numerical estimates of the velocity, overturning time scale, and temperatures are

$$\begin{aligned} V &= 11 \text{ m s}^{-1}, \quad L/V = 0.3 \text{ d}, \\ \Delta T_H &= 0.8 \Delta T_{EH}, \\ \Delta T_V &= \Delta T_{EV}. \end{aligned} \tag{24}$$

It is interesting to note that the horizontal scale emerging from the requirement that the flow regime be on the borderline between stratified and convective is related to a deformation radius. Using the criterion of Eq. 22 and the solutions of Eq. 16 gives

$$L^2 = D^2 N^2 \frac{L^3}{V^3 t_R}, \tag{25}$$

where $N^2 = g\Delta T_V / T_0 D$. The scale given by Eq. 25 is a deformation radius based on a frequency that is a combination of the radiative time constant and the advective time scale, which in this particular case are of the same order.

(iv) Linear analysis

In the foregoing section a fully developed nonlinear flow is examined and a particular horizontal scale is identified. But will this scale also be favored during the early small amplitude phase of flow development? In this section the small amplitude response of the same system will be examined. As previously, a radiative forcing is imposed and the dynamical response is evaluated. In the present case, the response is examined as a function of an imposed frequency and spatial wavenumber.

The Boussinesq approximation is adopted and the static stability is specified. The linearized equations of motion are

$$v_t + \frac{1}{\rho_0} p'_y = 0, \tag{26}$$

$$\frac{1}{\rho_0} p'_z = g\frac{T'}{T_0}, \tag{27}$$

$$v_y + w_z = 0, \tag{28}$$

$$T'_t + w\overline{T}_z = \frac{T'_E - T'}{t_R}. \tag{29}$$

Assume that $\overline{T}_z$ and t_R are constant. Equations 26-29 can be combined into one equation for the temperature, forced by $T'_E(t,y,z)$.

$$\left(\partial_t + \frac{1}{t_R}\right)T'_{zz} + N^2 T'_{yy} = \frac{1}{t_R} T'_{Ezz}, \tag{30}$$

where $N^2 = g\overline{T}_z / T_0$. Assume that the forcing is confined to a depth πD and introduce new dimensionless variables

$$\varsigma = z/D, \quad \eta = y/L, \quad \tau = t/t_R. \tag{31}$$

Eq. 31 becomes

$$(\partial_\tau + 1)T'_{\varsigma\varsigma} + BT'_{\eta\eta} = T'_{E\varsigma\varsigma}, \tag{32}$$

where $B = N^2 D^2 t_R^2 / L^2$ is a Burger number based on a time scale given by the radiative time constant.

The linear response of the system may be importantly influenced by penetration of energy into over and underlying regions. Therefore instead of rigid walls at top and bottom it is useful to use an infinite domain. The forcing is given by

$$\begin{aligned} T'_E &= \Delta T_{EH} \cos(\zeta)\cos(\eta)\cos(\omega t), \quad && |\zeta| \le \pi/2, \\ &= 0, && |\zeta| > \pi/2. \end{aligned} \tag{33}$$

The boundary conditions are boundedness of perturbations for large ζ, and continuity of normal velocity and pressure at the interfaces at $\zeta = \pm\pi/2$.

Solutions are easily found. The system has only two parameters, the Burger number and the frequency. Frequencies of interest are probably on the order of the radiative time

constant. Of particular interest is the variation in response of the system when the Burger number varies, because the horizontal scale enters through the Burger number. Figure 11 displays the vertical velocity and the temperature at the midpoint of the forced layer as functions of B The dimensionless frequency is taken to be unity. For small horizontal scales the temperature response becomes small and the vertical velocity amplitude approaches $W = \Delta T_{EH} / \overline{T}_z t_R$, so that vertical advection in Eq. 29 is the sole balance against the imposed radiative heating. For large horizontal scales the vertical velocity is small and the temperature amplitude approaches a constant, controlled only by the frequency and the radiative time constant.

The dynamical response as measured by the vertical velocity amplitude is strongest when the Burger number is a greater than unity. Thus a strong response occurs when

$$L > NDt_R = ND_0 t_{R0} \left(\frac{D}{D_0} \right)^2 . \tag{34}$$

Using the numerical estimates of Eq. 19 and an estimate of 0.01 s^{-2} for the Brunt frequency gives

$$\frac{D}{D_0} < 0.2. \tag{35}$$

as the criterion for disturbances of horizontal scale 300 km to show a vigorous response. This is consistent with the results of the nonlinear scaling analysis.

(v) Comments

The surprising feature of these dynamical investigations is that they point to a depth shallower than a scale height for the circulations associated with the Venus mesoscale cloud features. Such shallow circulations are consistent with knowledge of the ultraviolet absorber except in one respect. Esposito and Travis (1982) found it essential to allow variations in the overlying submicron haze to be correlated with variations in the main cloud. This haze is located at least a scale height above the top of the main cloud. But their studies are based on the behavior of large scale dark regions, and mesoscale variations may well be different. In fact, it is dynamically reasonable that larger systems, such as the 4-day wave, would penetrate further upward than small systems (Smith et al., 1993).

Acknowledgments

This work has been supported by the NASA Galileo Project, the Pioneer Venus Program, and the Planetary Atmospheres Program. M. D. S. is supported in part by the NASA Graduate Student Researchers Program.

REFERENCES

Avduevskiy, V. S., M. Ya. Marov, Yu. N. Kulikov, V. P. Shari, A. Ya. Gorbachevskiy, G. R. Uspenskiy, and Z. P. Cheremukhina, 1983. Structure and parameters of the Venus atmosphere according to Venera probe data. In *Venus*, Ed. Hunten, D. M., L. Colin, T. M. Donahue, and V. I. Moroz, University of Arizona Press, pages 280-298.

Baker, R. D. II and G. Schubert, 1992. Cellular convection in the atmosphere of Venus. *Nature*, **355**, 710-712.

Belton, M. J. S., G. R. Smith, D. A. Elliot, K. Klaasen, and G. E. Danielson, 1976. Space-time relationships in the UV markings on Venus. *J. Atmos. Sci.*, **33**,1383-1393.

Belton, M. J. S., G. R. Smith, G. Schubert, and A. D. Del Genio, 1976. Cloud patterns, waves and convection in the Venus atmosphere. *J. Atmos. Sci.*, **33**, 1394-1417.

Belton, M. J. S., P. J. Gierasch, M. D. Smith, P. Helfenstein, P. J. Schinder, J. B. Pollack, K. A. Rages, A. P. Ingersoll, K. P. Klaasen, J. Veverka, C. D. Anger, M. H. Carr, C. R. Chapman, M. E. Davies, F. P. Fanale, R. Greeley, R. Greenberg, J. W. Head III, D. Morrison, G. Neukum, and C. B. Pilcher, 1991. Images from Galileo of the Venus cloud deck. *Science*, **253**, 1531-1536.

Crisp, D., 1986. Radiative forcing of the Venus mesosphere. I. Solar fluxes and heating rates. *Icarus*, **67**, 484-514.

Crisp, D., 1989. Radiative forcing of the Venus mesosphere. II. Thermal fluxes, cooling rates, and radiative equilibrium temperatures. *Icarus*, **77**, 391-413.

Del Genio, A. D. and W. B. Rossow, 1990. Planetary-scale waves and the cyclic nature of cloud top dynamics on Venus. *J. Atmos. Sci*, **47**, 293-318.

Esposito, L. W., 1980. Ultraviolet contrasts and the absorbers near the Venus cloud tops. *J. Geophys. Res.*, **85**, 8151-8157.

Esposito, L. W. and L. D. Travis, 1982. Polarization studies of the Venus uv contrasts: Cloud height and haze variability. *Icarus*, **51**, 374-390.

Goody, R. M. and Y. L. Yung, 1989. *Atmospheric Radiation.* Oxford University Press, New York, 519 pp.

Limaye, S. S., 1987. Atmospheric dynamics on Venus and Mars. *Advances in Space Research*, **7**, (12)39-(12)53.

Kawabata, K. D., D. L. Coffeen, J. E. Hansen, W. A. Lane, M. Sato and L. D. Travis, 1980. Cloud and haze properties from Pioneer Venus polarimetry. *J. Geophys. Res*, **85**, 8129-8140.

Newman, M., and C. B. Leovy, 1992. Maintenance of strong rotational winds in Venus' middle atmosphere by thermal tides. *Science*, **257**, 647-650.

Pollack, J. B., O. B. Toon, R. C. Whitten, R. Boese, B. Ragent, M. Tomasko, L. Esposito, L. Travis and D. Weidman, 1980. Distribution and source of the UV absorption in Venus' atmosphere. *J. Geophys. Res.*, **85**, 8141-8150.

Rossow, W. B, A. D. Del Genio, S. S. Limaye and L. D. Travis, 1980. Cloud morphology and motions from Pioneer Venus images. *J. Geophys. Res.*, **85**, 8107-8128.

Schinder, P. J., P. J. Gierasch, S. S. Leroy and M. D. Smith, 1990. Waves, advection and cloud patterns on Venus. *J. Atmos. Sci.*, **47**, 2037-2052.

Seiff, A., 1987. Structure of the atmospheres of Mars and Venus below 100 kilometers. *Adv. Space Res.*, **7**, (12)5-(12)16.

Seiff, A., D. B. Kirk, R. E. Young, R. C. Blanchard, J. T. Findlay, G. M. Kelly and S. C. Sommer, 1980. Measurements of thermal structure and thermal contrasts in the atmosphere of Venus and related dynamical observations: Results from the four Pioneer Venus probes. *J. Geophys. Res.*, **85**, 7903-7933.

Smith, M. D., P. J. Gierasch and P. J. Schinder, 1993. Submitted to *J. Atmos. Sci.* (in press)

Tomasko, M. G., L. R. Dose and P. H. Smith, 1985. The absorption of solar energy and the heating rate in the atmosphere of Venus. *Adv. Space Res.*, **5**, 71-79.

FIGURE CAPTIONS

Figure 1. Mosaic of frames 18228900 and 18228945. North is at the top, east to the right. The general circulation is from east to west with a poleward drift. The bottom of the picture lies just south of the equator, and 100 degrees of longitude are shown. The white crosses show the location of local brightness minimum cloud features identified by the automatic feature tracker, and black crosses show the location of local brightness maximum cloud features.

Figure 2. Brightness scans through a local brightness maximum cloud feature (located just to the left of zero pixels). Ten data numbers (DN) corresponds to an albedo difference of approximately 2%. Time increases from top to bottom covering a total of eight hours. Eight pixels equal one degree or 107 km.

Figure 3. Autocorrelation of a region centered on a typical cloud feature identified by the automatic feature tracker. The distance from one correlation peak to another provides an estimate for the distance between features of similar albedo (local brightness maximum or local brightness minimum). A distance of about 40 pixels (500 km) is indicated.

Figure 4. Averaged profile of all local brightness maximum and local brightness minimum cloud features identified by the automatic feature tracker. Local brightness maximum and local brightness minimum features have similar albedo amplitudes and similar profiles. There is also a tendency for contrasting material to surround identified cloud features.

Figure 5. Contour plots of a fit to the wind velocity obtained from the automatic feature tracker to the five lowest spherical harmonics. The zonal wind fit (Fig. 5a) is nearly flat giving weak jets at mid-latitudes. There also appears to be some divergence from a spot just north of the equator and in the afternoon. The meridional wind fit (Fig. 5b) shows poleward flow.

Figure 6. Paths of local brightness maximum (Fig. 6a) and local brightness minimum (Fig. 6b) cloud features found in three or more consecutive image pairs. The points indicate the position of the feature in the earlier of the images in the image pair. All cloud features move poleward and to the west.

Figure 7a. As in Fig. 6 except that the spherical harmonic fit shown in Fig. 5 has been removed to accentuate non-global motions. Only local brightness maximum cloud features are shown. Local brightness minimum cloud features display similar behavior.

Figure 7b. A small area near the equator (indicated by a box in Fig. 7a) is enlarged to show detail. No organized motions are observed.

Figure 8. Correlation coefficient as a function of time separation between images in an image pair. Each line represents the correlation coefficient for a region surrounding a particular cloud feature identified by the automatic feature tracker. The initial drop in the correlation coefficient is caused by digitization error, while the gradual decrease is caused by deformation. The rate of decrease in the correlation coefficient is the same for local brightness maxima and local brightness minima cloud features.

Figure 9. Solar heating rates in the Venus atmosphere for different profiles of ultraviolet absorber. This figure is from Crisp (1986). The long dashed profile is for a bright uv region and the short dashed profile for a dark one. The solid profile is Crisp's estimate of a global mean. The dotted profile is for an extreme case with the uv absorption placed low.

Figure 10. Regime Diagram.

Figure 11. Linear results. Top: Profiles of vertical velocity amplitude as functions of height. Bottom: Response amplitudes as functions of the Burger number.

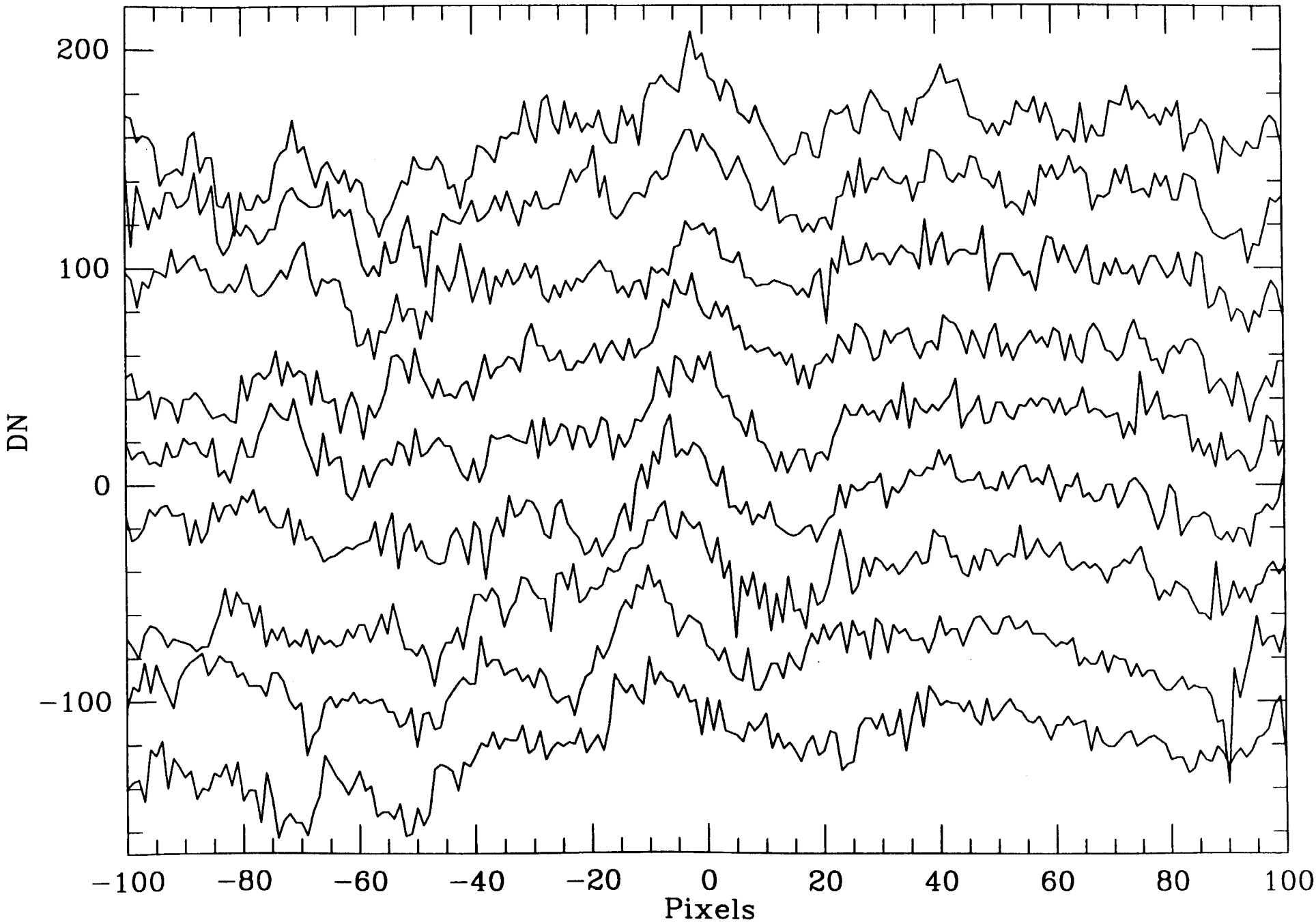

Fig. 2

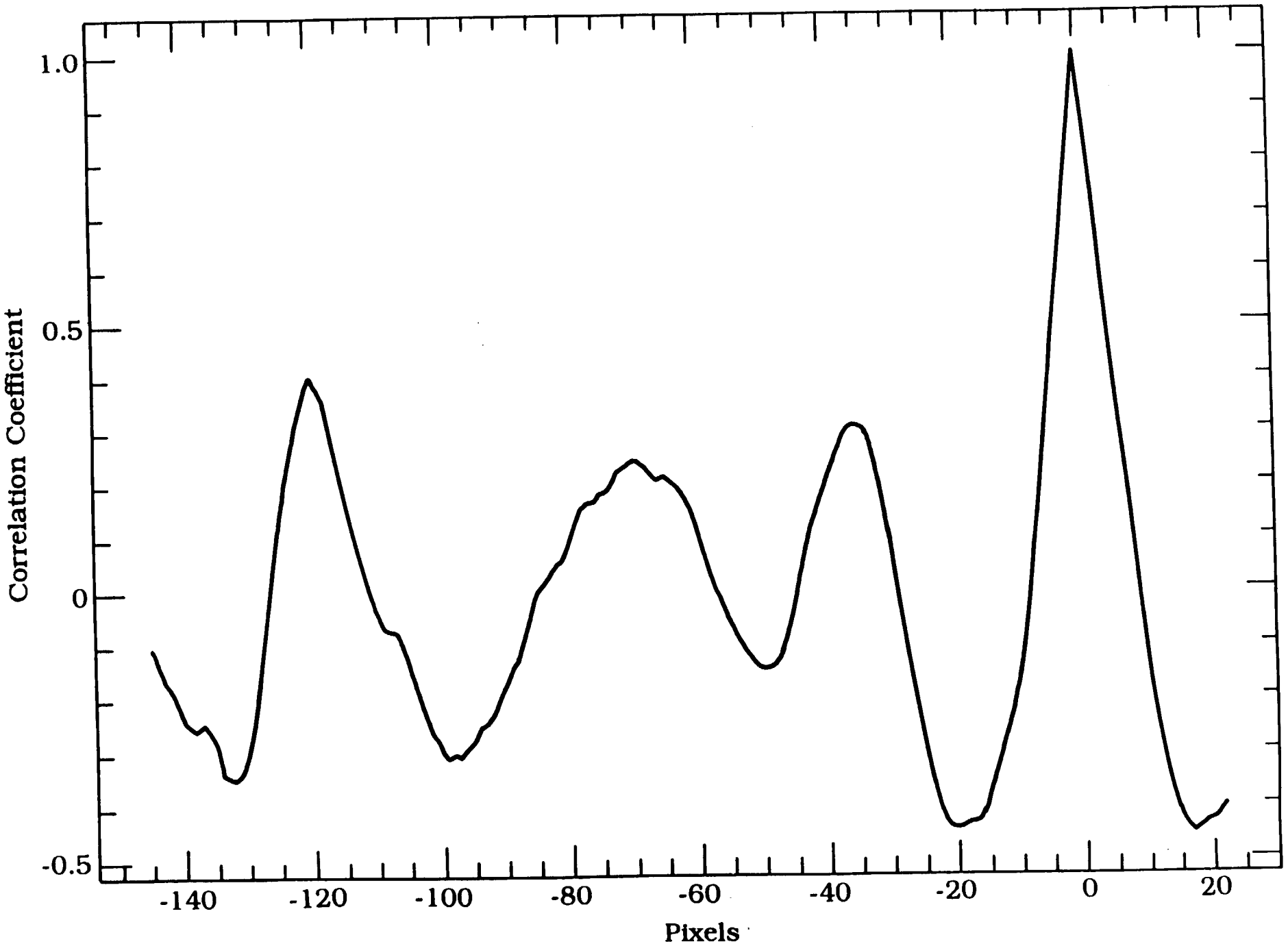
1.0
0.5
0
-0.5
Correlation Coefficient
-140
-120
-100
-80
-60
-40
-20
0
20
Pixels

Fig. 3

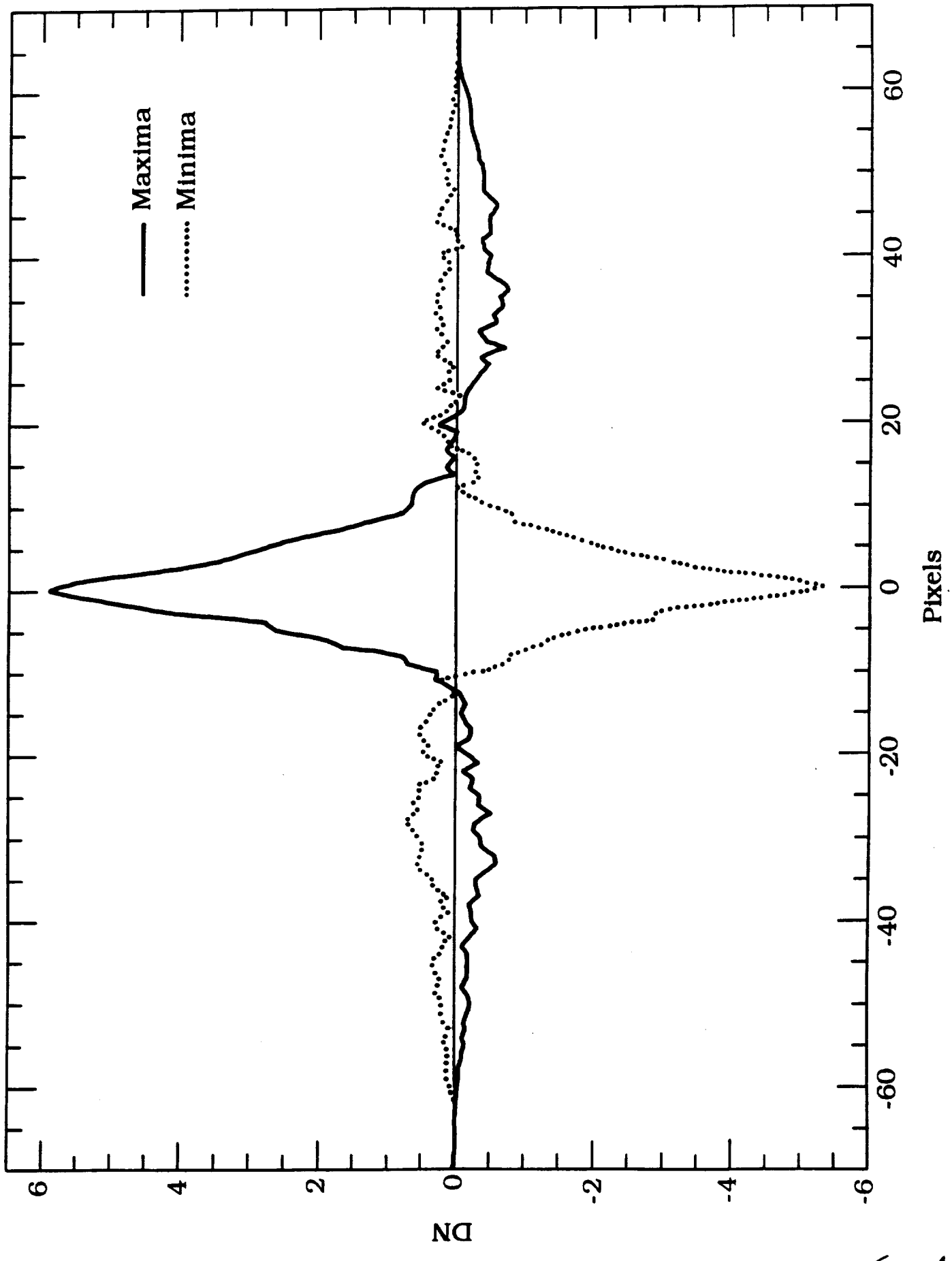

Fig. 4

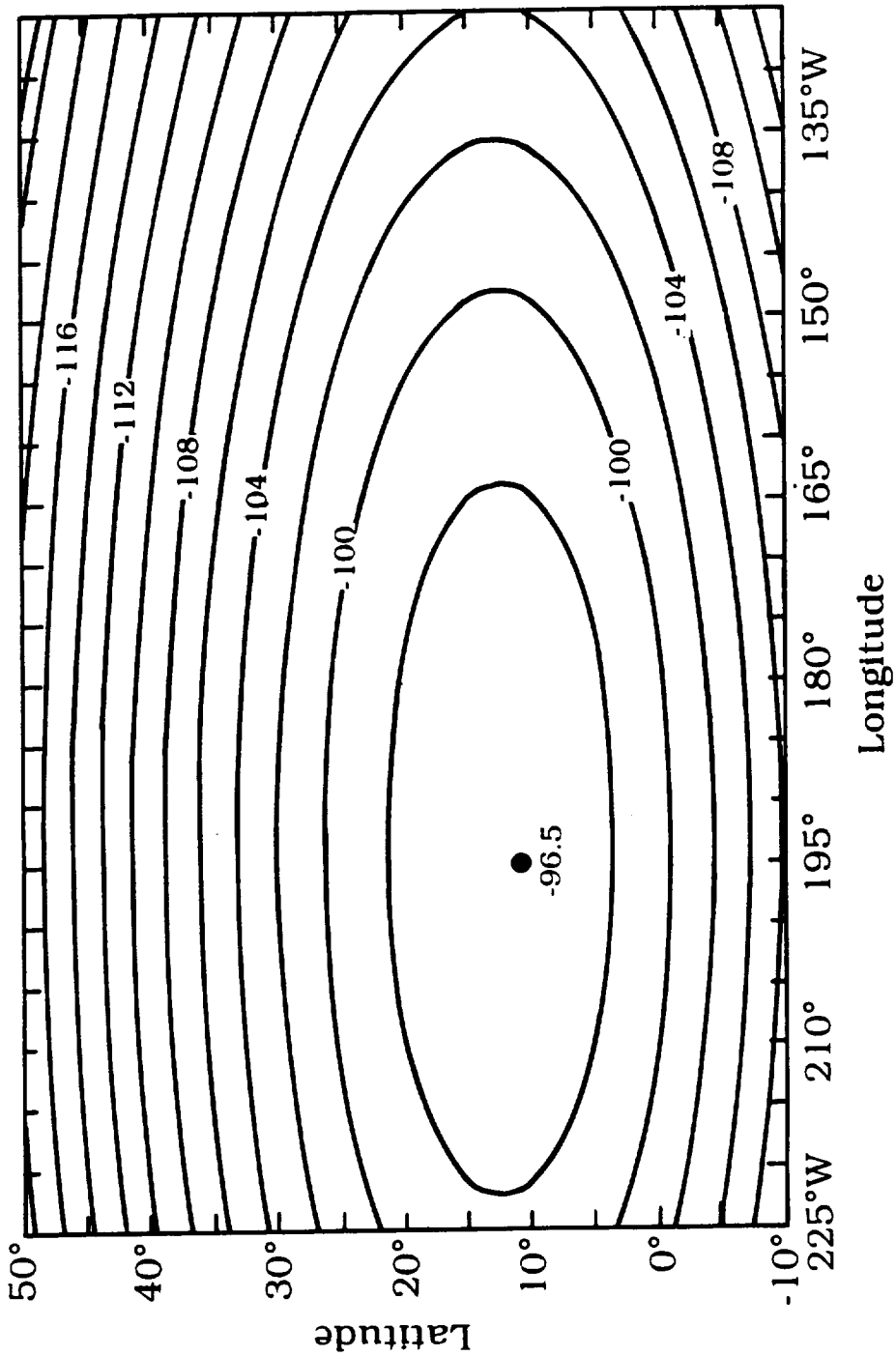
-116
-112
-108
-104
-100
-100
-104
-108
-96.5
50°
40°
30°
20°
10°
0°
-10°
225°W
210°
195°
180°
165°
150°
135°W
Latitude
Longitude

Fig. 5a

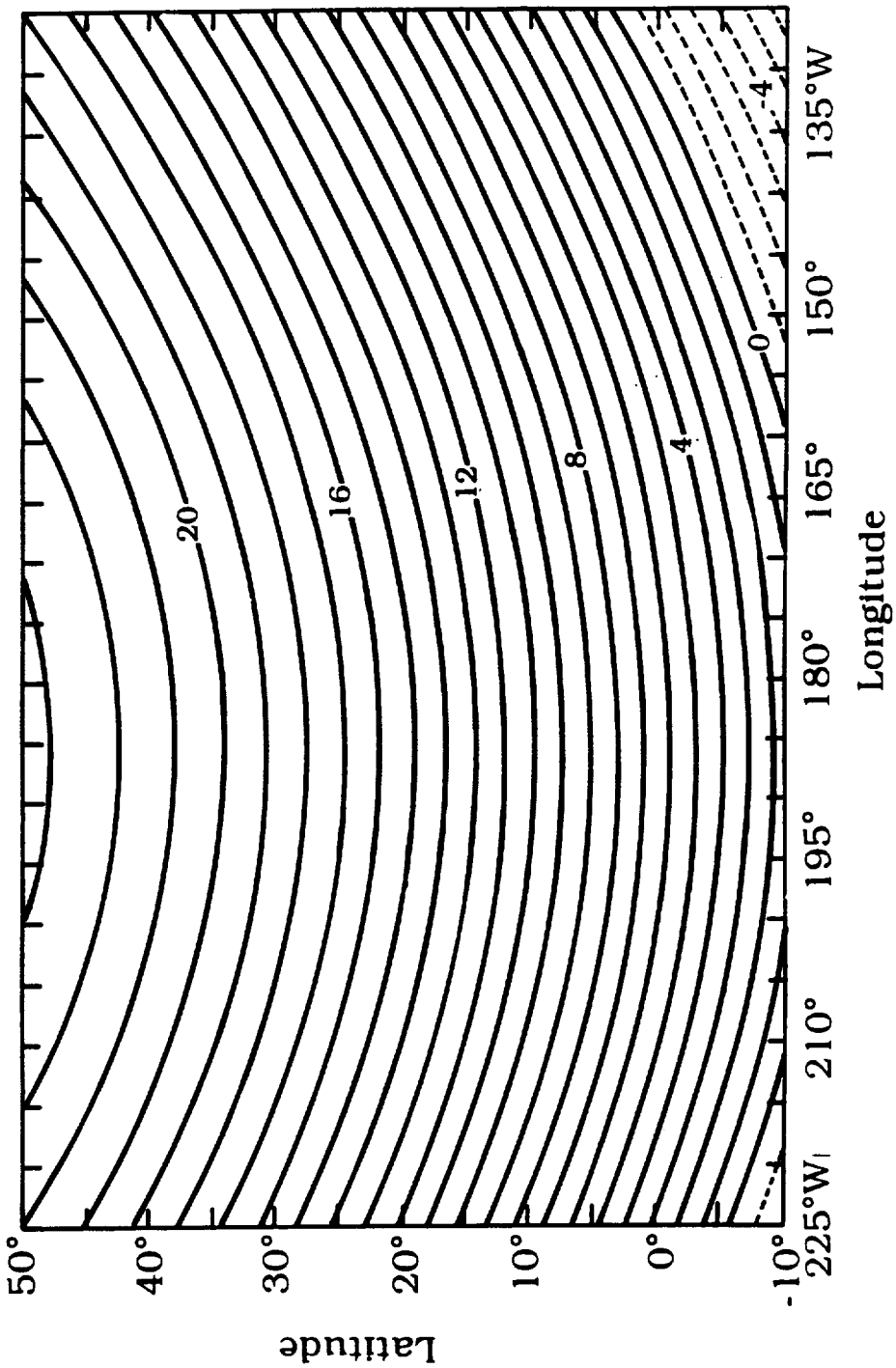
Latitude
50°
40°
30°
20°
10°
0°
-10°
225°W
210°
195°
180°
165°
150°
135°W
Longitude
20
16
12
8
4
0
-4

Fig. 5b

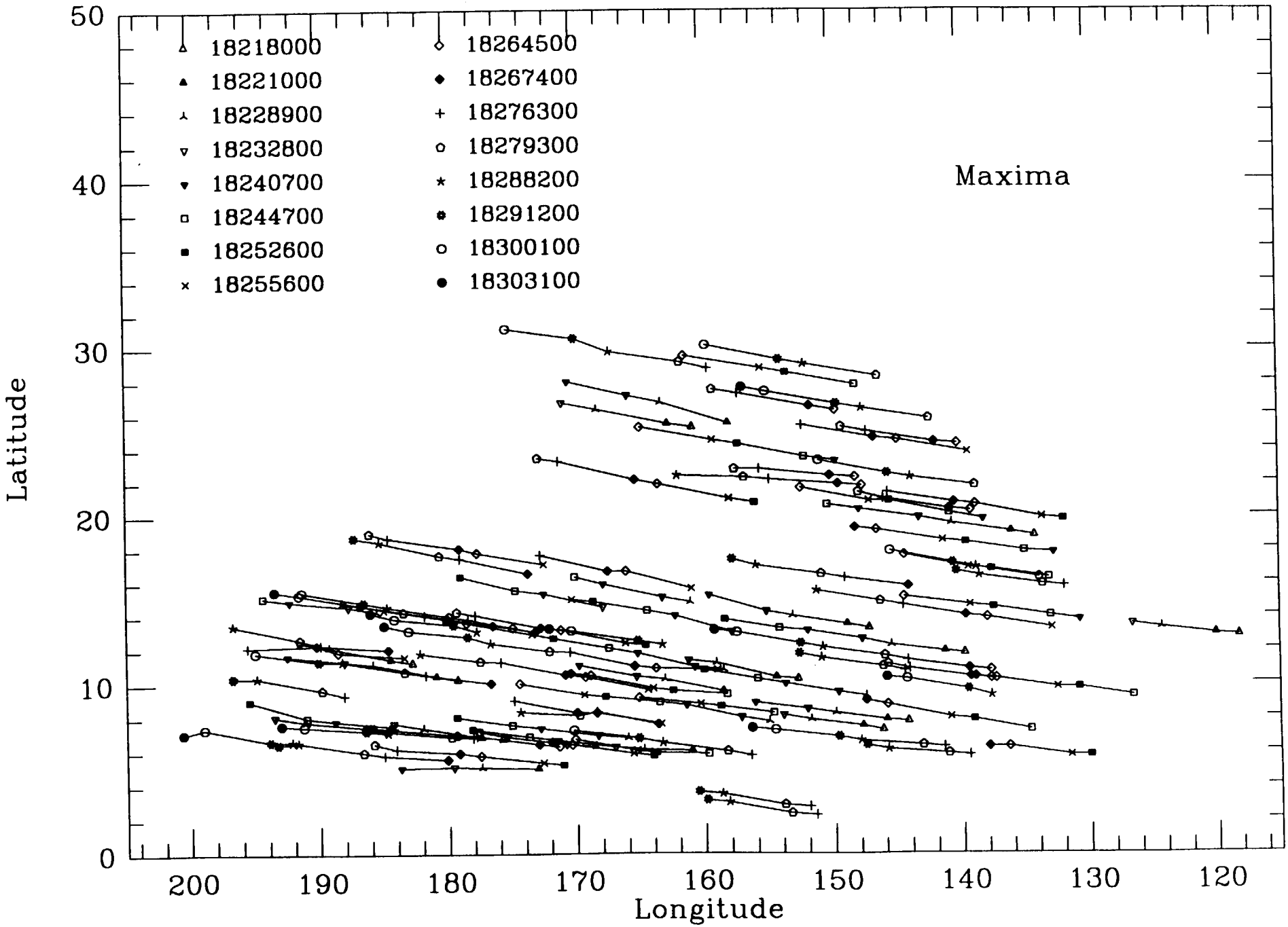
18218000
18221000
18228900
18232800
18240700
18244700
18252600
18255600
18264500
18267400
18276300
18279300
18288200
18291200
18300100
18303100
Maxima
Latitude
Longitude
50
40
30
20
10
0
200
190
180
170
160
150
140
130
120

Fig. 62

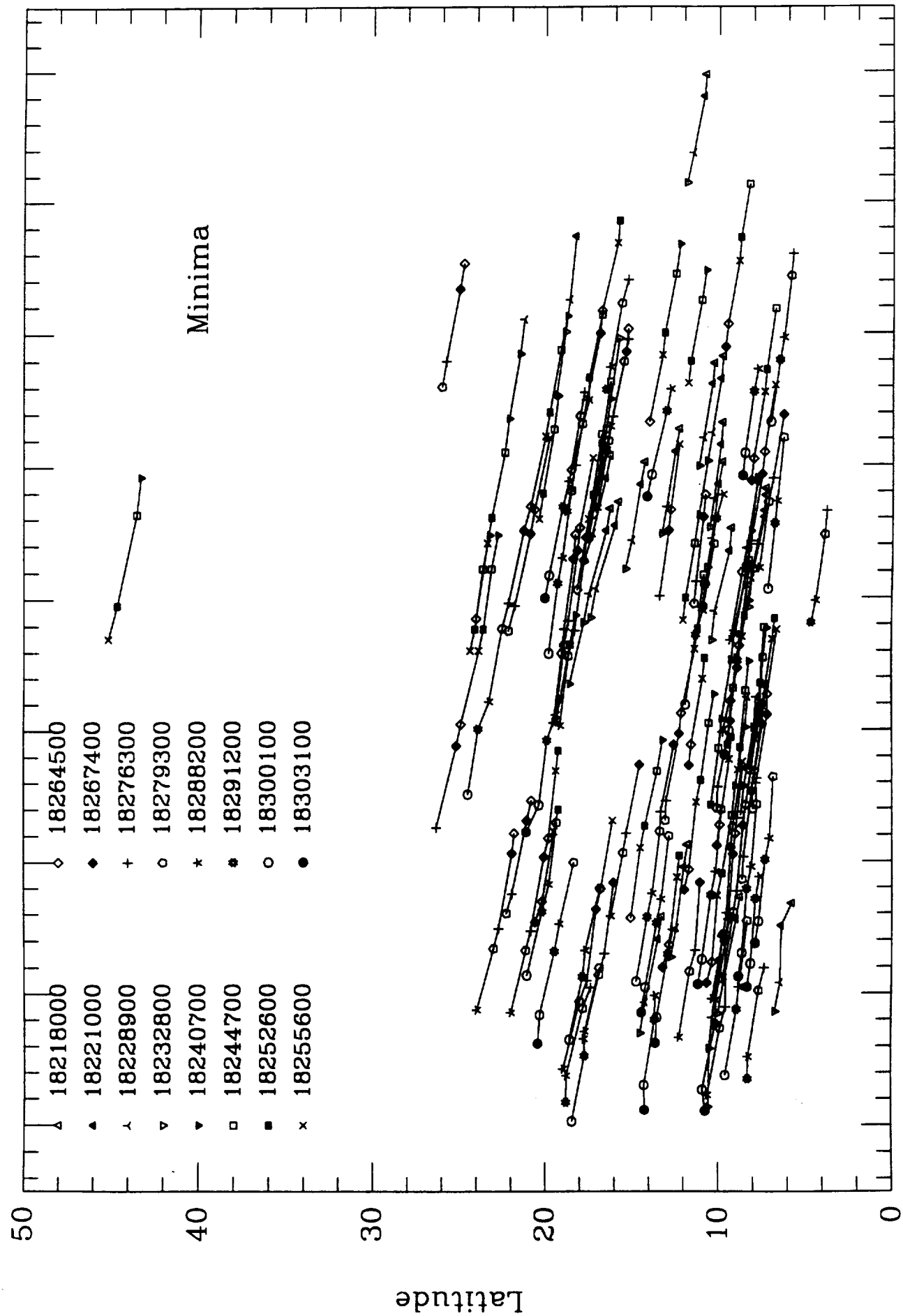
Minima
18218000
18221000
18228900
18232800
18240700
18244700
18252600
18255600
18264500
18267400
18276300
18279300
18288200
18291200
18300100
18303100
Latitude
Longitude
50
40
30
20
10
0
200
190
180
170
160
150
140
130
120

Fig. 6b

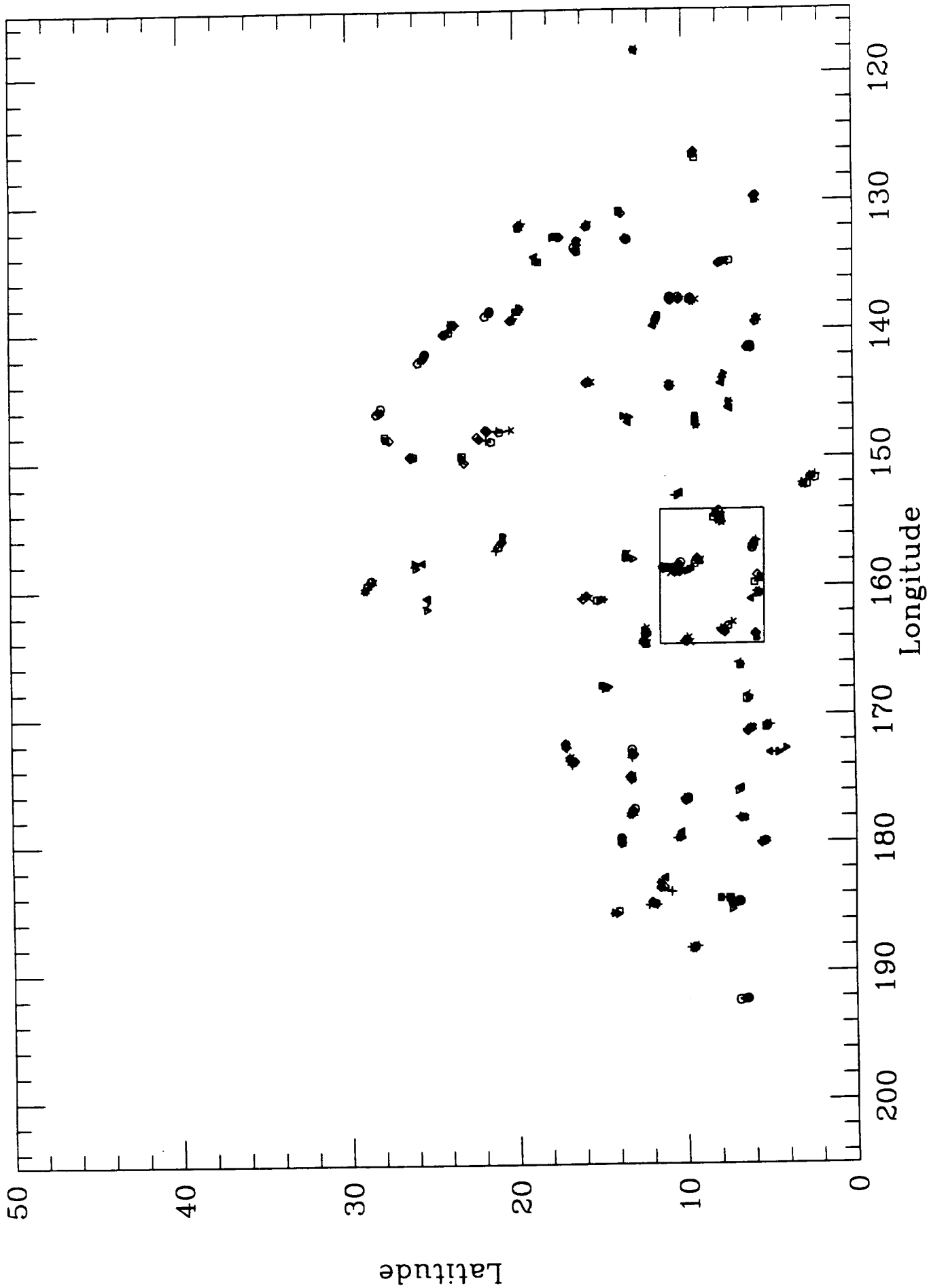
Latitude
50
40
30
20
10
0
200
190
180
170
160
150
140
130
120
Longitude

Fig. 7a

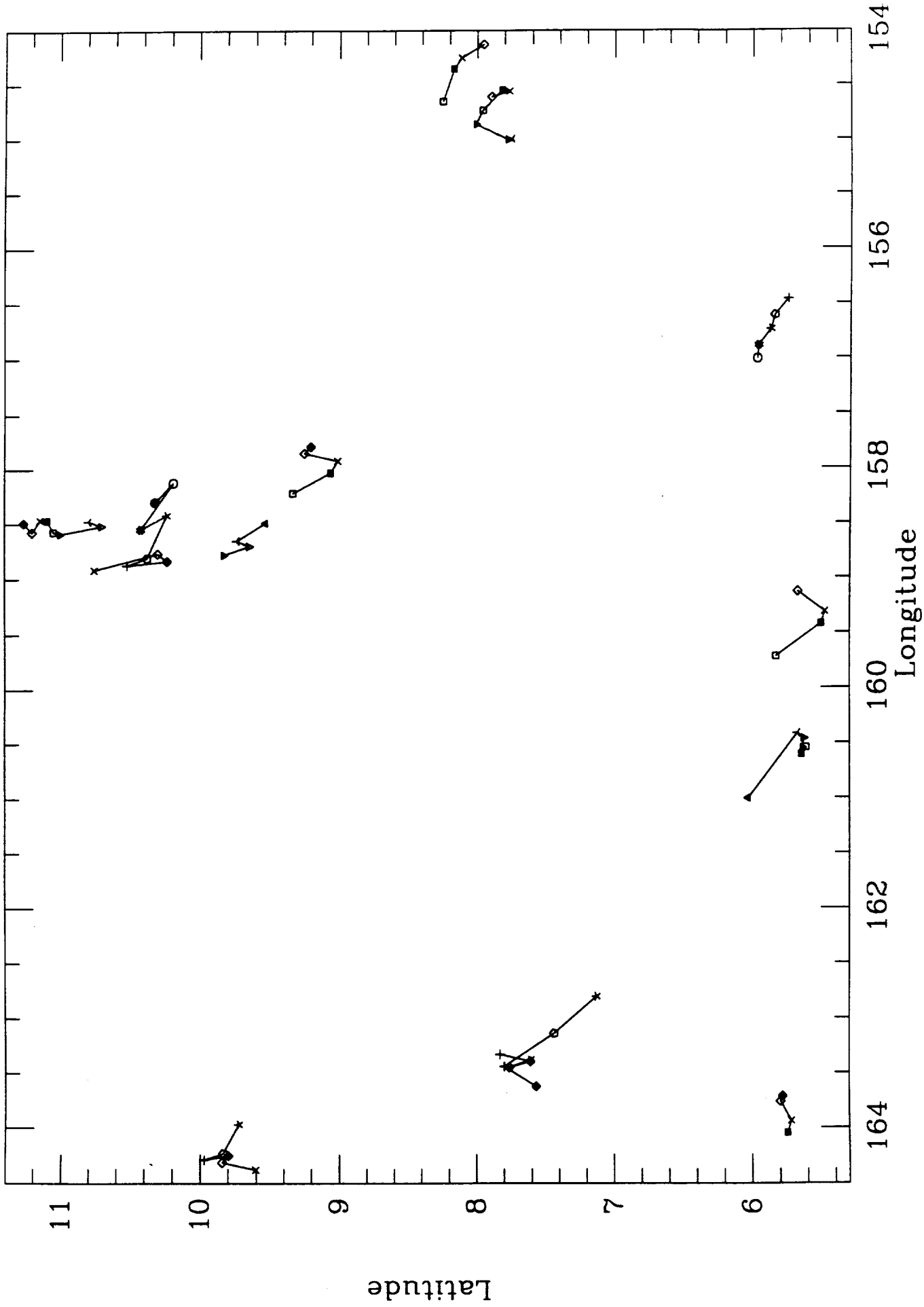

Fig. 7b

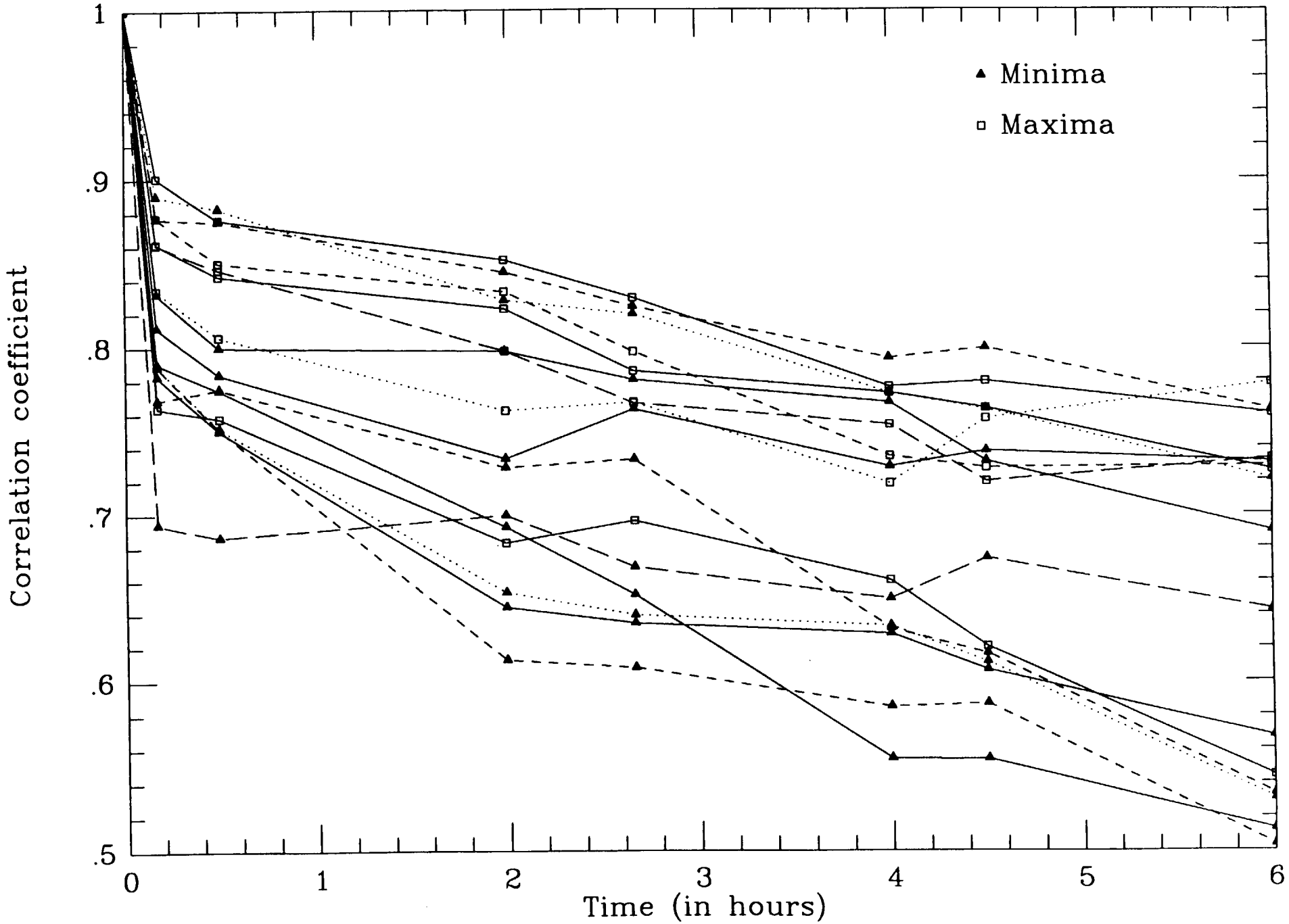
Minima
Maxima
Correlation coefficient
Time (in hours)
1
.9
.8
.7
.6
.5
0
1
2
3
4
5
6

Fig. 8

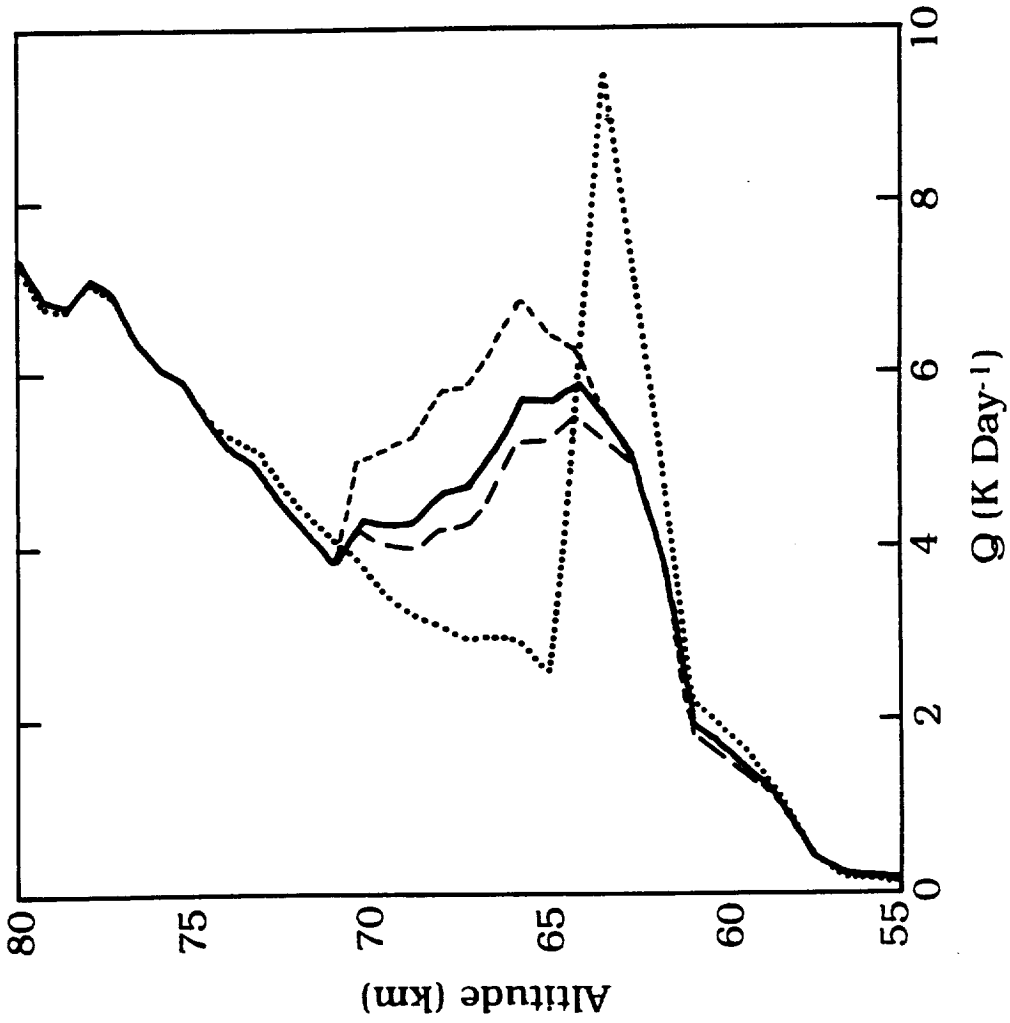

Fig. 9

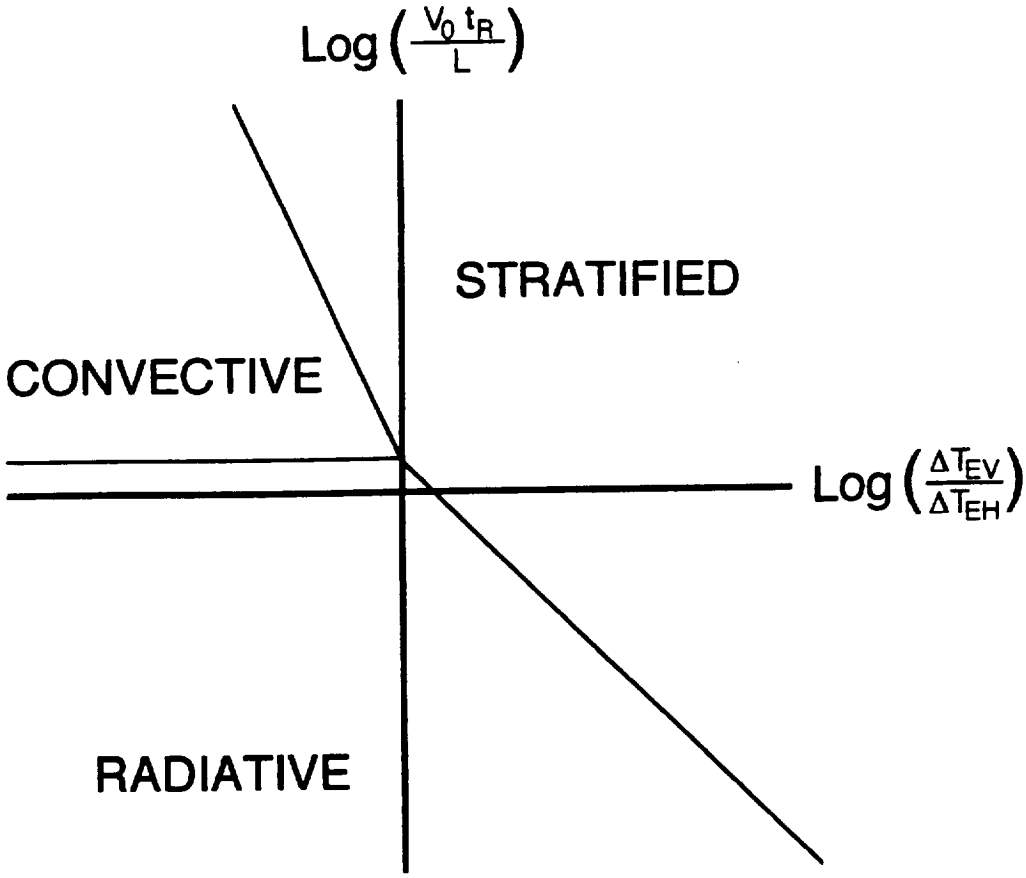
Log $\left(\frac{V_0 t_R}{L}\right)$
STRATIFIED
CONVECTIVE
Log $\left(\frac{\Delta T_{EV}}{\Delta T_{EH}}\right)$
RADIATIVE

Fig. 10

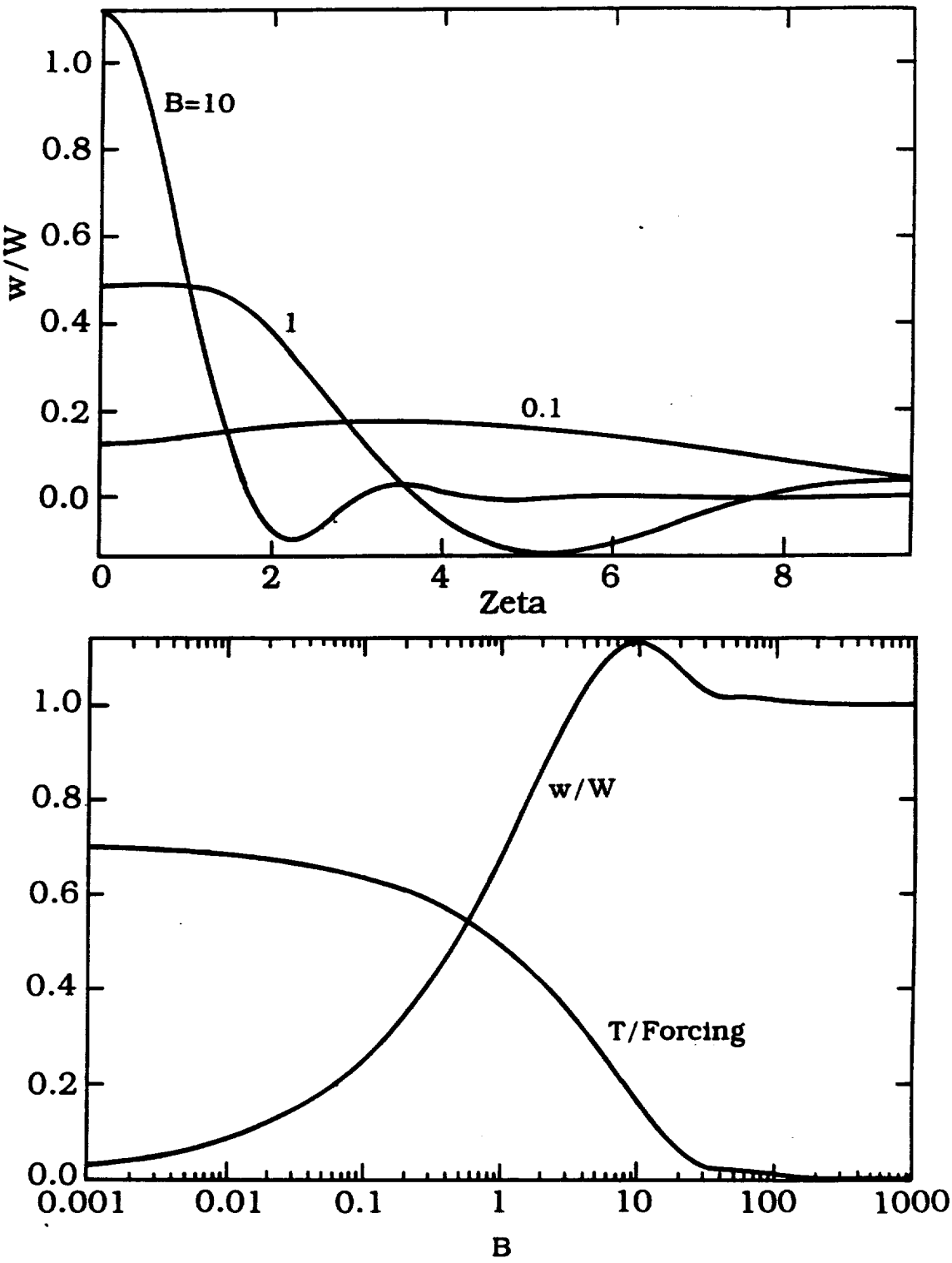
1.0
0.8
0.6
0.4
0.2
0.0
w/W
B=10
1
0.1
0
2
4
6
8
Zeta
1.0
0.8
0.6
0.4
0.2
0.0
w/W
T/Forcing
0.001
0.01
0.1
1
10
100
1000
B

Fig. 11